Biogenic Impact of Urban Vegetation on Heat and Carbon Dynamics

in the Built Environment

by

Peiyuan Li

A Dissertation Presented in Partial Fulfillment
of the Requirements for the Degree
Doctor of Philosophy

Approved October 2021 by the
Graduate Supervisory Committee:

Zhi-Hua Wang, Chair
Huei-Ping Huang
Soe W. Myint
Enrique R. Vivoni
Tianfang Xu

ARIZONA STATE UNIVERSITY

December 2021

ABSTRACT

The fast pace of global urbanization makes cities the hotspots of population density and anthropogenic activities, leading to intensive emissions of heat and carbon dioxide (CO_2), a primary greenhouse gas. Urban climate scientists have been actively seeking effective mitigation strategies over the past decades, aiming to improve the environmental quality for urban dwellers. Prior studies have identified the role of urban green spaces in the relief of urban heat stress. Yet little effort was devoted to quantifying their contribution to local and regional CO_2 budget. In fact, urban biogenic CO_2 fluxes from photosynthesis and respiration are influenced by the microclimate in the built environment and are sensitive to anthropogenic disturbance. The high complexity of the urban ecosystem leads to an outstanding challenge for numerical urban models to disentangling and quantifying the interplay between heat and carbon dynamics.

This dissertation aims to advance the simulation of thermal and carbon dynamics in urban land surface models, and to investigate the role of urban greening practices and urban system design in mitigating heat and CO_2 emissions. The biogenic CO_2 exchange in cities is parameterized by incorporating plant physiological functions into an advanced single-layer urban canopy model in the built environment. The simulation result replicates the microclimate and CO_2 flux patterns measured from an eddy covariance system over a residential neighborhood in Phoenix, Arizona with satisfactory accuracy. Moreover, the model decomposes the total CO_2 flux from observation and identifies the significant CO_2 efflux from soil respiration. The model is then applied to quantify the impact of urban greening practices on heat and biogenic CO_2 exchange over designed scenarios. The result shows the use of urban greenery is effective in mitigating both

urban heat and carbon emissions, providing environmental co-benefit in cities. Furthermore, to seek the optimal urban system design in terms of thermal comfort and CO_2 reduction, a multi-objective optimization algorithm is applied to the machine learning surrogates of the physical urban land surface model. The dissertation finds there are manifest trade-offs among ameliorating diverse urban environmental indicators despite the co-benefit from urban greening. The findings of this dissertation, along with its implications on urban planning and landscaping management, would promote sustainable urban development strategies for achieving optimal environmental quality for policy makers, urban residents, and practitioners.

ACKNOWLEDGMENTS

First of all, I would like to express my deepest and sincerest appreciation to my advisor and dissertation committee chair, Professor Zhihua Wang, for his outstanding mentoring throughout my four and half years of doctoral study. Without him, this dissertation would not be possible. During my Ph.D. study, I am always supported by his patience, warm encouragement, and extraordinary guidance, and inspired by his passion in research and teaching, as well as his foresight in science. Professor Wang has given me sufficient freedom to live on my own schedule and pursue different projects. His training and mentoring style fostered my independency as a researcher; his advising and guidance will be beneficial to my future career. It is a great pleasure and honor to be his student and work with him.

I am also extremely grateful to my committee members, Professor Enrique R. Vivoni, Professor Huei-Ping Huang, Professor Soe W. Myint, and Professor Tianfang Xu for their time and patience in supervising my research work, their invaluable and insightful feedback and suggestions on this dissertation, and their indispensable contributions to my development as a young scientist.

I would like to thank Professor Larry W. Mays, Professor Peter Fox, Professor Giuseppe Mascaro, and Professor Otakuye Conroy-Ben at the Sustainable Engineering and the Built Environment, Professor Robert McCulloch from School of Mathematical and Statistical Sciences, Professor David J. Sailor at the School of Geographical Sciences & Urban Planning, for their kind help, advice, and encouragement during my time at Arizona State University. I also acknowledge the administrative members in the School of Sustainable Engineering and the Built Environment at ASU, especially Michael Sever, Melanie Duran from the advising team, Wafa Cox from human resources team, and Kayla Vestal and Jhanaye Glynn from financial team for their management of my Teaching and Research Assistantships during my Ph.D. study.

I would like to thank my former advisors, Professor Brian R. Ellis at University of Michigan, and Professor Weiguang Wang, Professor Peng Yi at Hohai University, for their advising and continuous encouragement.

Special thanks to my Ph.D. colleagues and officemates Dr. Chenghao Wang, Xin Guan, Zhaocheng Wang, Adil Mounir, Lorrayne Miralha Marin Da Silva, and Xueli Yang, for their support, encouragement, and general help throughout my Ph.D. study.

I also gratefully acknowledge the financial support from many organizations and departments, including the U.S. National Science Foundation, National Aeronautics and Space Administration, National Oceanic and Atmospheric Administration, and the School of Engineering and the Graduate College at Arizona State University.

Finally, I would like to express my special and most sincere thanks to my family back in China and my fiancée, Wenjuan Liu, for their strong support of my academic endeavors.

TABLE OF CONTENTS

LIST OF TABLES

LIST OF FIGURES

Figure		Page

CHAPTER 1

INTRODUCTION

1.1 Literature Review

1.1.1 Background

Urban areas cover about 3% of the global land surface but accommodate more than half of the global population today; the latter figure will escalate to 67% by the mid-century (UN 2019). The growth in urban population significantly intensifies anthropogenic stressors and greenhouse gas (GHG) emissions from traffic, heating, power generation, cement production, etc., leading to a continuous rising of thermal discomfort and CO_2 level in cities (L.E. Mitchell et al. 2018). The effect of urbanization on elevated ambient temperature is commonly known as the urban heat island (UHI) effect (T.R. Oke 1973; 1982). Seeking for countermeasures to mitigate the UHI effect has emerged as an active research area in past decades through modeling the energetic exchange in the built environment using urban land surface models (LSMs).

Over past decades, urban LSMs have undergone continuous development from simple urban energetic models (H. Kusaka et al. 2001; V. Masson 2000) to incorporate momentum transport (A. Martilli 2002), urban hydrological processes (N. Meili et al. 2020; X. Stavropulos-Laffaille et al. 2018; Z.-H. Wang et al. 2013), and anthropogenic emissions (D.J. Sailor 2011; D.J. Sailor & L. Lu 2004). In particular, urban LSMs have gradually evolved to incorporate parameterization schemes of urban vegetation with increasing complexity, such as green roofs (A. Lemonsu et al. 2012; J. Yang & Z.-H. Wang 2014), urban trees (S.-H. Lee et al. 2016; S.-H. Lee & S.-U. Park 2008; Y.-H. Ryu et al. 2015; R. Upreti et al. 2017; Z.-H. Wang 2014), and urban irrigation (C. Wang et al.

2019c; J. Yang & Z.-H. Wang 2015). These new schemes significantly enhanced the model predictive skill over realistic built terrains, furnishing further improvement of urban LSMs for capturing biogenic and anthropogenic carbon emission in urban areas (J. Song et al. 2017).

In addition to the pronounced UHI effect, cities are also hotspots of GHG emission, especially CO_2, with concentrated sources and human activities (C.S.B. Grimmond et al. 2002; L.R. Hutyra et al. 2014). In particular, anthropogenic CO_2 ($AnCO_2$), primarily emitted from the fossil fuel combustion, constitutes the largest flux of CO_2 to the atmosphere and represents the dominant source of GHG forcing to emergent climate patterns (K.R. Gurney 2014). $AnCO_2$ emissions are often used as a near-certain boundary conditions for solving total carbon budget, which is essential to improve our fundamental understanding of the feedback mechanisms between the carbon cycle and climate changes (R.C. Balling Jr et al. 2001; M. Vetter et al. 2008). Accurate quantification of the urban CO_2 emission, either biogenic or anthropogenic in source, requires the integration of observational, mechanistic, and modeling methods at fine resolutions (K.R. Gurney 2014; K.R. Gurney et al. 2012).

By combining the advantages of "bottom-up" inventory data by sectors and the "top-down" spatial distributed dataset from remote sensing imagery (D.J. Sailor 2007; D.J. Sailor & L. Lu 2004), the CO_2 mapping technology today can represent the efflux estimation over space and time with wide coverage (global or continental scale), high spatial resolution (1~10km) (C. Gately et al. 2019; K.R. Gurney et al. 2019; A.R. Jacobson et al. 2020; T. Oda et al. 2018), and reliable with cross validations. The finest grid currently available, with resolution of 1 km^2 in space and 1 hour in time, can be used to resolve footprints and disentangle different sources of carbon emission of eddy-covariance (EC) measurements. The gridded datasets are also capable of distinguishing carbon fluxes from different sectors, albeit mostly focused on fossil fuel emission from moving vehicles (C. Gately et al. 2019; A.R. Jacobson et al. 2020). The mapping of biogenic CO_2 release or uptake is usually missing in the built environment, mainly due to the complex flow field and dynamics of transport in the built environment (H.J.S. Fernando 2010). Up to date, the biogenic sources of CO_2 emission is largely under explored as compared to its $AnCO_2$ counterpart, especially in residential areas with substantial fraction of vegetation cover. This inadequacy of capturing CO_2 emission by plant physiological functions in urban areas, in turn, surfaces in the net ecosystem exchange (NEE) gridded data, leading to large uncertainties and degraded data quality (J. Macknick 2011).

The representation of urban vegetation in current urban LSMs is, on the other hand, almost exclusively focused on the cooling effect and hydrological processes. The quantification of urban CO_2, up to date, remains largely based on observational data (C.S.B. Grimmond et al. 2002; L.E. Mitchell et al. 2018; D.E. Pataki et al. 2003; D.E. Pataki et al. 2006). Recently, a pioneering work has been conducted for numerical CO_2 flux modeling at the street scale (M. Goret et al. 2019). The model was tested over a heavily urbanized city center (90% impervious surface), and showed urban vegetation played a minimum role in CO_2 exchange (less than 3%) due to the small vegetation fraction in city core. While the model performance is good, the limited representation of biogenic CO_2 emission constrains its applications to highly impervious areas. In contrast, nearly half of the urban land in the U.S. attributes to residential use, where the vegetation fraction is significantly higher than it in urban cores (F. Pozzi & C. Small 2001), with the presence of urban vegetation in the forms of urban parks, golf courses, and most importantly, maintained urban gardens. It is therefore critical for urban LSMs to capture plant responses to elevated temperature, CO_2 level, irrigation, and active lawn management.

1.1.2 Interplay between Thermal and Carbon Environment in Cites

It is noteworthy that most anthropogenic heat sources, such as vehicular emission and heating, ventilation, and air conditioning (HVAC) systems, are also significant contributors to greenhouse gases, especially carbon dioxide (CO_2). The elevated CO_2 concentration and deteriorated air quality in cities, in turn, tend to intensify the local UHI effect and further contribute to climate change at a global scale (G. Churkina 2016; L.R. Hutyra et al. 2014). In searching for the effective carbon reduction strategies, much effort in previous years has been devoted to quantifying the anthropogenic releases of CO_2 via direct measurement, modeling, and inventory approaches (B. Crawford et al. 2011; C.K. Gately & L.R. Hutyra 2017; C.K. Gately et al. 2015; M. Goret et al. 2019; L. Järvi et al. 2019; M. Sargent et al. 2018). While it is well recognized that the anthropogenic CO_2 ($AnCO_2$) releases from fossil fuel consumption dominate the overall carbon efflux in cities, many studies also pointed out that the biogenic CO_2 from urban greening spaces cannot be neglected (O. Bergeron & I.B. Strachan 2011; L.R. Hutyra et al. 2014; T. Vesala et al. 2008). The carbon sequestration by urban vegetation (lawns, parks, golf courses, and residential gardens) can partially offset, e.g., the vehicular CO_2 emission.

Some densely vegetated areas can achieve carbon neutral during warm months due to active plant CO_2 uptake (O. Bergeron & I.B. Strachan 2011).

Urban vegetation behaves distinctively from plants in the natural environment, primarily due to their peculiar growing conditions in the built environment. It is noteworthy that urban areas usually furnish favorable conditions for plant growth and physiological functions, because in cities: 1) warmer ambient temperatures, e.g. those due to the prominent urban heat island effect, allow urban plants to maintain a higher photosynthesis rate and a longer growing period (E.C. Lahr et al. 2018; L. Meng et al. 2020; S. Zhao et al. 2016); 2) regular maintenance practices, such as irrigation and fertilization, relieve much of environmental stresses for plant growth (A.M. Luketich et al. 2019); and 3) the elevated CO_2 level forms a natural CO_2 pump, promoting the carbon assimilation rate (H. Wang et al. 2017; S. Wang et al. 2019).

Among urban vegetation, urban trees have the most sophisticated biophysical functions, partially due to the complexity of their geometry (three dimensional as compared the planar distribution of grasses). Previous studies have found that the presence of street trees significantly alter the microclimate and the heat and moisture re-distribution in the urban canyon, including the change of surface energy balance (C.S.B. Grimmond et al. 2009), the reduction of thermal discomfort (E. Redon et al. 2020; C. Wang et al. 2018c), and weakening the passive pollutant dispersion (C. Wang et al. 2018a), to name a few. In particular, urban trees influence CO_2 dynamics in counteracting ways: they are effective carbon sinks via photosynthesis, but meanwhile can also create unfavorable growing conditions for shaded ground vegetation (e.g. lawns). The shading effect tends to intercept solar radiation for photosynthesis and lower the ground level temperature (C.S.B. Grimmond et al. 2002; S.-H. Lee & S.-U. Park 2008; A. Lemonsu et al. 2012; R. Upreti et al. 2017), hence reduces the carbon uptake via ground vegetation by impeding their physiological functions.

Meanwhile, being the growing media of vegetation and an indispensable part of urban green spaces, soil surface is a net CO_2 source in most cases (B. Koerner & J. Klopatek 2002; X. Tao et al. 2016). With urban warming and landscaping management, soil respiration rate is expected to be higher in cities than in the natural environment (A.R. Contosta et al. 2020; S.M. Decina et al. 2016; E.A. Dyukarev 2017; T. Vesala et al. 2008). Bare soil patches in degraded lawns due to inappropriate management release more CO_2 than bare soil land because of the continuing root and microbial respiration (J. Bae & Y. Ryu 2017; B.J.L. Ng et al. 2015). Even with vegetation cover, S.M. Decina et al. (2016) found the annual soil respiration in a residential area with active landscaping management is comparable to the local traffic emissions in hot months, causing undesired effects on carbon reduction.

To achieve the optimal environmental co-benefit for mitigating both heat and carbon emissions by urban greening, holistic understanding of the physiological functions of urban vegetation is of pivotal importance. Theoretically, the rate of carbon release (respiration) and uptake (photosynthesis) from urban vegetation will be influenced by environmental temperature and soil water. Cooling provided by urban greening inhibits soil respiration and photosynthetic activities, working towards opposite directions in carbon budget. Similarly, urban irrigation provides water for plant growth and microbial respiration, influencing photosynthesis and respiration simultaneously. Whether urban greening (i.e. the expansion of vegetation fraction and irrigation) promotes or impedes

CO_2 sequestration depends on the expansion rate and cooling efficiency, leading to possible trade-offs or co-benefits between thermal and carbon mitigation. Based on in-situ observation or simple empirical models at neighborhood scale, previous studies pointed out the importance of the complex interactions and feedbacks between urban green spaces and the built environment (A. Christen et al. 2011; B. Crawford et al. 2011; E. Velasco & M. Roth 2010; E. Velasco et al. 2013). Yet, the discussions in prior studies were largely focused the singular impact on either thermal or carbon environment separately. Those focused on carbon exchange usually quantify the contribution of urban vegetation to the total CO_2 flux over the built terrain with fixed vegetation fraction and irrigation scheme, thus have limited abilities to examine the environmental response in terms of the alternation in land use and landscaping management strategies, as well as to guide future planning and decision making.

On the other hand, numerical models have the advantage over observational measurements by avoiding the limited timespans or footprints of measuring instruments, and number of sites, thus providing a versatile alternative approach to study the urban environment. Past decades have seen the development of numerous urban LSMs to simulate the dynamics and transport of heat and CO_2 emissions in the built environment (A.J. Arnfield 2003; T.R. Oke et al. 2017). In particular, numerical simulations at multi-scales, ranging from neighborhood to regional scales, were conducted to evaluate urban greening for cooling and energy saving, subjected to future trend of urbanization and global changes (e.g., J. Song & Z.-H. Wang 2016; Z.-H. Wang & R. Upreti 2019). From CO_2 exchange perspective, modeling technique has usually been applied to decompose the total CO_2 flux measured by eddy covariance system to identify the individual sector of the carbon source, but rarely discussed in the context of environmental co-benefit of heat and CO2 mitigation, or the evaluation of overall environmental quality under specific urban design. For the sustainable development of future cities amid the global climate change, it is of vital necessity to view the compound (multiple) environmental measures rather than on a singular (especially cooling) effect alone (Z.-H. Wang 2021). This emerging research interest calls for the advancement in urban land surface models to disentangle the complex interplay between thermal and carbon environment in cities.

1.1.3 Urban Canopy Modeling

Physics of flow and transport in the urban canopy layer (UCL) involve complex interplay of land surface processes, atmospheric turbulence, and anthropogenic activities. The numerical modeling of urban microclimate hence focus on two broad compartments: (1) the atmospheric transport using parameterization (e.g. Reynolds-averaged Navier-Stokes or RANS equations), computational fluid dynamics (e.g. large-eddy simulations), or stochastic dispersion (Y. Toparlar et al. 2017; C. Wang et al. 2018a), that relies heavily on wind-tunnel tests as the "ground truth", and (2) urban LSMs that resolve the surface transport of energy, water/moisture, momentum, and scalars, especially those arising from built terrains. Among existing urban LSMs, the single-layer urban canopy models (UCMs) are probably the most widely used. They are particularly attractive to researchers for maintaining a fine balance between the numerical simplicity (i.e. urban canyon representation) and the comprehensiveness of land surface dynamics. Despite its comparative simplicity to more sophisticated LSMs, single-layer UCMs have tractable parameter sensitivity (T. Loridan et al. 2010; Z.-H. Wang et al. 2011) and often give satisfactory performance with the same level of model calibration (C.S.B. Grimmond et al. 2011; C.S.B. Grimmond et al. 2010). These UCMs have been incorporated into the popular meso-scale Weather Research and Forecasting (WRF) model (F. Chen et al. 2011; H. Kusaka et al. 2001; J. Yang et al. 2014) and extensively applied for local and regional urban hydrometeorological modeling for cities all over the world.

In this dissertation, we adopt a state-of-the-art single-layer UCM as the numerical stratum for capturing the dynamic transport in urban energy and hydrological cycles (Z.-H. Wang et al. 2013; J. Yang & Z.-H. Wang 2014; J. Yang et al. 2014). This UCM represents the built terrain as a generic unit of two-dimensional (2D) street canyon, consisting of two arrays of buildings separated by a road, with infinite longitudinal dimension. Inside the street canyon, the heterogeneity of the ground facet is represented using sub-facets of paved surfaces (road), bare soil, and vegetated areas (lawns and trees). Furthermore, the morphological representation of urban trees in the UCM is made configurable to accommodate flexible location and number of rows of trees. The model resolves explicitly the radiative heat exchange between shade trees and built facets (Z.-H. Wang 2014) and transpiration by tall vegetation, in addition to the ground level vegetation (lawns). The physical representation of plants in the built environment makes the UCM a versatile platform to incorporating photosynthesis and respiration models.

Figure 1.1 shows a schematic of the single-layer UCM incorporating urban carbon exchange processes, where the dimensional parameters w, r and h are the canyon width, roof width and building height respectively; z_a, z_R and z_T are the reference height of the atmospheric layer, building, and street canyon, respectively; R_b, R_h, R_t, R_s, and R_e denote the CO_2 release from building, human, traffic, soil, and plants, respectively; An is the

CO_2 assimilation rate; and *P*, *ET*, *E* and *I* are the hydrological components in the model, denoting the precipitation on the ground, evapotranspiration over natural surfaces, evaporation over paved surfaces and infiltration, respectively. The in-canyon transport of energy, water, and scalar fluxes are resolved separately for each sub-facet (walls, impervious and vegetated roads, shade trees, etc.); and aggregated by areal means to compute the total urban fluxes. In this study, we programed the coupled UCM-carbon model using MATLAB® (version R2020a). It is noteworthy that all the proposed algorithms are sufficiently generic and can be coded using other programming tools.

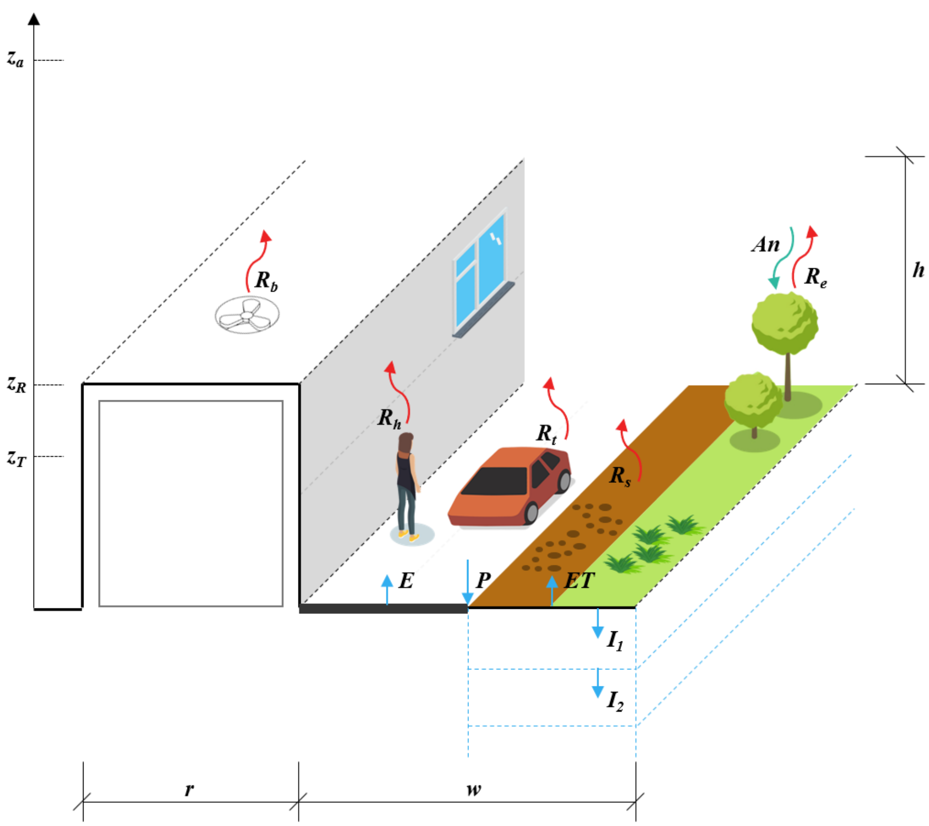

Figure 1.1 Schematic of the single-layer urban canopy model incorporating urban carbon exchange processes from biogenic, anthropogenic, and abiotic sources and sinks.

The in-canyon meteorological variables (radiation, temperature, humidity, and aerodynamic resistance) resolved by UCM are used to drive the plant physiological model for the estimation of the biogenic CO_2 fluxes in street canyon. Depending on the height of plants, those variables at prescribed elevation in the street canyon are applied for different types of plant separately. In particular, CO_2 release from soil respiration is assessed from the simulated soil temperature and moisture of the vegetated surface. Anthropogenic heat emission from the buildings is calculated by the heat conduction module of UCM, which is in turn utilized in building CO_2 release estimation in combination of the local heating profile (i.e. types of fuels and their relative contributions).

1.2 Research Objectives and Dissertation Structure

Based on the literature and identified research and knowledge gaps of urban trees identified in Section 1.1, this dissertation aims to evaluate the biogenic impact of urban vegetation on heat and carbon dynamics in the built environment and to provide decision making support for sustainable urban development amid the global climate change. In particular, the three major objectives of this dissertation area are (i) to quantify CO_2 exchange from biogenic sectors specifically in urban areas; (ii) to evaluate the impact of urban greening practices on heat and carbon dynamics; (iii) to aid the urban system design towards a more sustainable environment.

The dissertation is organized into five chapters. Chapter 2 describes the parameterization of the biogenic CO_2 exchange in cities by coupling an advanced single-layer urban canopy model with plant photosynthesis and respiration models and the evaluation of the proposed modeling framework against the field measurements. In Chapter 3, we utilize the proposed model to investigate the impact of four common urban greening practices on thermal and carbon environment on designed scenarios and examine the potential of environmental co-benefits from urban greening. Based on the experimental results in Chapter 3, Chapter 4 presents a practical and versatile approach to use the proposed model for urban system design. Materials in Chapter 2 and 3 have been published in P. Li & Z.-H. Wang 2020a and 2021b, respectively. Chapter 5 summarizes the key findings and environmental implications of this dissertation and provides recommendations for the design of urban green spaces. In the end, Chapter 5 also outlines a few potential future studies based upon the proposed algorithms and major findings of this dissertation.

CHAPTER 2

MODELING CARBON DIOXIDE EXCHANGE IN A SINGLE-LAYER URBAN CANOPY MODEL

In this Chapter, a new modeling algorithm to quantify urban biogenic CO_2 exchange (hereafter referred to as the UCM-CO_2 model) is proposed. The new model coupled an advanced UCM with photosynthesis and respiration models and is designated specifically to the developed urban land. The proposed modeling framework is tested against the field measurements from EC system over a residential area in Phoenix, Arizona. In addition, the CO_2 emission portfolio of the neighborhood is examined to illustrate the potential of CO_2 reduction from biogenic sectors in the built environment.

2.1 Model Description

2.1.1 Biogenic CO_2 Fluxes from Plant Physiological Functions

The physiological functions of plant CO_2 exchange, primarily the stomatal control, have been extensively studied in natural environment (G.J. Collatz et al. 1991; G.J. Collatz et al. 1992; C.B. Field et al. 1995; C.M.J. Jacobs 1994; R. Leuning 1995). One approach to quantify the NEE is to calculate the photosynthesis assimilation rate at canopy level using An-g_c method (estimate the carbon assimilation rate An based on stomatal conductance at the canopy level g_c), then deduct soil or ecosystem respiration based on their dependency on environmental conditions (M.U.F. Kirschbaum 1995; J. Lloyd & J.A. Taylor 1994). Here we adopt a typical physiological plant model (A.F.G. Jacobs et al. 2003; R.J. Ronda et al. 2001) and integrate it with the UCM model.

Given micrometeorological conditions, the gross primary productivity (GPP) at leaf level, A_g, is given by,

$$A_g = f(\mathrm{PAR}, T_{\mathrm{leaf}}, C_i), \tag{2.1}$$

where PAR is the photosynthetic active radiation, representing the amount of radiation that is able to drive photosynthesis; T_{leaf} is the leaf temperature; and C_i is CO_2 concentration inside of leaves. The first two inputs can be obtained from the UCM output: PAR is predicted as fraction of the irradiance incipient on leaves (either at the tree or ground vegetation sub-facet in the street canyon for plants being shade trees or urban lawns, respectively), and T_{leaf} the skin temperature of the vegetated sub-facet. The ratio of PAR to the total solar irradiance is roughly a constant at a prescribed location, ranging from 0.39 to 0.53, with a median value of 0.46 (R.T. Pinker & I. Laszlo 1992). In addition, C_i can be estimated as a fraction of external CO_2 level (C_s); the ratio between C_i and C_s is critical for plant functions (H. Wang et al. 2017). The plant regulates the ratio via stomatal opening and closure as a function of water vapor pressure deficit (C.M.J. Jacobs 1994):

$$\frac{C_i - \Gamma}{C_s - \Gamma} = \chi_{\max}\left(1 - \frac{D_s}{D_o}\right) + \chi_{\min}\frac{D_s}{D_o}, \tag{2.2}$$

where Γ is the CO_2 compensation point; D_s is the vapor pressure deficit at leaf level; D_o is the D_s at stomatal closure; and $\chi_{\max}$ and $\chi_{\min}$ are the maximum and minimum value of the ratio $(C_i - \Gamma)$ to $(C_s - \Gamma)$. The values of D_o, $\chi_{\max}$, $\chi_{\min}$, and Γ are parameterized for given types of plants analytically or empirically (R.J. Ronda et al. 2001). It is noteworthy that Γ is temperature-dependent and can be estimated using Q_{10} method as

$$V(T_{leaf}) = V_{25}Q_{10}^{(T_{\text{leaf}}-25)/10}, \tag{2.3}$$

where V is a generic temperature-dependent variable (in this case, Γ); V_{25} is the value of the variable at 25 °C; and Q_{10} is the rate of increase per 10 °C change in temperature.

Specifically, we adopt the formulas of A.F.G. Jacobs et al. (2003), R.J. Ronda et al. (2001), and C.M.J. Jacobs (1994) to determine the plant function in Eq. (2.1) as

$$A_g = \left(A_m + R_d\right)\left[1 - \exp\left(\frac{-\alpha\text{PAR}}{A_m + R_d}\right)\right], \tag{2.4}$$

where R_d is the plant dark respiration and usually calculated as a fraction of A_m; A_m is the primary productivity, given by

$$A_m = A_{m,\max}\left[1 - \exp\left(-g_m \frac{C_i - \Gamma}{A_{m,\max}}\right)\right], \tag{2.5}$$

with $A_{m,\max}$ the maximum primary productivity under high CO_2 concentration and sufficient light condition, and g_m the stomatal conductance. Here $A_{m,\max}$ and g_m are temperature-dependent, and can be estimated using the Q_{10}-type method as

$$V_k(T_{\text{leaf}}, T_1, T_2) = V(T_{\text{leaf}})\left\{1 + \exp\left[0.3\left(T_1 - T_{\text{leaf}}\right)\right]\right\}^{-1}\left\{1 + \exp\left[0.3\left(T_{\text{leaf}} - T_2\right)\right]\right\}^{-1}, \tag{2.6}$$

where V_k is again the temperature-dependent variable (in this case, $A_{m,\max}$ and g_m); $V(T_{\text{leaf}})$ is the function in Eq. (2.3); and T_1 and T_2 are empirical parameters for given types of plants.

To find the gross primary production at canopy level, CO_2 uptake at leaf level needs to be integrated over entire leaf surface area, as

$$A_{g,c} = \int_0^{LAI} A_g dL = A'_m\left(\text{LAI} - \frac{E_{\text{int}}}{K_x}\right), \tag{2.7}$$

where $A_{g,c}$ is the assimilation rate at canopy level; $A'_m = A_m + R_d$; LAI is the leaf area index; K_x is the extinction coefficient; and E_{int} represents the overall leaf density from top to bottom of the canopy, calculated as

$$E_{\text{int}} = \text{Ei}\left[\frac{\alpha K_x \text{PAR}}{A'_m}\exp\left(-K_x \text{LAI}\right)\right] - \text{Ei}\left[\frac{\alpha K_x \text{PAR}}{A'_m}\right], \tag{2.8}$$

with Ei [•] the exponential integral.

Plants that have different photosynthesis pathways will respond distinctively in the same meteorological condition. According to the number of carbons in the intermediate compounds during photosynthesis, the major plant types on the earth are C_3 and C_4. C_3 plants are the dominant plant types worldwide, including rice, wheat, soybeans, and all trees. C_4 plants are less common and usually present in hot and arid climate regions for its adaptation to water stress (M.V. Lara & C.S. Andreo 2011). Due to the distinctive plant physiological functions, the contribution from C_3 and C_4 plants needs to be quantified separately. The total carbon assimilation from plants (An_{tot}) is given by:

$$An_{tot} = F_{v,3} A_{g,c,3} + F_{v,4} A_{g,c,4}, \tag{2.9}$$

where $F_{v,3}$ and $F_{v,4}$ are the vegetation fraction for C_3 and C_4 plant to the total study area, respectively; and $A_{g,c,3}$ and $A_{g,c,4}$ are the assimilation rate calculated from Eq. (2.7) for C_3 and C_4 plant, respectively. Typical values of the empirical parameters for GPP estimate for C_3 and C_4 plants are listed in Table 2.1. For the built environment, the accurate estimation of vegetation cover is rather difficult, not to mention the relative fraction of plant types. We therefore need to resort to remote sensing dataset on vegetation indices to identify the variation of vegetation fraction in total. In this case, we proposed an algorithm to estimate the total vegetation fraction based on the readily available remote sensing LAI and vegetation fraction dataset with the more commonly used dataset with moderate resolution (300 m ~ 1 km). In general, the peak of LAI reflects the rapid biomass accumulation in the previous growing stage, indicating the activeness of plants in photosynthesis and CO_2 absorption. Therefore, in this study, we estimate the plant phenology from the observed vegetation coverage and the time derivative of LAI. We calculate the effective fraction as the total vegetation fraction in the plant physiological model, given by:

$$EF_v(t) = \frac{L' - L'_{\min}}{\overline{L'} - L'_{\min}} F_v(t), \tag{2.10}$$

where EF_v is the effective fraction for vegetation cover; F_v is the observed vegetation from remote sensing dataset; $L' = d\mathrm{LAI}/dt$ is the time derivative of LAI; and the overhead bar denotes the time average.

Furthermore, individual fractions for C_3 and C_4 plant need to be estimated based on the knowledge of local species and lawn management strategies. For example, C_4 plants will first become active in the early spring, growing fast through the summer and stop functioning by the late fall, while C_3 plants could be active all year round without an apparent peak (C.J. Still et al. 2003). For practical lawn management, grasses are often mowed before the dormant season to promote the growth in the next spring, leading to the reduction of carbon assimilation during winter months.

Table 2.1 Parameters for Plant Physiological Model

C_3				
χ_{max}	0.89			
α_d (k Pa^{-1})*	0.07			
α_0 (mg J^{-1})*	0.036			
	V_{25}	Q_{10}	T_1 (K)	T_2 (K)
Γ (mg m^{-3})	68.5 ρ_a	1.0		
g_m (mm s^{-1})	7.0	2.0	278	301
$A_{m,\max}$ (mg m^{-2} s^{-1})	2.2	2.0	281	311
C_4				
χ_{max}	0.85			
α_d (k Pa^{-1})	0.015			
α_0 (mg J^{-1})	0.029			
	V_{25}	Q_{10}	T_1 (K)	T_2 (K)
Γ (mg m^{-3})	4.3 ρ_a	1.0		
g_m (mm s^{-1})	17.5	2.0	286	309
$A_{m,\max}$ (mg m^{-2} s^{-1})	1.7	2.0	286	311

*α_0 is the light use efficiency under low light condition; a_d is a fitted parameter defined in R.J. Ronda et al. (2001).

2.1.2 Soil and Plant Respiration

The carbon release from bare soils in urban areas is often neglected due to the perception that soils constitute a minor source of CO_2 as compared to anthropogenic emissions. In fact, soil respiration is a major contribution to atmospheric CO_2 in manmade landscapes with irrigation and fertilization. Specific urban garden soils with enriched organic matter and nitrogen are often used in cities to promote plant growth. S.M. Decina et al. (2016) reported that the soil respiration in residential areas with active landscaping management is 2.2 times higher than that of urban forests. The total CO_2 flux from soils is comparable with fossil fuel emission in summer months.

Bare soil respiration is primarily regulated by soil temperature (T_s) and soil water content (θ). Though other factors such as the elevation of organic matters or nitrogen levels, air pressure changes, etc. will also influence the respiration rate, their contribution is considered minor or implicitly embedded into changes of T_s and θ (Y. Luo & X. Zhou 2006). Like plant physiology, Q_{10}-type methods are often used for temperature-dependent relation in soil respiration. The default range of T in conventional Q_{10} method (Eq. (2.3)) is capped below 45 °C, which is applicable for air temperature in most climate regions. However, in arid environment, surface temperature in hot summers can be as high as 55 °C, in which case the soil respiration will be suppressed because the major contributors of respiration, i.e. microbial activities and plant root respiration, are no longer at the optimum functional temperature (Y. Luo & X. Zhou 2006). Using a monotonic function, like the one in Eq. (2.3), will lead to a large bias under extreme temperatures. Alternatively, M.U.F. Kirschbaum (1995) proposed a temperature dependency model to estimate soil respiration due to biotic and abiotic processes, by admitting an optimum temperature as an additional variable. Instead of using a fixed value for Q_{10}, this model accounts for the change of Q_{10} with temperature, as

$$Q_{10}(T) = \exp\left[10\beta\left(1 - \frac{T}{T_{opt}}\right)\right], \tag{2.11}$$

where β and T_{opt} are empirically fitted parameters. Combined with Eq. (2.3) and the dependency on soil moisture, the soil respiration rate can be obtained as

$$R_s(T_s, \theta) = f(\theta) R_{25} Q_{10}(T_s)^{(T_s - 25)/10}, \tag{2.12}$$

where R_s and R_{25} are the soil respiration rate under T_s and 25 °C; and $f(\theta)$ is the respiration reduction function due to water stress. Different forms of $f(\theta)$ can be found in literature for urban evapotranspiration (P. Li & Z.-H. Wang 2019; Z.-H. Wang et al. 2013) and soil respiration (M.U.F. Kirschbaum 1995). Typical linear and non-linear reduction curves for estimating the evapotranspiration and respiration rates are

$$f_2(\theta) = \max\left[0, \min\left(1, \frac{\theta - \theta_w}{\theta_{fc} - \theta_w}\right)\right], \quad (2.13)$$

$$f_3(\theta) = 2f_2(\theta) - f_2^2(\theta), \quad (2.14)$$

$$f_4(\theta) = 1 - e^{-10.563 f_2(\theta)}. \quad (2.15)$$

Figure 2.1 shows the variation of Q_{10} and soil respiration rate with ambient temperatures. It is clear that the soil respiration rate decreases when the temperature exceeds the optimum value.

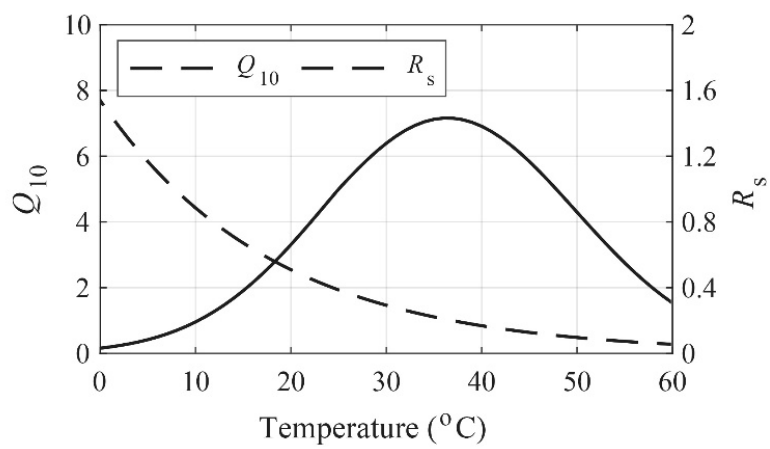

Figure 2.1 Temperature dependency of Q_{10} and soil respiration rate (plotted using T_{opt} = 36.9 °C, B = 0.204, R_{25} = 1.0).

Plant respiration is usually evaluated empirically using statistical regressions of field measurements. In the long run, the relation between the ecosystem respiration and its GPP is usually linear across various types of land cover (D. Qun & L. Huizhi 2013; W. Yuan et al. 2011), which is conventionally used in the assessment of ecosystem services. An alternative approach considers that the instantaneous respiration rate is controlled by plant physiological and micrometeorological conditions, which can be explicitly formulated (J.M. Norman et al. 1992; Y. Qi et al. 2010). Both approaches require the measurement of plant respiration at night when the photosynthesis in inactivate. However, in practice, it is difficult to exclude soil respiration from the measured plant respiration. Therefore, ecosystem respiration is usually used to represent the total CO_2 efflux from vegetated surface, including both soil and plant respiration. Here we adopt the formula derived over a grassland to represent the ecosystem respiration R_e, for low vegetation surfaces (J.M. Norman et al. 1992),

$$R_e = \left(a + b\mathrm{LAI}\right)\theta_{10} e^{c\left(T_s - T_{s,\mathrm{ref}}\right)}, \tag{2.16}$$

where $a = 0.159$, $b = 0.064$, $c = 0.054$, and $T_{s,\mathrm{ref}} = 27.7$ ºC are empirical coefficients fitted from 900 on-site observations over grassland and θ_{10} is the soil moisture at 10 cm below the surface.

2.1.3 Abiotic CO_2 Flux

The abiotic CO_2 fluxes in urban areas are generated from burning of fossil fuels from two major sources including (1) the transportation sector (vehicular emission) and (2) the building sector (heating and/or cooking). Conventionally, the abiotic $AnCO_2$

emissions were estimated from the energy consumption inventories. For example, the on-road traffic release can be calculated from the local traffic volume, vehicle types, combustion efficient, and the fuel economy. We can then make a crude estimate of the carbon release due to heating and cooking using the purchasing record of the fuels (wood, gas, oil, etc.). This method is heavily labor- and cost-consuming for locality-based data collection and results in limited data availability across different regions with constant spatiotemporal discontinuity.

The last two decades have seen much effort devoted to the mapping of global or regional CO_2 level or efflux. The current advances in mapping technology combine the bottom-up (inventory by sectors) and top-down (spatial distributed dataset from remote sensing imagery) method, which enables the mapping of CO_2 efflux variability over time and space at high resolution. For example, Vulcan Project version 2 (Vulcan v2, K.R. Gurney et al. 2009) provides CO_2 release from traffic over the contiguous U.S. with 10 km spatial and hourly temporal resolution. However, Vulcan v2 only covers the year of 2002, and the spatial resolution is still too coarse to match the footprint of EC measurements. To resolve this issue, we normalize the hourly release to its annual total to obtain the hourly release factor through the year of 2002 and assumed no interannual variation of the factor. The carbon emission is then estimated using the derived release factor multiplied the total annual release of the year of the interest. To validate the assumption, the diurnal variation is compared to the Carbon Tracker 2019 (A.R. Jacobson et al. 2020) with hourly temporal resolution. The seasonal and annual total release are retrieved from Open Data Inventory for Anthropogenic CO_2 (ODIAC, T. Oda et al. 2018) and Database of Road Transportation Emissions (DARTE, C. Gately et al. 2019). Table

2.2 summaries the spatiotemporal resolution and coverage of the available gridded dataset of CO_2 emission used in this study.

The CO_2 emission from buildings can be estimated from the inventory data of building heat release or from the UCM output of the heat exchange via the building sub-facets. We assess the equivalent CO_2 emission based on the emission factor, defined as the amount of fossil fuel required for a unit of heat. For example, with the building interior temperature known, the UCM can quantify the heat exchange between the building envelop and its ambient environment. The equivalent CO_2 emission can be obtained using the building-environment heat exchange multiplied the emission factor, according to the type of fuel and heating efficiency. A summary table of the emission factors for commonly used fuel can be found in M. Goret et al. (2019).

Table 2.2 Summary of Gridded Dataset for CO_2 Release

	Resolution		**Coverage**	
Product	**Temporal**	**Spatial**	**Temporal**	**Spatial**
ODIAC	Monthly	1/120°	2000-2018	Global
DARTE	Annual	1/80°	1980-2018	U.S.
Vulcan v2	Hourly	10 km	2000-2018	U.S.
Vulcan v3	Annual	1 km	2010-2015	U.S.
Carbon Tracker 2019	3-hour	1°	2000-2017	Global
Hestia	Hourly	1 km	2010-2015	LA basin

2.1.4 Human Respiration

In densely populated areas, human activities can be a significant source of CO_2 emission. Here we give a simple estimation of the respiration rate from a single person. At normal activity level, the average tidal volume (volume of air per breath) is 500 ml to 750 ml, with CO_2 concentration level around 3.8% to 4% per breath (K.E. Barrett et al.

2009). A person regularly breathes 12 to 15 times per minutes. Following these assumptions, the respiration rate will be [7.52, 14.85] mg CO_2 s^{-1} per person. The estimation is in a reasonable range compared to the values used in the other studies (16.04 in B. Koerner and J. Klopatek (2002), 2.19 in Q. Cai et al. (2018), 8.87 in M. Goret et al. (2019)). Total CO_2 flux from human respiration will be calculated using the mean level per person times the population density retrieved from Gridded Population of the World (GPWv4). The hourly variation of respiration factors is used to represent changes in the population density in different built environments during a day (Figure 2.2). For example, during working hours, the pollution density (hence the factor of human respiration) is expected to reduce in residential areas, whereas it increases at urban cores where most office buildings locate. No seasonal variation of population is considered.

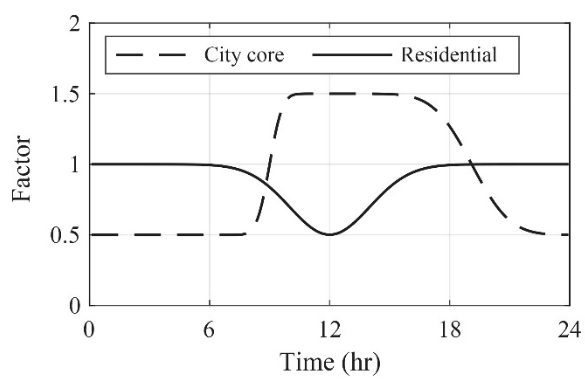

Figure 2.2 The diurnal variation of hourly factors of human Respiration at city core (dashed line) and residential area (solid line)

2.2 Results and Discussion

2.2.1 Model Test and Evaluation

The proposed model was first tested against field measurements by an EC located in west Phoenix, Arizona, USA (33.483847 °N, 112.142609 °W). The EC tower recorded four-component net radiation, 3D wind field, air temperature, humidity, CO_2 concentration, and pressure at 10 Hz frequency. Both soil temperature and moisture were recorded at three depths (5 cm, 15 cm, 30 cm) below the ground. Additional soil temperature measurement was also made at 2 cm below the ground. The original 10 Hz atmospheric measurements were processed, quality-controlled, and integrated at 30 min intervals with no gap filling. In this study, we used the measurements recorded from January 1, 2012 to May 28, 2013 (513 days) for subsequent analysis (available at https://sustainability.asu.edu/caplter/data/view/knb-lter-cap.649/).

The source area of the flux tower covered a typical residential area of single-family houses (J. Song et al. 2017). Most lots in the study area have small front and backyard spaces with automated irrigation system. The overall land cover within 1 km^2 of the EC tower were 48.4% impervious surfaces (26.4% building and 22.0% road), 36.8% bare soil, 14.6% vegetation, and 0.1% water pool (W.T.L. Chow et al. 2014).

A comprehensive list of input parameters used in the UCM model is shown in Table 2.3. The street and building aspect ratios are estimated from Quickbird remote sensing imagery of the study site (W.T.L. Chow et al. 2014). Aerodynamic roughness and hydrothermal properties of buildings, soils, and pavements are adopted from previous studies at the study site or similar residential areas in Phoenix metropolitans (J. Song & Z.-H. Wang 2015; 2016; J. Yang & Z.-H. Wang 2014) with detailed parameter sensitivity study. We first calibrated the UCM by comparing the model predictions and meteorological measurements of net radiation R_n, sensible heat H, and latent heat LE, during the period of May 13, 2012 00:00 to May 27, 2012 23:30 (15 days). The results are shown in Figure 2.3, with the root mean squared error (RMSE) of 24.5 Wm^{-2}, 28.3 Wm^{-2}, 21.6 Wm^{-2} for R_n, H, LE, respectively.

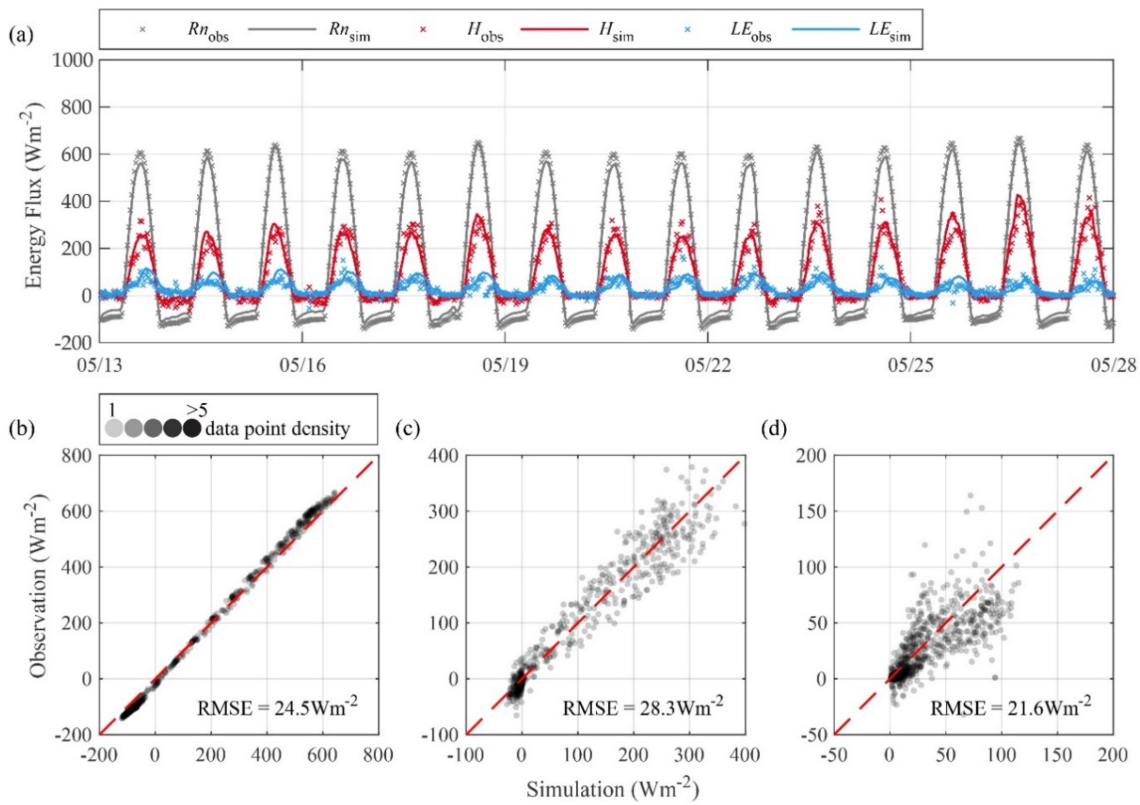

Figure 2.3 Results of model calibration (May 13 2012 00:00 to May 27 2012 23:30). (a) Timeseries of energy fluxes, and the comparison of simulation to observation at half-hour interval for (b) Net radiation Rn, (c) Sensible heat H, and (d) Latent heat LE.

Table 2.3 Physical Properties of the Study Site

Site Properties	
Roof level (m)	4.5
Reference height (m)	22.1
Normalized roof height (-)	0.13
Normalized roof width (-)	0.4
Normalized road width (-)	0.6
Thickness of roof (m)	0.3
Thickness of wall (m)	0.2
Roughness length for momentum for roof (m)	0.01
Roughness length for momentum for canyon (m)	0.05
Roughness length for heat for roof (m)	0.001
Roughness length for heat for canyon (m)	0.005
Street canyon orientation (rad)	$3/8\ \pi$
Latitude (rad)	0.5844
Longitude (rad)	1.9573
Soil Properties	
Saturation hydraulic conductivity (m s^{-1})	3.4×10^{-5}
Residual soil water content (m^3 m^{-3})	0.08
Saturated soil water content (m^3 m^{-3})	0.35
Slope of soil water retention curve, *b*	4.50
Soil layer thickness (m)	0.15
Surface Properties	
Roof (gravel)	
Albedo	0.17
Emissivity	0.95
Thermal conductivity (W K^{-1} m^{-1})	0.60
Heat capacity (MJ K^{-1} m^{-3})	1.00
Wall (wood, glass)	
Fractions	0.90, 0.10
Albedo	0.17, 0.50
Emissivity	0.90, 0.95
Thermal conductivity (W K^{-1} m^{-1})	1.30, 1.30
Heat capacity (MJ K^{-1} m^{-3})	0.80, 1.20
Road (soil, paved, vegetation)	
Fractions	0.35, 0.50, 0.15
Albedo	0.15, 0.40, 0.20
Emissivity	0.76, 0.90, 0.95
Thermal conductivity (W K^{-1} m^{-1})	2.20, 2.20, 1.50
Heat capacity (MJ K^{-1} m^{-3})	0.80, 0.45, 1.20

Once calibrated, the parameter space of the UCM is fixed and applied to the consequent study period. We then compared the model results against field measurements for the entire study period (513 days). Figure 2.4 shows the results of comparison for all available 30-min data points in scattered plots. The mean bias error (MBE) for R_n, H, and LE are 0.3 Wm^{-2}, 5.1 Wm^{-2}, and 5.2 Wm^{-2}, respectively, and RMSE values of 24.7 Wm^{-2}, 20.8 Wm^{-2}, and 24.6 Wm^{-2}, respectively. The model performance on R_n, H, and LE predictions is comparable to those reported in a prior study at the same site (N. Meili et al. 2020). It is also noteworthy that the surface energy balance needs to be strictly observed in the UCM algorithm, whereas in measurements energy imbalance is the norm (P. Li & Z.-H. Wang 2020b). Thus it is not surprising that in general the model tends to overestimate sensible and latent heat to account for the surface energy residual.

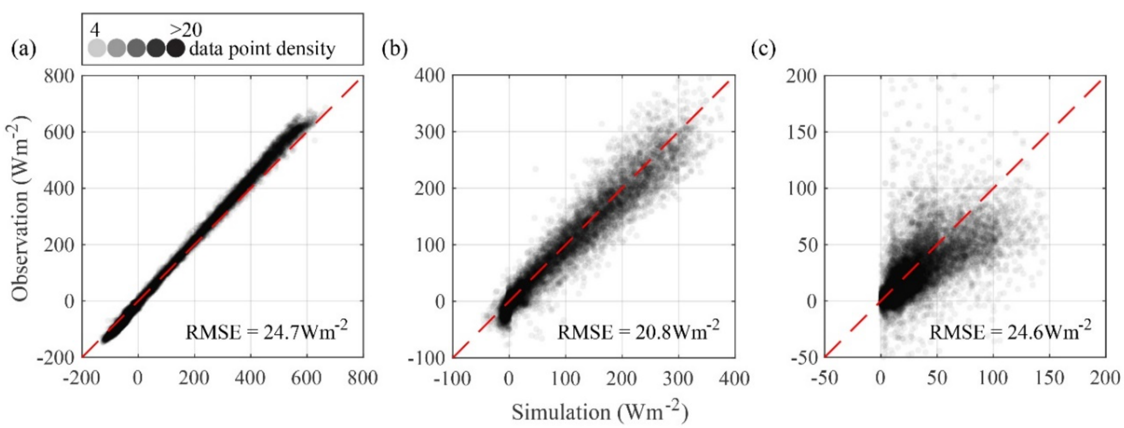

Figure 2.4 The comparison of model simulation to EC observation of (a) Net radiation R_n, (b) Sensible heat H, and (c) Latent heat LE, from January 01, 2012 to May 28, 2013

In addition, we compared predicted and observed diurnal variations of R_n, H, and LE fluxes averaged over individual months to illustrate their temporal variability. The results are shown in Figure 2.5; it is clear that the model captures the temporal evolutions of these heat fluxes well. Note that in general the peaks of sensible heat slightly lag behind those of net radiation. This hysteresis effect is physical, as being observed experimentally and proved analytically (J. Song et al. 2017; T. Sun et al. 2013), and in turn, influences plant function as the optimum temperature encountered with reduced PAR. Moreover, we also presented the model results of the canyon air temperature, humidity, ground temperatures, and solar irradiance at roof and ground level (Figure 2.6). Note that the solar irradiance at ground level is cut off by 40% as compared to the one at roof level. These results will be used to predict the biogenic CO_2 flux generated by plant physiological functions. No evaluation against observation was conducted due to the absence of field measurements of these variables.

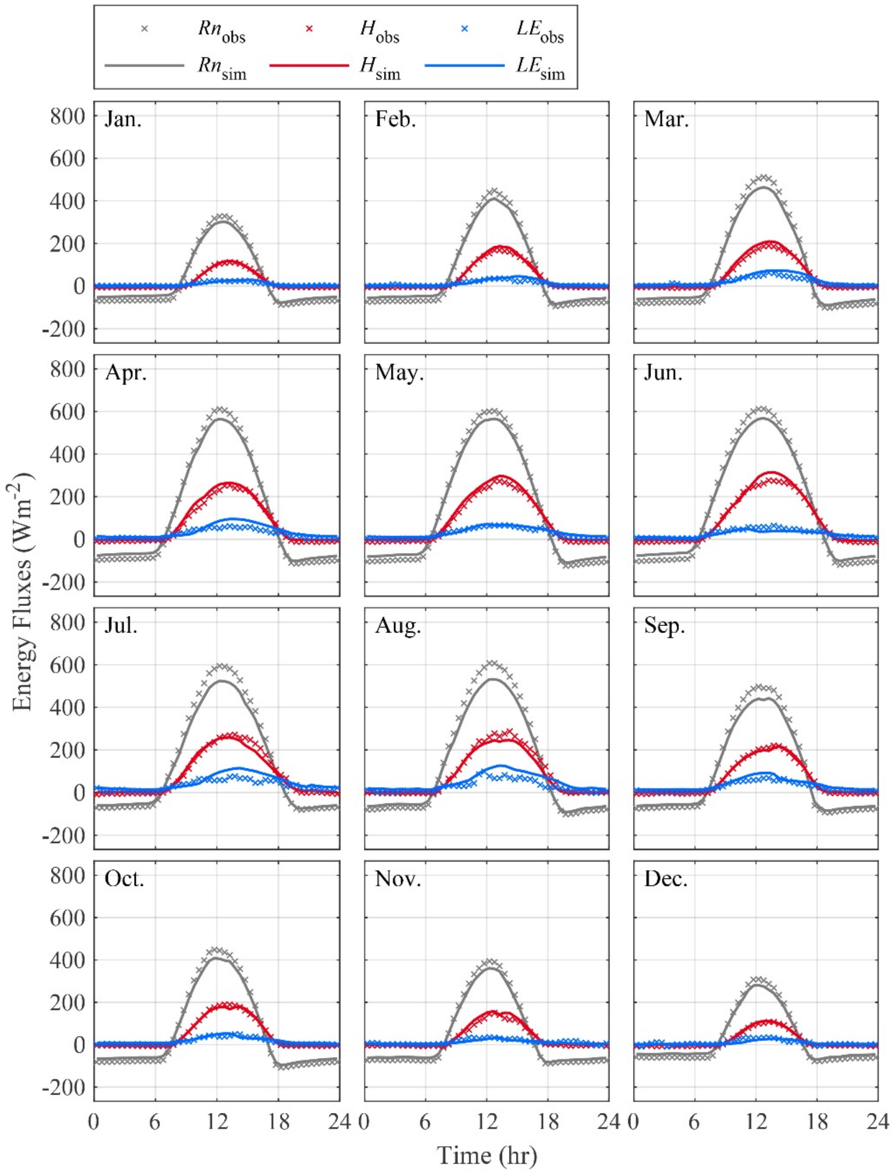

Figure 2.5 The diurnal variation of *Rn*, *H*, and *LE* (calculated from monthly mean).

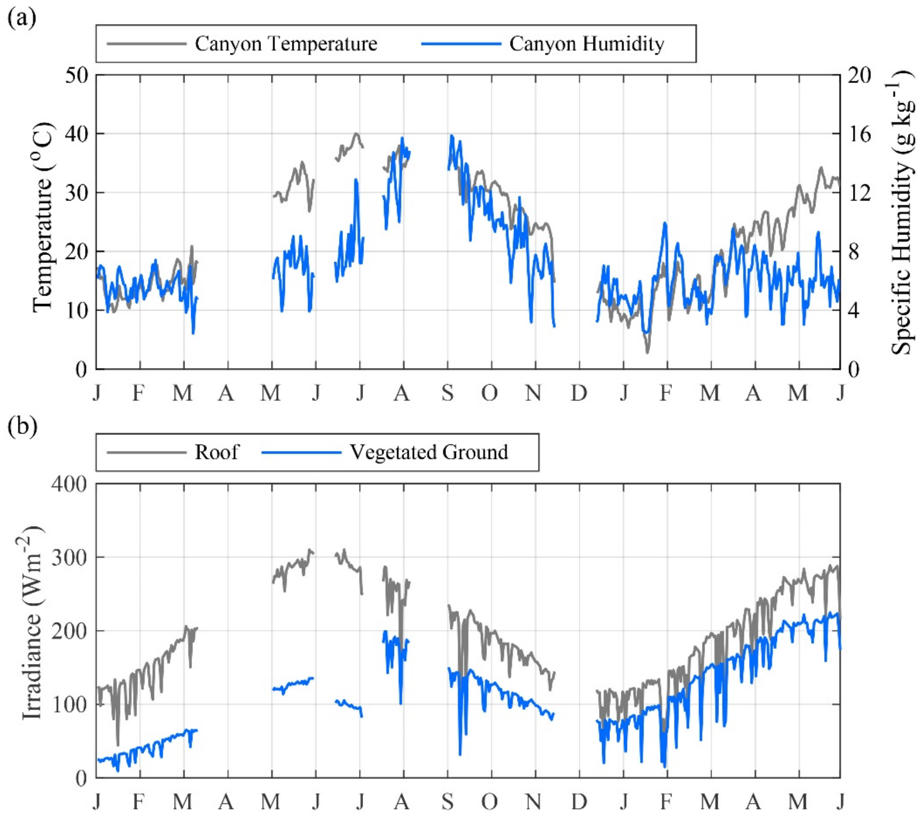

Figure 2.6 Results of model simulations of (a) Temperature and humidity at canyon level, and (b) Solar irradiance at roof and ground level from January 01, 2012 to May 28, 2013 at the study site

2.2.2 Biogenic CO_2 Exchange of Urban Plants

Plants in Phoenix area have distinct photosynthesis patterns, mainly consisting of C_3 trees and C_4 bushes or grasses. The fraction of C_4 plants in Phoenix area is generally estimated to be 0.4 to 0.5 of total vegetation area (C.J. Still et al. 2003), making C_4 plants a non-negligible contributor of carbon uptake. Specifically, many residential lots in the study area use a C_4 plant, Bermuda grass (*Cynodon dactylon*) as the yard lawn (W.T.L. Chow et al. 2014). Considering the difference in vegetation types and their typical locations in urban canopies, irradiance, temperature, and humidity at different levels are used in the proposed plant physiological model. The physiological function of C_3 trees is simulated under the meteorological conditions at the roof level, while the ground level meteorological conditions are used for C_4 grass. In particular, the solar irradiance is the primary source of PAR, and the ratio of 0.46 (PAR to total irradiance) is used in this study. Temperatures and humidity in street canyons are obtained from the UCM predictions and used to drive the plant physiological model and estimate the soil respiration.

To aggregate the leaf level CO_2 uptake to the canopy level, we obtain the vegetation fraction and its seasonal dynamics from remote sensing datasets. At the study site, the urban vegetation fraction (14.6 %) was estimated from a single frame of QuickBird satellite image based on local land cover classification at 2.4 m resolution (W.T.L. Chow et al. 2014). Despite of its high spatial resolution, the temporal dynamics is underrepresented. In this case, we use the Copernicus Global Land Services (CGLS, https://land.copernicus.eu) 10-day, 1 km^2 resolution data to find the seasonal variation of vegetation coverage and LAI. We used the observed LAI value divide the fraction of green vegetation cover (CGLS-FCOVER) to calculate the apparent LAI value over the study area. The annual mean apparent LAI in 2012 is 3.4. Figure 2.7 shows the seasonal variation of LAI and vegetation coverage from CGLS over the study area. The LAI is bimodal and peaks in April and between August to September, corresponding to the optimum growing condition in warm spring and late water-rich monsoon season, respectively. The latter peak in August and September is contributed by the phenology and biomass accumulation of Bermuda grass during summer, as its optimum growing temperature is [24, 37] °C. The fractions of C_3 and C_4 plants used in plant physiological model (Figure 2.7) are first set based on the derived total fraction and characteristics in phenology, and then fine-tuned for the best model performance in the prediction of total CO_2 exchange. Other model parameters used in plants physiological model are listed in Table 2.1. The extinction coefficient, K_x in Eq. (2.7) is set to 0.5 for both C_3 and C_4 plants, according to (L. Zhang et al. 2014).

The diurnal cycle of total plant uptake for each month is shown in Figure 2.8. The CO_2 uptake only occurs during daytime when photosynthesis is active to assimilate carbon. During hot months, the peak of canyon temperature lags several hours behind the peak of the irradiance, depending on the ET rate (Z.-H. Wang 2014). While the out-phased irradiance-temperature evolution tends to reduce the optimum rate of CO_2 uptake, the active synthesis, driven by both PAR and heat, will be prolonged due to the hysteresis so to achieve overall greater daily carbon assimilation. Also note that the CO_2 uptake in November shows a sharp peak at noon and decreases rapidly in the afternoon, because the narrowed phase lag between radiation and canyon temperature. On the other hand, plants are barely functional in December and January, leading to flat CO_2 uptake; the inactiveness matches the low ET rate measured in the same period. Within the total CO_2 uptake, 74% comes from C_3 plant primarily due to its consistent photosynthesis rate throughout a year and the higher carbon assimilation rate at its optimum condition for growth. In contrast, C_4 plants account for 26% of annual uptake with the maximum contribution at July and August for its adaptation to high temperature (Figure 2.9).

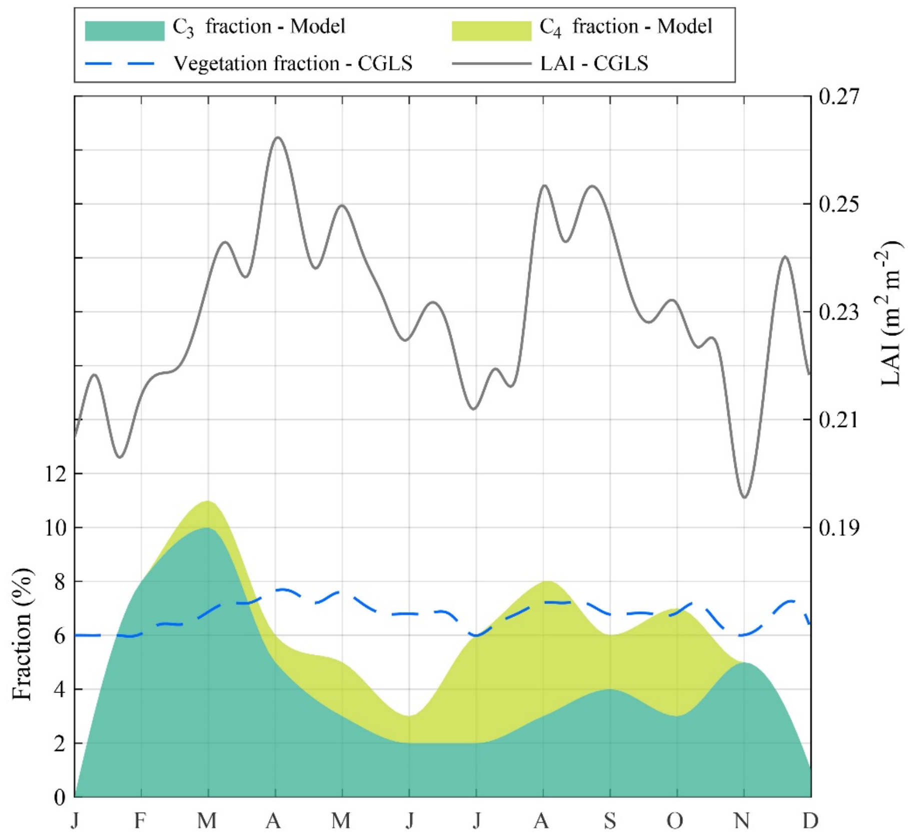

Figure 2.7 Seasonal variation of LAI (black solid line) and vegetation fraction (blue dash line) obtained from CGLS at the study site in 2012. Shaded green area show the total vegetation fraction used in plant physiological model.

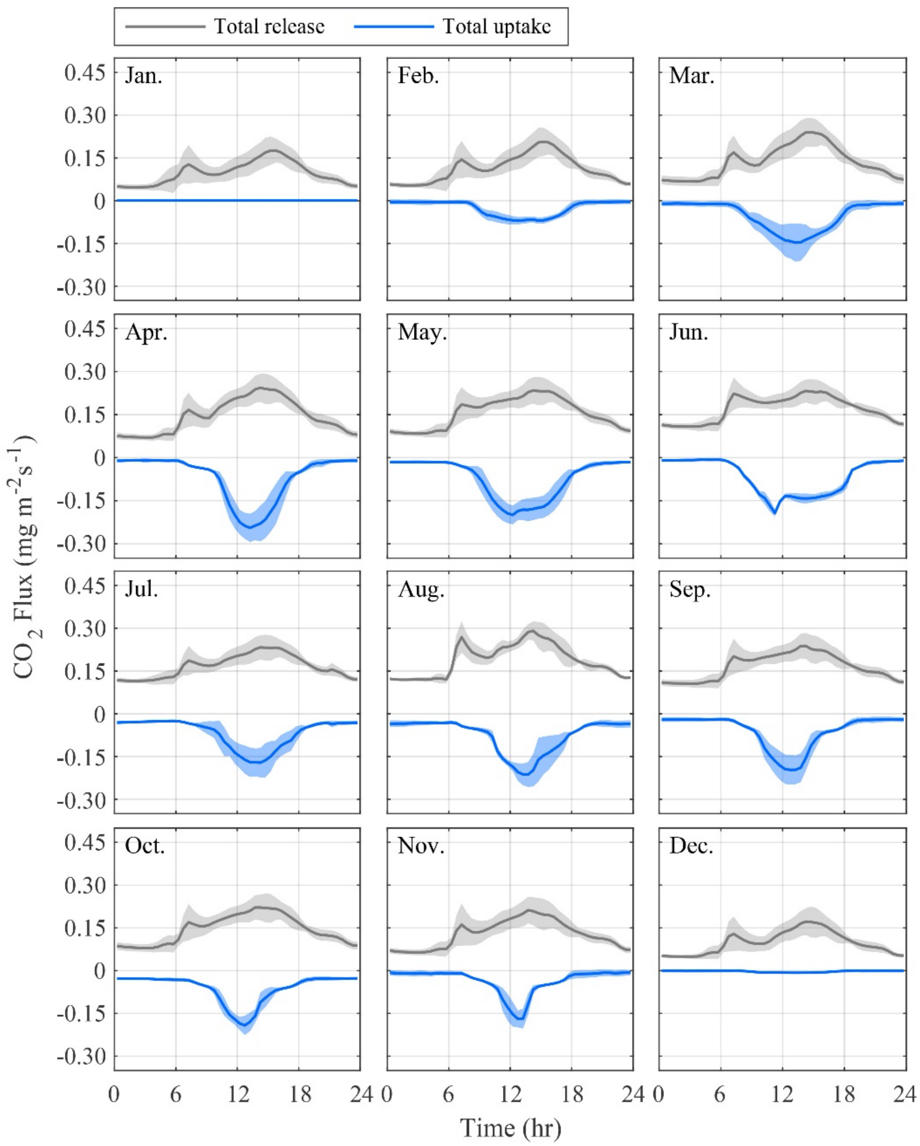

Figure 2.8 Diurnal variation of average modeled CO_2 release (black) and uptake (blue) for each month over the study period. The shaded area shows one standard deviation ($\pm 1.0\sigma$) from the monthly mean (solid lines).

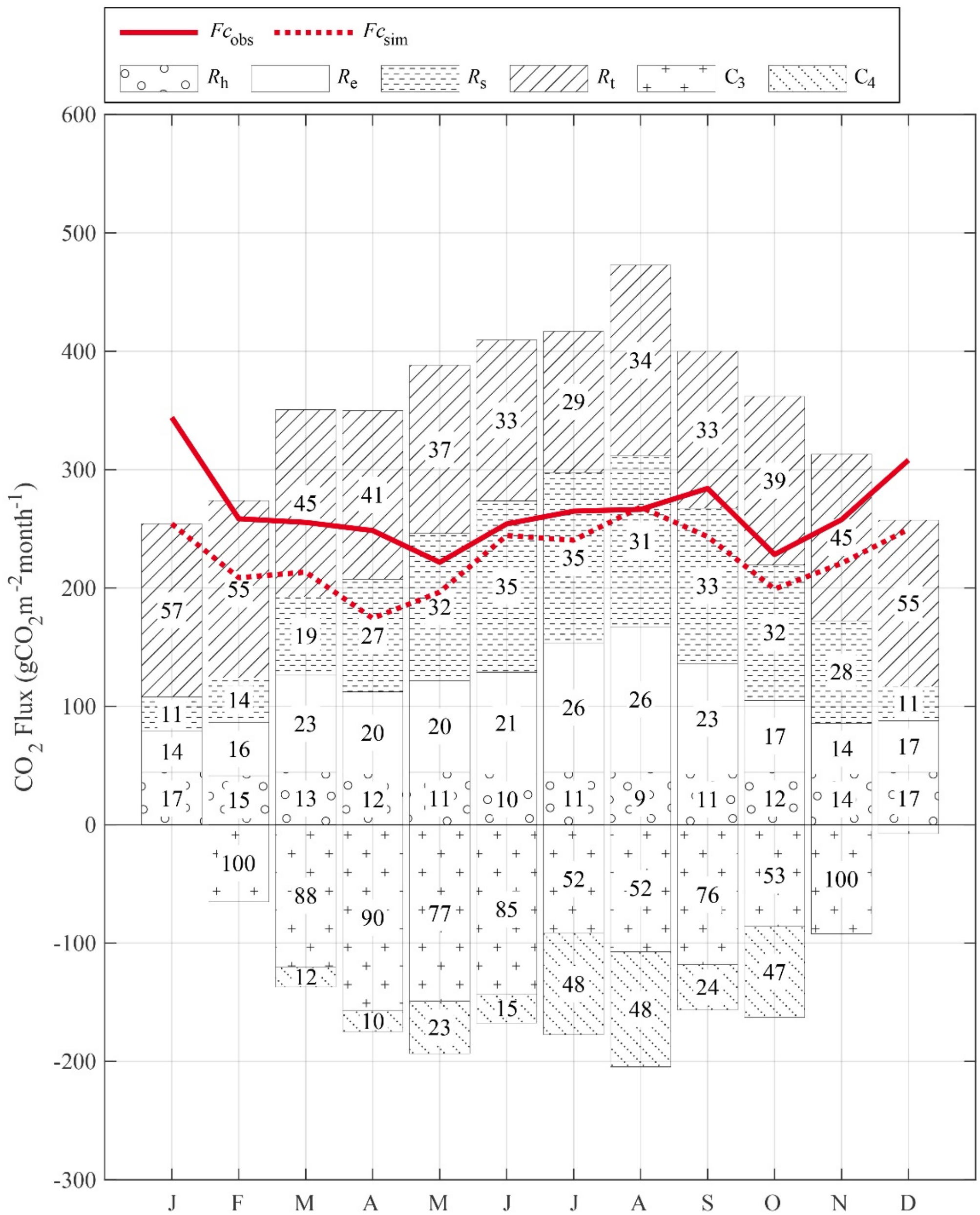

Figure 2.9 Seasonal Variation of the net CO_2 Flux from the observation (Fc_{obs}, solid line) and model simulations (Fc_{sim}, dash line) over the study area. C_3 and C_4 denote the CO_2 uptake by C_3 and C_4 plant, respectively. The filled bars represent the composition of release and uptake in each month. The values on the bars show the percentage of release or uptake from each source.

The CO_2 release from vegetated area is quantified by Eq. (2.16). It is noteworthy that the monthly ecosystem respiration to monthly GPP at the study site followed the linear relation reported from W. Yuan et al. (2011) and D. Qun and L. Huizhi (2013). The correlation coefficient is 0.53 ± 0.11 at monthly scale and 0.56 as the annual average, meaning 56% of CO_2 absorbed by vegetation released back to the atmosphere. The annual net CO_2 exchange from plants is -668.8 $gCO_2\ m^{-2}$, negative sign indicating the net uptake.

2.2.3 Soil Respiration

Using variable Q_{10} method in Eqs. (2.11) & (2.12), soil respiration is calculated using soil temperature and water content. The factor $f_3(\theta)$ is selected from Eq. (2.14) as it gives the best performance at the study site. The annual total soil respiration is 1147.0 $gCO_2\ m^{-2}$. This value is very close to the observational value 1112.5 $gCO_2\ m^{-2}$ reported in B. Koerner and J. Klopatek (2002) as the annual mean soil respiration in Phoenix residential area. However, the value is significantly lower than soil respiration obtained from low density residential area near Boston (7395.8 $gCO_2\ m^{-2}$ S.M. Decina et al. (2016)). The difference can be possibly attributed to the dry environment in Phoenix. Most houses in arid environment used xeric landscape design to save water from irrigation. Gravels, sometimes bare soils, take a large portion of xeriscaping, leading to the reduction of subsurface root uptake. Less irrigation and fast evaporation can also cause water deficit in soil and lower the biotic activeness. Hence, from the modeling perspective, R_{25} needs to be adjusted to account for changes in land covers and climate regions.

The seasonal variation in soil respiration is primarily determined by temperature. Though the soil respiration is suppressed via reduced Q_{10} during hot months, greater rate of soil respiration occurs during June to August (Figure 2.9). Soil respiration accounts for over 30% of total CO_2 release during May to October, comparable to traffic emissions in the residential area. During winter months, only ~12% of CO_2 release is from soil, making it the smallest source of CO_2. Despite of the significant seasonal variation, the soil respiration comprises 27% of total annual release at the study site, greater than the total CO_2 release from the vegetated surface (20%). In addition, shading and evaporative cooling provided by urban plants (especially tall trees) reduce the soil temperature, leading to unfavorable conditions for respiration. Considering the CO_2 uptake capability of urban plants, urban greening, viz. converting bare soils to vegetated landscapes, is an effective means to provide the environmental co-benefits of mitigating both heat and CO_2 emissions in the built environment.

2.2.4 Anthropogenic CO_2 Release

The anthropogenic CO_2 release is primarily determined by human activities and their working schedules. The modeling results are shown in Figure 2.10, where the weekly factor is defined as the ratio of hourly release to the total release of the week, and the annual factor is the ratio of the total weekly release to annual release. The variation is more related to the time of a day (diurnal cycle) rather than to the day of the year (seasonal variation) (Figure 2.10a). The diurnal variation of traffic release at the study site during workdays is apparently bimodal, corresponding to rush hours in the morning and evening traffic. The bimodal trend becomes less manifest in weekends and holidays (Figure 2.10b). The seasonal variability of traffic carbon emission is small, as shown in Figure 2.10c), where the monthly average value is 142.5 ± 11.0 gCO_2 m^{-2} with the maximum in August (160.9 gCO_2 m^{-2}) and the minimum in July (119.2 gCO_2 m^{-2}), respectively. It is noticeable that overall, the traffic emissions constitute the largest contributor to the annual total release in the study area.

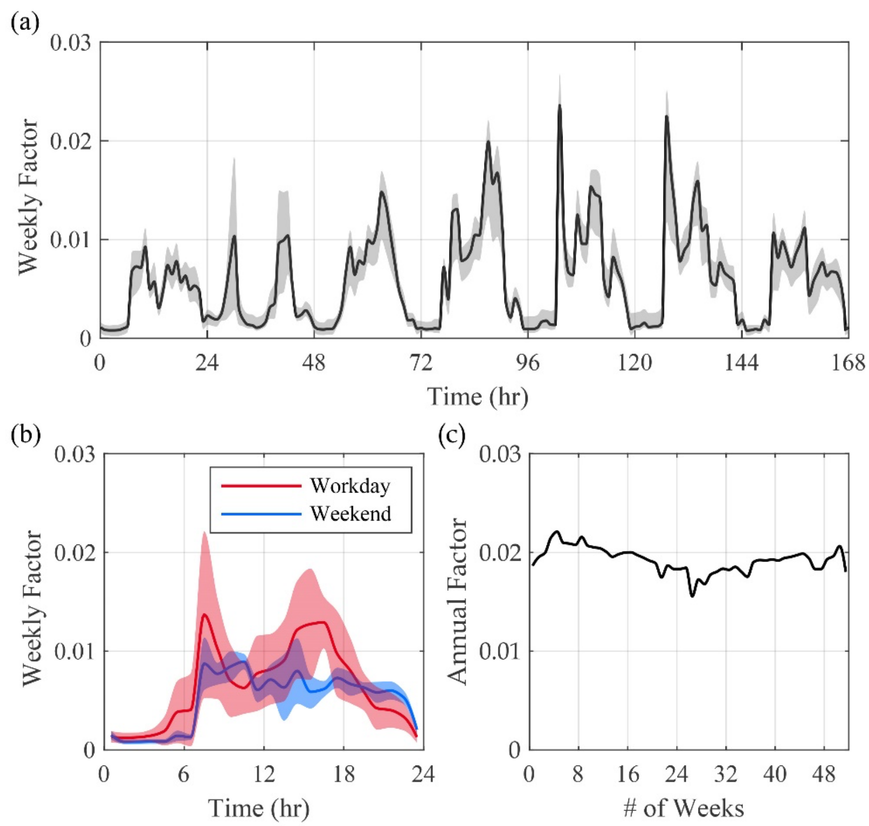

Figure 2.10 Traffic release factors. (a) Weekly factor derived from Vulcan v2 hourly data at the study area; (b) the average release factors for workday (red) and weekend (blue); (c) the intra-annual variation of the release Factor. Shade area in (b) represents one standard deviation (±1.0σ) from the mean value.

According to GPWv4 statistics, the population density of the study area is 1578 person per km^2 in 2010 and 1758 person per km^2 in 2015. We used linear interpolation to estimate the population density in 2012 and 2013. The residential curve (Figure 2.3) enhanced the bimodal shape in the diurnal cycle of the CO_2 release from the anthropogenic sources. The average annual release from human respiration is 552.7 gCO_2 m^{-2} and accounts 12.3% of total CO_2 release. Note that here the human respiration rate is estimated based on an average adult at the normal activity level. In general, the level of human respiration varies with different activities, ages, and genders, but its variability is comparatively lower than that of other contributors (e.g. plant functions). For more accurate estimation of human respiration, the population pyramid (age and gender distribution) of the study area is needed; the availability of such statistics, however, is often very scarce at high spatial resolution.

For the specific study site, CO_2 release from homes is considered insignificant for two reasons. First, the primary power source of air conditioning (both heating and cooling) and cooking is electricity in Phoenix area, thus has no direct CO_2 release; electric space heating is becoming more common in U.S. homes, especially in south states (USEIA 2015). Secondly, heating is occasionally needed in the mild winter in Phoenix due to its warm and semi-arid climate. Figure 2.8 shows the diurnal patterns of the CO_2 release, summing up the modeled traffic emission and respiration from plants, soil, and human. Comparing with the CO_2 fixed by plants, the total release overweighs the total uptake in every month of the year, making the study area a net source of CO_2.

2.2.5 CO_2 Exchange Decomposition

With all the individual sources and sinks quantified above, the modeled total CO_2 flux (Fc_{sim}) is compared to the measurement (Fc_{obs}) by EC tower. The net CO_2 exchange at the study site shows a bimodal shape within the diurnal cycle in both modeling and observation (Figure 2.11), primarily due to the bimodal characteristics of the anthropogenic releases. In addition, the sharp peak in CO_2 assimilation rate in mid-day offsets the soil and plant respiration, where the release curve around the noon is most significantly reduced due to the narrow window of active photosynthesis. This further contributes to the bimodal pattern of variation.

The model error (RMSE) over the study period is 0.21 mg $m^{-2}\,s^{-1}$ (or equivalently 4.68 μmol $m^{-2}\,s^{-1}$), calculated from 18530 half-hour data points. Better performance is observed during warm and hot months from May to October (RMSE = 0.13 mg $m^{-2}\,s^{-1}$ or 2.68 μmol $m^{-2}\,s^{-1}$). The relatively large error in winter and spring (RMSE = 0.25 mg m^{-2} s^{-1} or 5.63 μmol $m^{-2}\,s^{-1}$) may resulted from various reasons. Note that we did not consider any fossil fuel burning other than the traffic release, leading to the underestimation of CO_2 flux from the occasional use of gas for indoor heating during cold months. Other possible sources of urban CO_2 releases not included in the model, such as the outdoor grills or campfires in holiday season, can also contribute to the model discrepancy. The vegetation fraction used in the model is based on the estimation from the change of LAI, which may have more uncertainties in dormant season than in the summer. Lastly, the uncertainties related to CO_2 storage term in EC measurement will influence the model performance (B. Crawford & A. Christen 2014) as the diurnal trend showed in Figure 2.11 has the large variance in observation. Nevertheless, the overall performance is statistically better than the recently developed urban CO_2 model by M. Grote et al. (2016), in which the model RMSE is 15.3 μmol $m^{-2}s^{-1}$.

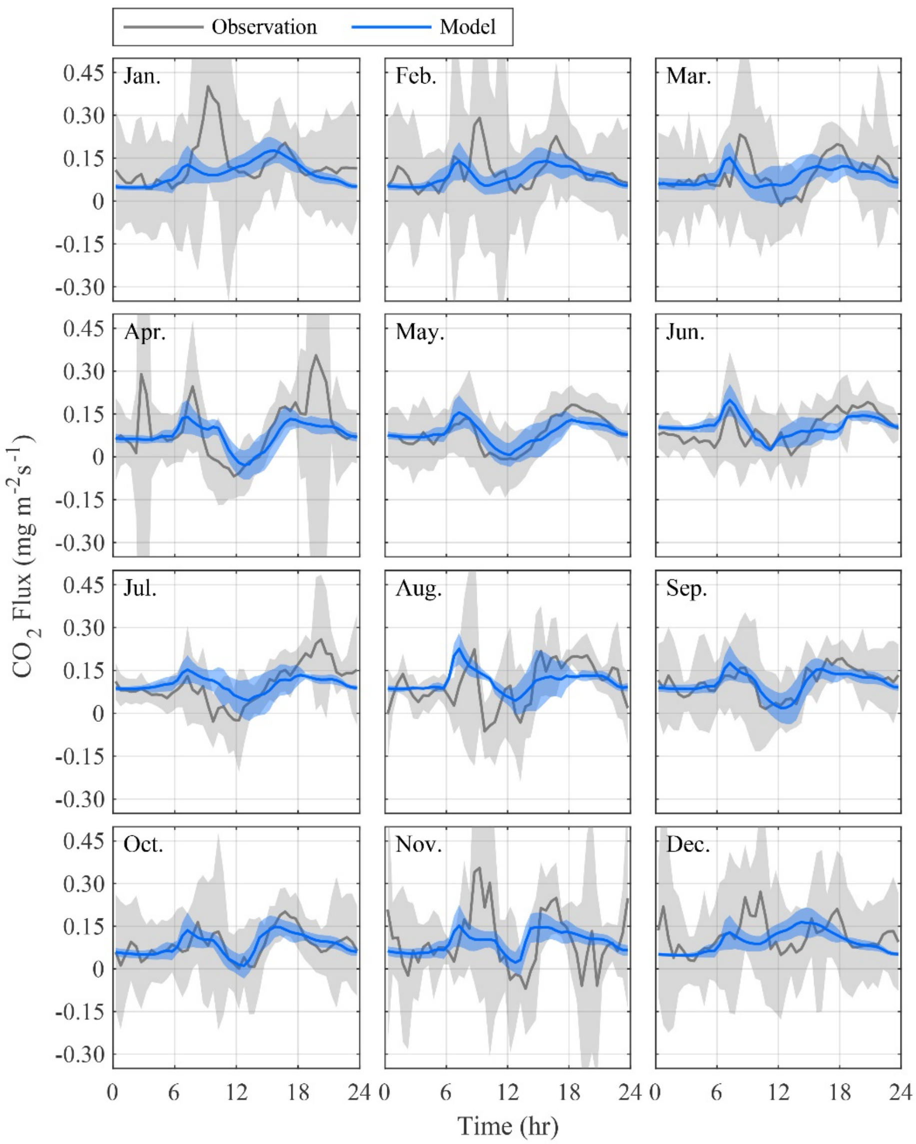

Figure 2.11 Diurnal variation of measured (black) and modeled (blue) CO_2 flux at the study site. The shaded area shows one standard deviation (±1.0σ) from the observed or modeled monthly means.

The overall decomposition of modeled CO_2 fluxes is shown in Figure 2.9. The largest contributor to annual emission is traffic release (40.2%), followed by soil respiration (27.0%). Respiration over vegetated surface and human respiration accounts for 20.4% and 12.3% of annual emission, respectively (Figure 2.9). The composition of CO_2 flux displayed a moderate seasonal variation. During May and June, soil respiration slightly outweighed traffic emission because the rising temperature and ample solar radiation provide the optimum condition for soil respiration. Plants function actively during the growing season, which greatly reduce the net CO_2 efflux over the urban canopy despite of the minor vegetation fraction in the study area. It is noteworthy that 30.0% of the anthropogenic release can be offset by plant net photosynthesis on the annual basis. Nevertheless, in this specific case, the residential area is a net source of CO_2, the decomposition implies a possible carbon balance ("net zero" carbon) of the built environment if adequate area of bare soil is vegetated.

2.3 Concluding Remarks

In this study, we developed a modeling framework to resolve the CO_2 exchange in cities and evaluated its performance in a typical residential area in Phoenix, Arizona. The proposed model integrates the available urban land surface schemes, plant physiological model, and spatially gridded emission datasets. The model results are found to be in good agreement with in-situ measurements of CO_2 flux by an EC flux tower. We also decompose the total carbon flux into individual sources of emission and the sink of plant uptake. In particular, we quantified the enhanced CO_2 absorption and release in the study area, owing to the modified in-canyon temperature, elevated CO_2 level, and maintained irrigation schedules in the built environment. Due to the lawn management, respiration from soil releases a significant amount of CO_2 into the surface layer.

Given the paucity of the available observational dataset for urban vegetation, much of the parameter space of the plant physiological functions in the current model was determined empirically from field experiments in agricultural lands. Nevertheless, the proposed model is scalable and versatile in simulating urban carbon exchange at wide spatio-temporal scales, ranging from the sub-urban scale emission driven by local meteorology, to city and regional scale CO_2 simulations when combined with mesoscale models. In offline simulations, the use of gridded dataset is preferred to match the footprints of EC systems with high spatio-temporal resolutions. When coupling with global climate models, the wide coverage of the spatial gridded dataset on urban geometry, vegetation-related metrics, and anthropogenic CO_2 emission provides a high versatility in data acquisition. It is caveated that, however, modeling of urban carbon exchange is hitherto generally subjected to large uncertainties, with their sources inherited from measurement datasets or numerical parameterization schemes, or both. Therefore, future development of urban CO_2 modeling and the improvement of the model predictive skills call for quantitative characterization of model uncertainties and intricate sensitivity analysis. The endeavor on observational measurements, albeit at their infancy, is progressing rapidly and shedding more and more lights to guide the model development and applications in quantifying the urban carbon exchange in the built environment.

CHAPTER 3

ENVIRONMENTAL CO-BENEFITS OF URBAN GREENING FOR MITIGATING HEAT AND CARBON EMISSIONS

In this Chapter, the UCM-CO_2 model described in Chapter 2 is applied to simulate the impact of the change in urban greening actions, i.e. lawn expansion and degradation, tree plantation, and irrigation, on the thermal and carbon environment in a typical residential neighborhood. We conduct a series of numerical experiments aiming to identify whether the urban greening led to the mitigation effect on both heat and carbon emissions and which action is the most efficient in improving the overall environmental quality.

3.1 Methods

3.1.1 The Study Area

In this study, we use the field measurements by an EC system located in west Phoenix, Arizona, USA (33.483847°N, 112.142609°W) to setup the base scenario as well as for the model calibration. The source area of the flux tower covers a typical residential area of single-family houses. The average roof height is 4.5 m, with a mean aspect (building-height-to-road-width, or *H*/*W*) ratio. Most lots in the study area have small front and backyard spaces with xeric landscaping and irrigated with garden hoses or automated irrigation system. The overall land cover within 1 km^2 of the EC tower were 48.4% impervious surfaces (26.4% building and 22.0% road), 36.8% bare soil, 14.6% vegetation (10.1% grassland and 4.5% tree), and 0.1% water pool (W.T.L. Chow et al. 2014). The dominant vegetation species is Bermuda grass (a warm season C_4 grass), while the common tree species are listed in W.T.L. Chow and A.J. Brazel (2012).

At the study site, the 23-m EC tower recorded four-components radiative fluxes, 3D wind field, air temperature, humidity, CO_2 flux and concentration, and pressure at 10 Hz frequency since 2011. The high frequency atmospheric measurements were then processed, quality-controlled, and integrated at 30 min intervals with no gap filling. To ensure sufficient mixing of CO_2 efflux, data points with the friction velocity u^* smaller than 0.1 m/s were removed from the observation. For numerical simulations, we used the measurements recorded from May 1 2012 to May 31 2012 (31 days).

3.1.2 The UCM-CO_2 Model

As detailed in Chapter 2, the UCM-CO_2 model integrates the urban thermal and hydrological processes using a single-layer UCM with the carbon exchange in the built environment (P. Li & Z.-H. Wang 2020a; 2021b). The geometry of the built environment is represented in the UCM as a two-dimensional (2D) street canyon, consisting of two arrays of buildings separated by a road, with infinite longitudinal dimension. Inside the street canyon, the heterogeneity of the ground facet is represented using sub-facets of paved surfaces (road), bare soil, and vegetated areas (lawns and trees). Furthermore, the morphological representation of urban trees in the UCM is made configurable to accommodate flexible location and number of rows of trees. The model resolves explicitly the radiative heat exchange between shade trees and built facets (Z.-H. Wang 2014) and transpiration by tall vegetation, in addition to the ground level vegetation (lawns).

In addition, the new model is capable of resolving a holistic set of urban CO_2 uptake and emission arising from various sources, including human, building, and vehicular $AnCO_2$ emissions, plant biogenic CO_2 fluxes, and abiotic soil respiration, via a data fusion approach. The plant physiological functions parameterized in the UCM-CO_2 model resolves the dynamics of plants CO_2 exchange, including the carbon assimilation and respiration. Moreover, instead of using one set of plant parameters for all types of vegetations, UCM-CO_2 model distinguishes C_3 and C_4 plants to accommodate the simulation of urban lawns in arid/semi-arid area where warm season grassland is a norm in cities (C.J. Still et al. 2003; T.L.E. Trammell et al. 2019). The urban total energy and CO_2 fluxes are computed from the areal means of the sub-facets in the urban canyon.

For subsequent numerical simulations, we first configure the UCM-CO_2 model according to the landscape characteristics covering the source area of the EC flux measurements described in Section 3.1.1. The biogenic CO_2 exchange is captured by physiological functions of both C_3 and C_4 plants detailed in Chapter 1 or P. Li and Z.-H. Wang (2020a). For example, the gross primary production at canopy level is calculated by integrating CO_2 uptake at leaf over the entire leaf surface area, as show in Eqs. (2.7) and (2.8).

The CO_2 releases from anthropogenic sources are derived from the spatial gridded data. We use traffic on-road emission estimates from Vulcan v2.0 (10km, hourly, K.R. Gurney et al. 2009) and ODIAC (1 km, monthly, T. Oda et al. 2018), and further correct the daily traffic pattern using the local traffic count data in a nearby residential area from Arizona Department of Transportation (ADOT). Human respiration is calculated from population density while assuming normal level respiration rate per capita. Traffic release and human respiration from external data source are obtained from independent inventories and evaluated separately. The simulated hourly CO_2 along with the exchanges in each sector have been compared and calibrated against the EC measurement (P. Li & Z.-H. Wang 2020a), and can be readily used by subsequent numerical experiments.

Based on the information of the morphology, land use, and EC measurement from the study site, the model is configured as shown in Table 3.1. It is noteworthy that the soil moisture was measured beneath the tower without irrigation, which did not accurately represent the soil moisture status in the source area of the EC measurements. In the neighboring residential area, the City of Phoenix recommends irrigating lawn at night or early morning every three days during summer and reduce to bi-weekly irrigation in winter (Landscape Watering by Numbers 2017). Since no information of actual soil moisture or irrigation in the study site is available, we derived the irrigation scheme from the municipal guidance of local residential irrigation and calibrated it against the measured latent heat from the EC tower. In this study, we use soil water content multiplier (SWC_x) to represent the overall irrigation scheme, which is defined as the ratio of target soil moisture after irrigation to the monthly mean soil moisture from measurement.

Table 3.1 Summary of the Parameter Space Used in UCM-CO_2 for the Study Site in Phoenix, Arizona.

Site Properties	
Roof level (m)	4.5
Reference height (m)	22.1
Normalized roof height (-)	0.1
Normalized roof width (-)	0.4
Normalized road width (-)	0.6
Thickness of roof (m)	0.3
Thickness of wall (m)	0.2
Roughness length for momentum for roof (m)	0.01
Roughness length for momentum for canyon (m)	0.05
Roughness length for heat for roof (m)	0.001
Roughness length for heat for canyon (m)	0.005
Street canyon orientation (rad)	3/8 π
Latitude (rad)	0.5844
Longitude (rad)	1.9573
Soil Properties	
Saturation hydraulic conductivity (m s^{-1})	3.4 x 10^{-5}
Residual soil water content (m^3m^{-3})	0.08
Saturated soil water content (m^3m^{-3})	0.35
Slope of soil water retention curve, b	4.50
Soil layer thickness (m)	0.15
Surface Properties	
Roof	
Albedo	0.13
Emissivity	0.95
Thermal conductivity (W $K^{-1}m^{-1}$)	0.90
Heat capacity (MJ $K^{-1}m^{-3}$)	1.00
Wall	
Albedo	0.40
Emissivity	0.95
Thermal conductivity (W $K^{-1}m^{-1}$)	0.10
Heat capacity (MJ $K^{-1}m^{-3}$)	1.40
Road (soil, paved, vegetation)	
Fractions	0.37, 0.53, 0.10
Albedo	0.30, 0.25, 0.30
Emissivity	0.95, 0.95, 0.95
Thermal conductivity (W $K^{-1}m^{-1}$)	1.50, 1.80, 1.00
Heat capacity (MJ $K^{-1}m^{-3}$)	1.80, 1.80, 1.70
Tree	
Coverage	0.05
Normalized tree height (-)	0.80
Normalized tree location (-)	0.10
LAI (m^2 m^{-2})	4.5

3.2 Results and Discussion

3.2.1 Model Validation

The UMC-CO_2 model was first calibrated and evaluated against the EC measurements from May 1st 2012 to May 31st 2012. The results of comparison of the net radiation (R_n), sensible heat (H), latent heat (LE), and total carbon flux (F_c) are shown in Figure 3.1a and 3.1b. The model performance on R_n, H, and LE predictions is comparable to those reported in previous UCM studies (e.g. C.S.B. Grimmond et al. 2011; N. Meili et al. 2020). As for the performance of CO_2 modeling against EC measurement, there is a paucity of reported results in the literature. For example, M. Goret et al. (2019) combined UCM and on-site campaign data to model F_c at a city core and reported a root-mean square error (RMSE) of 0.67 mg $m^{-2}s^{-1}$ between model simulations and field measurements. The Surface Urban Energy and Water Balance Scheme (SUEWS) proposed in L. Järvi et al. (2019) has the RMSE between 0.02 and 0.25 mg $m^{-2}s^{-1}$ when evaluating the diurnal pattern of F_c in different seasons. In comparison, the RMSE of CO_2 flux predicted by the UCM-CO_2 model is 0.04 mg $m^{-2}s^{-1}$ for the mean diurnal cycle (Figure 3.1b).

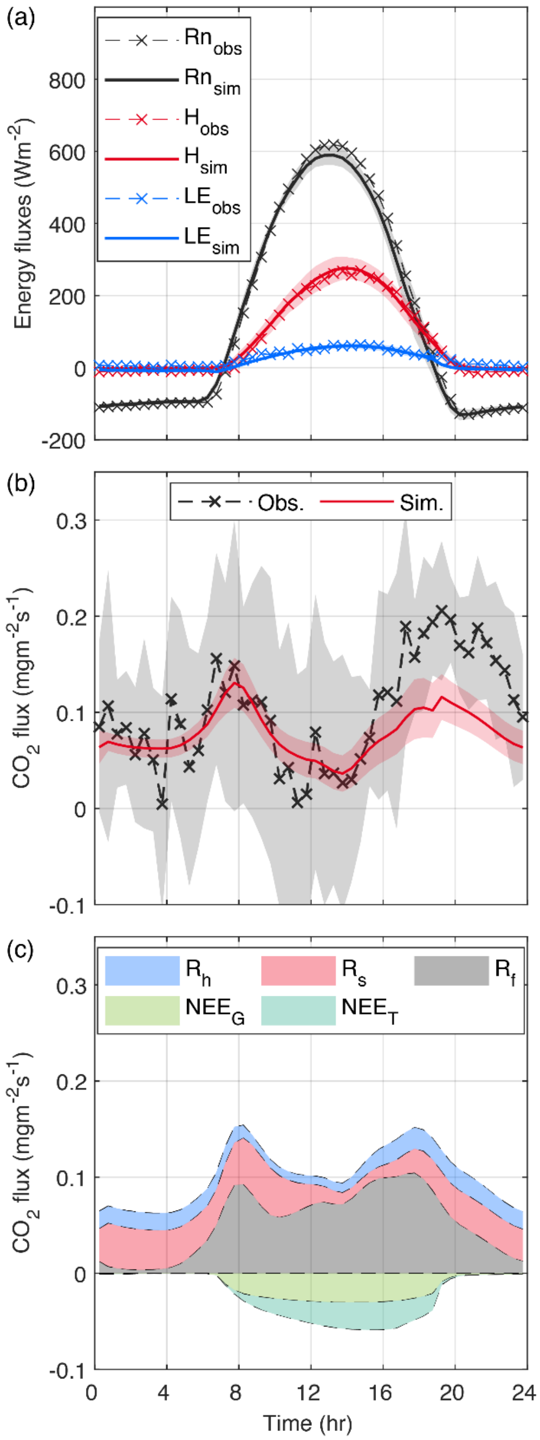

Figure 3.1 Comparison of model results with field measurements by the EC tower: (a) Surface energy fluxes; (b) total CO_2 flux. Shades represent one standard deviation from the model and observation mean. (c) Decomposition of total CO_2 flux from UCM-CO_2

model. R_h, R_s, and R_f represent respiration from human activity, soil, fossil fuel combustion, respectively. NEE_G and NEE_T represent NEE from urban lawn and tree, respectively.

The total CO_2 flux at the study site is the composition of CO_2 release from fossil fuel burning, human respiration, soil respiration, and NEE from urban tree and lawns. At the study site, traffic release is the major contributor to CO_2 efflux, followed by soil respiration due to the large bare soil fraction (Figure 3.1c). Soil respiration rate is validated using the observation data reported in B. Koerner and J. Klopatek (2002) at Phoenix residential area. Human respiration typically contributes 10% of total CO_2 efflux with limited uncertainty caused by population change of the study area (Figure 3.1c). Direct validation of plant NEE is technically difficult due to the lack of useable observational data at the study site. With the validation of total CO_2 flux and other major sources, plant NEE is validated indirectly by the residual of the CO_2 budget. The current study is focused on the biogenic CO_2 exchange, i.e., the variation of CO_2 exchange caused by urban greening.

3.2.2 Results of Case Study

For the subsequent case study to explore the impact of urban greening on urban cooling and biogenic CO_2 exchange, we keep the parameter space of the UCM-CO_2 model described in Section 3.2.1 (Table 3.1) intact, except four parameters viz. the ground vegetation fraction (f_V), tree crown coverage (f_T), bare soil fraction (f_S), and irrigation schedule (SWC_x). The variation of these four parameters corresponds to the changes in four components of urban greening, viz. (1) lawns, (2) urban trees, (3) bare soil, and (4) soil moisture statues reflective of urban irrigation.

The change of tree coverage is achieved by adjusting the crown size of the tree, ramping from 5 to 25% of the road width. The irrigation is scheduled at midnight, with SWC_x changing from 0.9 to 3.5, which is equivalent to 3% and 87% in normalized saturation degree, respectively. Since the ET arising from bare soil and grassland in the semi-arid environment is highly nonlinear with respect to the soil moisture state (Li and Wang 2019), the irrigation schedule supports the plant to meet 28% to 100% of the evaporation demand in the field. Figure 3.2 shows the relations between SWC_x, normalized saturation degree, and evaporation reduction factor.

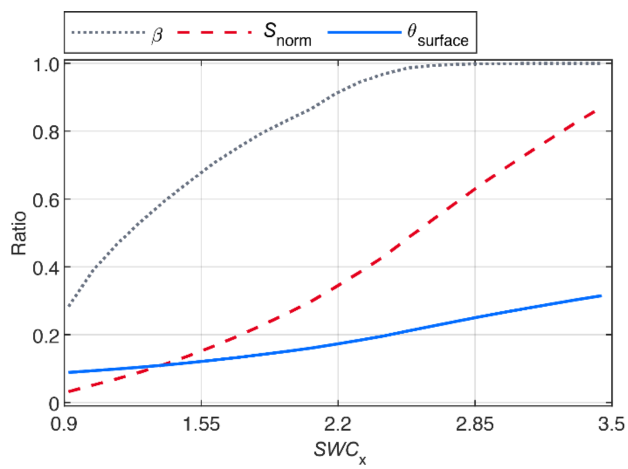

Figure 3.2 Relation between SWC_x to evaporation reduction factor (β, black dot line), normalized saturation degree (S_{norm}, red dash line), and surface soil moisture ($\theta_{Surface}$, blue solid line). β is defined as the actual ET rate to the potential ET. S_{norm} = (surface soil moisture – wilting point) / (field capacity – wilting point). In this case, the field capacity and wilting point are 0.35 and 0.08, respectively.

3.2.2.1 Average Heat and Carbon Mitigation by Urban Greening

We first assess the impact of urban greening on the mean air temperature and mean net biogenic ecosystem exchange (NEE) in the street canyon, viz. T_{can} and $\mathrm{NEE}_{\mathrm{can}}$, averaged over the entire simulation period; the results are shown in Figure 3.3. By changing the fraction of urban green space, the increase of tree coverage leads to much more effective cooling of canyon air temperature than the increase of lawn coverage (colormap in Figure 3.3a). This is consistent to the result reported in an earlier study and can be attributed to the radiative shading by the 3D urban trees being more effective than evapotranspirative cooling by the 2D (planar) lawn (Z.-H. Wang et al. 2016). C.D. Ziter et al. (2019) also found the substantial temperature decrease when tree coverage is greater than 40%. As for the net carbon exchange inside the street canyon, we found that the urban green space, both trees and lawns, function as a net CO_2 sink even with the minimum coverage of f_V and f_T (5%) (contour in Figure 3.3a). In general, the magnitude of $\mathrm{NEE}_{\mathrm{can}}$ (with negative sign denoting carbon sink) further decreases with the urban tree and lawn fractions roughly linearly, signaling that the strength of urban green space as carbon sink increases. It is noteworthy that when f_T is large (> 0.15), the rate of $\mathrm{NEE}_{\mathrm{can}}$ change with lawn fraction decays, indicating that lawns become weaker carbon sink in the presence of dense tree coverage. This can be physically interpreted as those tall/dense urban trees cast larger shaded areas on the ground and suppress the CO_2 uptake strength of the ground vegetation, by intercepting radiation (especially PAR) and lowering the canyon air temperature.

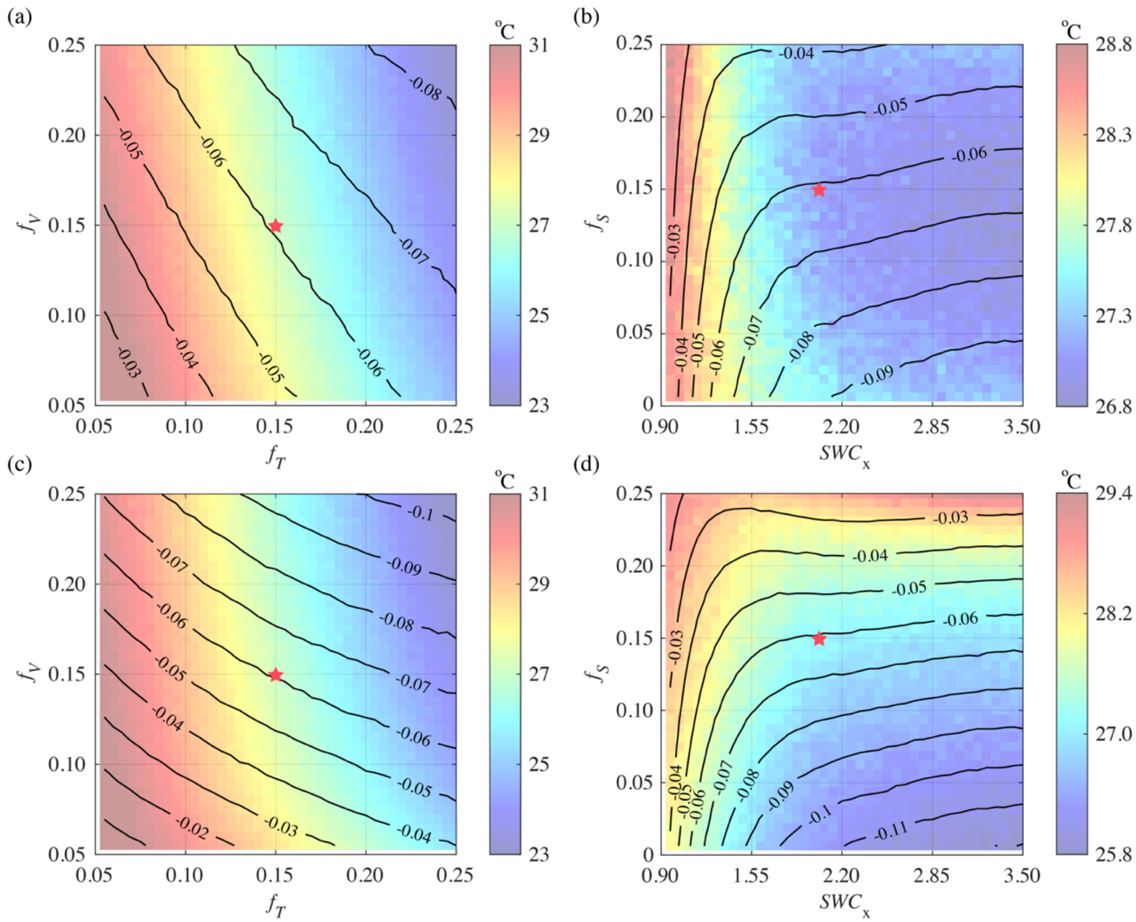

Figure 3.3 Simulation results of the mean canyon air temperature (T_{can} in °C, filled colormap) and net biogenic CO_2 exchange (NEE_{can} in mg $m^{-2}s^{-1}$, contours) by changing (a) Tree coverage, f_T and grassland fraction, f_V, and (b) bare soil fraction, f_S and irrigation schedule, SWC_x, independently. Subplots (c) and (d) are the same as (a) and (b) but keeping the total fraction of $f_V + f_S$ as constant of 0.3. The star indicates the reference scenario with $f_V = 0.15$, $f_T = 0.15$, $f_S = 0.15$, $SWC_x = 2.0$.

As shown in Figure 3.3b, the change in bare soil fraction (f_S) has marginal cooling effect. In contrast, the cooling efficiency from irrigation is significant, especially for cities in hot and dry climate (A.J. Crawford et al. 2012; C. Wang et al. 2019b). The impact of irrigation on carbon exchange, on the other hand, is highly nonlinear. Two distinct regions can be identified in Figure 3.3b: the contour lines are steep at the low soil moisture regime ($SWC_x < 1.3$) but plateaued when amply irrigated, indicating the sharp change of sensitivity of carbon uptake to irrigation. As approaching the limiting case where irrigation is turned off, the high water stress suppresses the carbon uptake from plants, leaving bare soil respiration the primary source of CO_2 exchange. The rate of soil respiration is positively correlated with a wide range of soil temperature (J. Lloyd & J.A. Taylor 1994). When urban plants are irrigated, it clearly provides the co-benefit of cooling the ambient air temperature (Figure 3.3a), and meanwhile reducing the CO_2 emission by (1) reducing soil respiration via cooling effect and (2) promoting plant carbon absorption via reducing the water stress. When adequately irrigated ($SWC_x > 2.0$), the CO_2 uptake becomes insensitive to further increase in irrigation amount, and the net carbon flux is in turn dominated by the change of bare soil fraction (c.f. flat contour lines in Figure 3.3b).

For results shown in Figure 3.3a and 3.3b, we keep the land cover changing independently, meaning that the increase of f_S and f_V leads to the decrease of total impervious surface area (ISA). In practical urban planning, however, the ISA is unlikely to change, at least significantly, in a developed built environment. To capture the more realistic urban greening strategies, we then devise an alternative set of scenarios by fixing the total fraction of urban greening at 30% (i.e. $f_S + f_V = 0.3$). The changes of lawn and bare soil fractions are therefore dependent and limited to the availability of open ground space in the street canyon. Urban greening at the road level physically represents the conversion of bare soil into vegetated surface, or reversely as the degradation of urban lawns. The simulation results of the effect of this new (and more realistic) set of urban greening scenarios on urban cooling and carbon mitigation are shown in Figure 3.3c&d, and can be seen as qualitatively consistent with the results of their counterpart scenarios in Figure 3.3a&b. Nevertheless, some differences are noted: first, the increase of f_V in Figure 3.3c leads to faster carbon mitigation rate by increasing vegetation cover than that in Figure 3.3a. This is due to that urban greening, by converting bare soil to vegetated (with a constant availability of open space in the street canyon), is doubly beneficial by providing additional CO_2 uptake capability as well as evaporative cooling (F. Aram et al. 2019; J. Song & Z.-H. Wang 2015), both contributing to CO_2 reduction. Similar trend of strengthened carbon mitigation capacity can be found, by comparing Figure 3.3d and 3.3b, via enhanced irrigation of urban lawns.

It is noteworthy that from reported observation dataset, soil respiration from vegetated area is higher than that arising from purely bare soils, primarily because of active root respiration and high soil organic carbon from the grassland (J. Bae & Y. Ryu 2017; B.J.L. Ng et al. 2015; X. Tao et al. 2016). Nevertheless, well-maintained urban lawns act net CO_2 sinks, despite that the elevated soil respiration rate weakens the plant carbon uptake. This effect will be further amplified if an urban lawn degrades into brown turf grassland with large bare soil portion due to extreme heat or drought, as the vegetation fraction for active CO_2 uptake shrinks while respiration from underground biomass continues.

Furthermore, the results of predicted sensible and latent heat fluxes aggregated over the street canyon are shown in Figure 3.4. The response of sensible heat to varying components of urban greening is similar to that of the canyon air temperature, and the latent heat to the carbon likewise. It is noteworthy that in Figure 3.4b, the latent heat exhibits a bi-modal pattern with respect to the bare soil fraction in the regime where the soil moisture is high ($SWC_x > 2.2$). This bimodal pattern of latent heat can be attributed to two mechanisms regulating plant transpiration and soil evaporation separately. When the bare soil fraction is low ($f_S < 0.05$), the presence of large impervious surface warms the canyon air (Figure 3.3b), which can, in turn, enhances plant evapotranspiration with ample irrigation. On the other extremity, when the large bare soil fraction is large ($f_S >$ 0.15), urban irrigation leads to large soil evaporation.

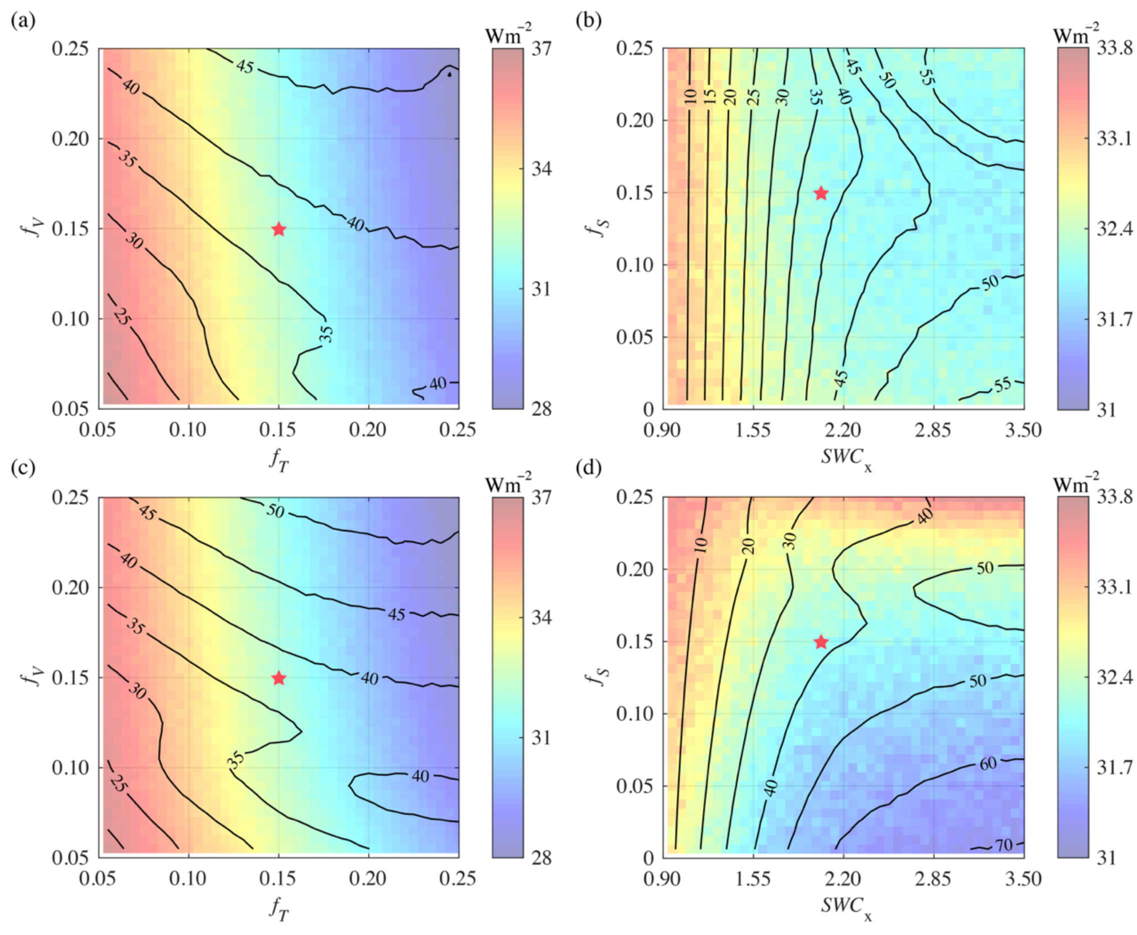

Figure 3.4 Same as Figure 3.3 but for mean canyon sensible heat flux (H_{can}, Wm^{-2}, filled colormap) and latent heat flux (LE_{can}, Wm^{-2}, contours)

3.2.2.2 Diurnal Variation of Changes in Temperature and Carbon Flux

In addition to the mean heat and carbon mitigation, here we look into the diurnal variation of T_{can} and NEE_{can} due to urban greening by presenting the results of a portfolio of selected scenarios listed in Table 3.2, as shown in Figure 3.5. From Figure 3.5a, it can be seen that the increase of ground vegetation fraction can enhance the strength of CO_2 sink, but has insignificant impact on environmental cooling. Furthermore the use of lawns for mitigating carbon emissions is subject to additional constraints: (1) irrigation of urban lawns, or more generally the maintenance of mesic landscaping, in the semi-arid or arid cities can be demanding due to water scarcity (E. Litvak et al. 2017), and (2) lawns are susceptible to degradation from exposure to high thermal and water stresses. In contrast, urban trees provide an attractive means as they provide more significant cooling effect (Figure 3.5b), especially during nighttime (recall that UHI is predominantly a nocturnal effect), owing to the synergistic radiative and evapotranspirative cooling (J. Konarska et al. 2016; R. Upreti et al. 2017; C. Wang et al. 2019a; C. Wang et al. 2018b). Increasing tree fraction also promotes CO_2 sequestration significantly during daytime. The significant carbon sink strength of trees is primarily attributable to greater leaf areas in multiple layers of tree canopy and wide adaptation to heat and water stress (R. Teskey et al. 2015). For cities in arid environment, shade trees (especially native species) are particularly recommendable for better environmental co-benefit of thermal and carbon mitigation and more economic water-heat trade-off.

Table 3.2 Configurations of Urban Greening for the Study Site and Numerical Experimental Scenarios

Scenario	f_V	f_T	f_S	SWC_x
PHX	0.10	0.05	0.37	1.5
Ref	0.15	0.15	0.15	2.0
$Grass^-$	**0.05**	0.15	0.15	2.0
$Grass^+$	**0.25**	0.15	0.15	2.0
$Tree^-$	0.15	**0.05**	0.15	2.0
$Tree^+$	0.15	**0.25**	0.15	2.0
$Soil^-$	0.15	0.15	**0.05**	2.0
$Soil^+$	0.15	0.15	**0.25**	2.0
Irr^-	0.15	0.15	0.15	**1.0**
Irr^+	0.15	0.15	0.15	**3.0**

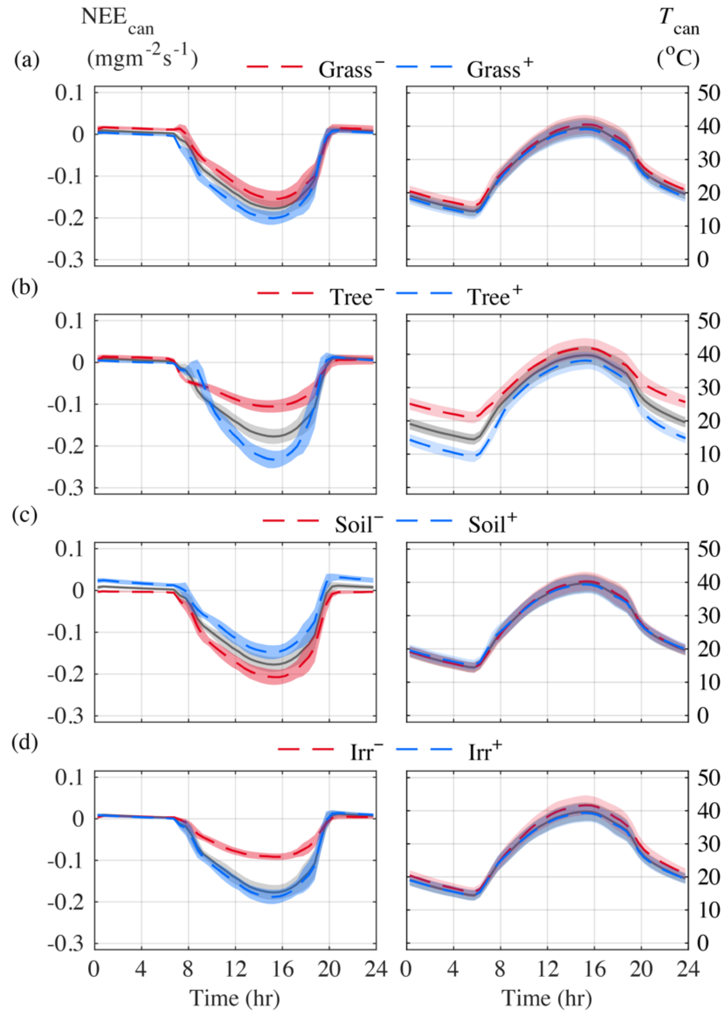

Figure 3.5 Mean diurnal variation of the net biogenic CO_2 exchange NEE$_{can}$ and the canyon temperature T_{can}: (a) Grass$^{\pm}$, (b) Tree$^{\pm}$, (c) Soil$^{\pm}$, and (d) Irr$^{\pm}$. Blue and red lines stand for the "+" and "–" scenarios in each category, respectively (detailed in Table 2). Shaded areas represent one standard deviation. The solid black line indicates the reference scenario with $f_V = 0.15$, $f_T = 0.15$, $f_S = 0.15$, $SWC_x = 2.0$.

As comparing to the reference case, increased irrigation does not intend to significantly reduce T_{can} or NEE$_{can}$. But less irrigation will lead to apparent temperature increase and loss of CO_2 sequestration (Figure 3.5d). The normalized saturation degree

(S_{norm}) for Irr^{-}, Ref, and Irr^{+} cases are about 5%, 30% and 70%, respectively. The asymmetric phenomenon is likely caused by the non-linear relationship of evapotranspiration as a function of soil moisture (ET-θ relation) (P. Li & Z.-H. Wang 2019). When soil moisture becoming the limiting factor for plant growth, evaporative cooling and CO_2 uptake will be largely suppressed. On the contrary, when soil moisture is adequate to support healthy growth for plants, T_{can} becomes insensitive to irrigation, so does NEE_{can}. The diurnal variation echoes the mean effect discussed in the previous section: Adequate irrigation is necessary to effectuate the environmental co-benefit of urban greening for heat and carbon mitigation, whereas excessive soil water only has but marginal effect on further improving the urban environmental quality.

3.3 Environmental Implications

Based on results derived from the designed scenarios, urban greening leads to the general improvement in thermal and carbon environment in cities. Though theoretically, wide coverage of green space and irrigation cool the environment and strengthen natural carbon sinks to a significant degree, cost-benefit trade-offs should be considered in management practices. It is noteworthy that the benefit evaluation should take the value of carbon sinks into account. From this perspective, the cost of irrigation will be offset by the added value it creates in CO_2 emission reduction, as it 1) helps vegetation maintain a healthy status for active CO_2 uptake; 2) mitigates the degradation risk of urban lawns; 3) cools the soil thus suppress soil respiration. Similarly, it is recommended to adopt street trees, instead of lawns, for better heat and CO_2 emission mitigation effects in cities, as tree 1) has denser leaves thus greater CO_2 sink power; 2) cools the environment thus suppress respiration; 3) requires less maintenance. Nonetheless, for some specific regions or tree species, trees might be exposed to other risks such as wildfire (P. Dass et al. 2018) and mortality (D. Hilbert et al. 2018; I.A. Smith et al. 2019).

Quantitatively, the interplays between thermal and carbon environment need to be disentangled using advanced numerical models. For example, both temperature and moisture control the microbial activity in the soil, thus irrigation amount determines whether co-benefits or advisory effects happen in practice. Though irrigation cools the soil, extra soil moisture might promote soil respiration. Meanwhile, insufficient irrigation affects the growth of vegetation and limits the photosynthesis rate. Best environmental co-benefits will be achieved when the fine balance between these mechanisms is found. The critical thresholds will vary from different cities, local tree species, and management practices. For cities in arid climate regions where urban thermal stress and water scarcity co-exist, results from precise modeling might refresh the perspectives on cost-benefit trade-offs, therefore unveil more feasible strategies to a low carbon city. Urban planners and city designers should also adopt the modeling tools from urban climate research communities in decision-making progresses.

3.4 Concluding Remarks

In this study, we utilized the newly developed UCM-CO_2 model to quantify the relative contribution arising from specific components of urban greening, viz. grassland, tree, soil, and irrigation, to the total environmental co-benefit for improving both thermal and air quality. It should be caveated that parameterizations of urban heat and carbon exchange processes in the UCM-CO_2 model and the results of simulation are constrained by the limited availability of observational datasets and the difficulty of controlling urban variables in real urban planning. Nevertheless, the results of numerical experiments are informative as to reveal the mean and diurnal pattern of variations of air temperature and NEE in the street canyon with changes of individual urban greening component. The interactions between the dynamics of heat and CO_2 exchange were also manifest, where the relative coverage of lawns, shade trees, and bare soils plays a dominant role.

More specifically, for different urban landscaping strategies, we found that tall shades trees have the highest efficacy for achieving the desired environmental co-benefit. In contrast, the effect of mesic landscape using urban lawns is conditioned on the adequate water supply and good maintenance practices to prevent degradation, whereas xeriscaping has limited capacity for reducing carbon emissions despite its water-saving potential. In addition, we identified the nonlinear transition in the response of ambient temperature and total carbon flux, and the bi-modal variability of the latent heat, to different irrigation schemes. The finding of these intriguing patterns has the potential to help urban planners and practitioners to optimize urban irrigation strategies in terms of the water-energy trade-off. These findings, along with its implications on urban planning and management, improve our holistic understanding of urban environmental quality and help the endeavor to the sustainable urban development.

CHAPTER 4

MULTI-OBJECTIVE OPTIMIZATION OF URBAN ENVIRONMENTAL SYSTEM DESIGN USING MACHINE LEARNING

In this Chapter, a machine learning (ML) algorithm, Gaussian Process regression is used to emulate the physical-based UCM-CO_2 model to assess the daily mean in-canyon temperature and net ecosystem exchange. ML surrogates are trained and validated on the simulation results generated by UCM-CO_2 over a wide range of urban characteristics, showing high accuracy in capturing heat and carbon emissions. Using the validated surrogate models, we then conduct multi-objective optimization using the genetic algorithm to optimize urban design scenarios for desirable urban mitigation effects.

4.1 Method

4.1.1 Single Layer Urban Canopy Model

In this study, we adopt the newest version of Arizona State University Urban Canopy Model (ASLUM version 4.1, P. Li & Z.-H. Wang 2020a; 2021b). ASLUM v4.1 features the coupling of urban energy and water dynamics with photosynthesis and respiration from urban vegetation, which enables us to quantify the compound environmental impact of urban mitigation strategies, urban greening in particular, for both urban heat and CO_2 mitigation.

To characterize the urban environment, the in-canyon air temperature (T_{can}) is calculated from the energy balance closure in street canyon (i.e., building walls and grounds) by (Wang et al., 2013),

$$T_{\mathrm{can}} = \frac{\frac{2H}{W}\frac{T_w}{RES_w} + \frac{f_p T_p}{RES_p} + \frac{f_v T_v}{RES_v} + \frac{f_s T_s}{RES_s} + \frac{T_a}{RES_{can}}}{\frac{2H}{W}\frac{1}{RES_w} + \frac{f_p}{RES_p} + \frac{f_v}{RES_v} + \frac{f_s}{RES_s} + \frac{1}{RES_{can}}}, \tag{4.1}$$

where T and f represent the temperature and fraction of the sub-facets; RES is the aerodynamic resistance on each sub-facets; subscripts w, p, v, s, a, can denote walls, paved surfaces, vegetation, bare soil, atmosphere, and canyon respectively. In addition, the biogenic net ecosystem exchange (NEE) is given as

$$\mathrm{NEE} = R - \mathrm{GPP}, \tag{4.2}$$

where R is the total respiration from soil and vegetation; GPP is the total gross primary production from trees and lawns. The value of NEE follows the convention in ecology with both R and GPP positive numbers, and negative NEE means net carbon sink.

4.1.2 Dataset

A simulated dataset generated by ASLUM v4.1 are used for the subsequent ML emulations. To improve the robustness of ML models over a wide range of urban configurations, we conduct a large number of numerical simulations (N = 55388) by ASLUM v4.1 using a variety of critical system design parameters. Training ML models only requires a small portion of the dataset, while the majority of the dataset will be used in model testing and evaluation (see Section 4.2.1). Each simulation is driven by in-situ observation from an eddy covariance (EC) system in west Phoenix, Arizona (33.483847ºN,112.142609ºW) as the meteorological forcing. The EC system measured basic meteorological variables and energy fluxes at 22 m above the ground (>15 m above average roof level). Data retrieved from this EC tower (W.T.L. Chow 2017) has been used in previous urban studies ranging from surface energy dynamics, urban environment modeling, and boundary layer physics (W.T.L. Chow et al. 2014; N. Meili et al. 2020; J. Song et al. 2017). The meteorological forcing used in subsequent simulations includes the downwelling shortwave and longwave radiation, atmospheric temperature, pressure, humidity, and wind speed (Figure 4.1). We selected 24 hours of measurement during a typical clear day in early summer (May 11th, 2012) to drive the physical model, with air temperature of 35 ^{o}C at the maximum and 23 ^{o}C at the minimum. Meanwhile, the time selection of meteorological forcing avoids the influence from random weather events like the presence of cloud, precipitation, and cold/heat waves. During the simulation period, ALSUM v4.1 predicts the evolution of upwelling radiation, surface temperatures and heat fluxes, and biogenic CO_2 at an interval of 5 minutes, and aggerates these variables into to 30-minutes average as the outputs.

The scenarios of urban system design in ASLUM v4.1 are represented by several groups of parameters, including the street morphology, thermodynamic properties of urban fabric, urban greenery properties, overall land use types, and landscaping management schemes. Previous studies have shown that certain parameters of the ASLUM v4.1 possess higher sensitivity especially in prediction of extreme events and design optimization. These parameters are hereafter referred to as the critical design parameters (P. Li & Z.-H. Wang 2021b; J. Yang & Z.-H. Wang 2014; J. Yang et al. 2016). In the light of previous studies, here we select 24 urban system critical design parameters in four groups that are most impactful to the urban thermal environment and carbon exchange dynamics (Table 4.1). In subsequent simulations, values of each critical parameter are stochastically sampled from its prescribed probability density functions

(PDFs). Those PDFs are primarily derived from field or laboratory measurements, reported values from literature, or best estimates within the physical ranges (P. Li & Z.-H. Wang 2021b). In each simulation, we monitor the mean air temperature at the pedestrian level inside of street canyon (T_{can}), and the mean net ecosystem exchange (NEE) over the street canyon. Finally, all simulations are randomly split into two sets (training and test) for the subsequent ML regression and optimization.

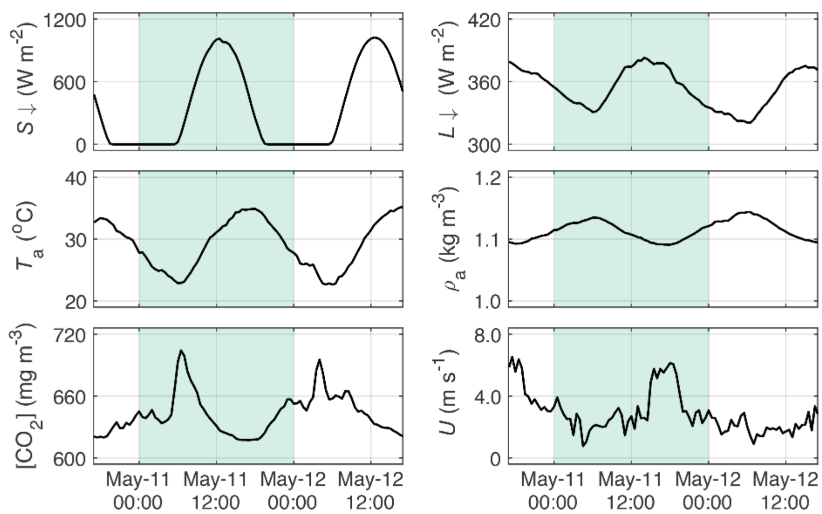

Figure 4.1 Meteorological forcing used in the simulation (a) Downwelling shortwave ($S\downarrow$) and longwave ($L\downarrow$) radiations; (b) air temperature (T_a) and windspeed (U); (c) background CO_2 concentration ([CO_2]) and air density (ρ_a). Mean T_{can} and NEE are calculated during the shaded period (24 hours). Results from non-shaded period are used for quality control in ASLUM and are not used in ML training and test.

Table 4.1 Variables Used as Training Features for Gaussian Process Regression Models.

Name	Unit	Mean	Std.	Min.	Max.
Canyon geometry					
Normalized road width					
W	-	0.60	0.19	0.05	0.80
Normalized building height					
H	-	0.78	0.40	0.10	1.50
Soil properties					
Bare soil fraction					
f_s	-	0.21	0.11	0.05	0.50
Saturation soil moisture					
W_s	-	0.35	0.07	0.15	0.55
Residual soil moisture					
W_r	-	0.06	0.01	0.02	0.10
Initial soil moisture					
SWC_i	-	0.20	0.06	0.08	0.30
Plant properties					
Lawn fraction					
f_v	-	0.33	0.11	0.05	0.50
Tree - Leaf area index					
LAI_T	m^2/m^2	4.15	0.87	1.50	6.50
Grass - Leaf area index					
LAI_G	m^2/m^2	2.68	0.79	1.00	5.00
Tree crown size					
r_T	-	0.07	0.03	0.02	0.12
Tree height					
h_T	-	0.70	0.21	0.25	1.00
Tree location					
c_T	-	0.48	0.27	0.00	1.00

Name	Unit	Mean	Std.	Min.	Max.
Material properties					
Albedo - Wall					
aW_1	-	0.17	0.04	0.06	0.28
Albedo - Paved					
aG_1	-	0.13	0.03	0.05	0.20
Albedo - Lawn					
aG_2	-	0.20	0.04	0.08	0.33
Albedo - Bare soil					
aG_3	-	0.20	0.04	0.08	0.33
Thermal conductivity - Wall					
kW_1	$Wm^{-1}K^{-1}$	0.12	0.03	0.05	0.20
Thermal conductivity - Paved					
kG_1	$Wm^{-1}K^{-1}$	1.49	0.33	0.56	2.44
Thermal conductivity - Lawn					
kG_2	$Wm^{-1}K^{-1}$	0.65	0.14	0.24	1.06
Thermal conductivity - Bare soil					
kG_3	$Wm^{-1}K^{-1}$	0.23	0.05	0.08	0.36
Heat capacity - Wall					
cW_1	$MJm^{-3} K^{-1}$	2.31	0.51	0.86	3.74
Heat capacity - Paved					
cG_1	$MJm^{-3} K^{-1}$	0.90	0.20	0.34	1.46
Heat capacity - Lawn					
cG_2	$MJm^{-3} K^{-1}$	1.70	0.37	0.64	2.76
Heat capacity - Bare soil					
cG_3	$MJm^{-3} K^{-1}$	1.02	0.21	0.38	1.63

4.1.3 Gaussian Process Regression

GPR is a Bayesian kernel regression method that uses a Gaussian Process (GP) to describe the distribution of the quantity of interest and the Bayes' theorem to infer the posterior distribution (C.E. Rasmussen & C.K.I. Williams 2006). A GP refers to a set of random variables, $\{Y_1, Y_2, ..., Y_k\}$ (often indexed by inputs), that jointly follow a multivariate Gaussian distribution. GPR starts by specifying the prior (i.e., before seeing any data) mean and covariance of the joint Gaussian distribution using the mean function $\mu(\mathbf{x}) = E[Y(\mathbf{x})]$ and a covariance function $k(\mathbf{x}, \mathbf{x}') = E[[Y(\mathbf{x}) - \mu(\mathbf{x})][Y(\mathbf{x}') - \mu(\mathbf{x}')]]$, respectively. Here, $\mathbf{x}$ is a d-dimensional vector and may include space coordinates, time, or controlling variables of Y. The mean and covariance functions should reflect the prior knowledge of the general trend and level of smoothness of the target function, respectively. The covariance implicitly maps the inputs to features $\phi(\mathbf{x})$. By doing so, GPR can approximate complex, nonlinear relationships between the target ($Y = T_{\mathrm{can}}$ or NEE) and inputs (sampled from the ASLUM v4.1 parameter space).

Once training data are introduced, GPR uses the Bayes' Theorem to infer the posterior distribution of the target. Let $D = \{(\mathbf{x}_1, y_1), (\mathbf{x}_2, y_2), ..., (\mathbf{x}_n, y_n)\}$ denote training data, the posterior distribution of the target variable at an unseen data point, $Y^* = Y(\mathbf{x}^*)$ is given by:

$$Y^* \mid D, \mathbf{x}^* \sim N(\bar{y}^*, Var(Y^*)). \tag{4.3}$$

The posterior mean and variance are given below:

$$\bar{y}^* = \mu(\mathbf{x}^*) + \Sigma^{*T}(\Sigma + \sigma_\varepsilon^2 I_n)^{-1}[\mathbf{y} - \mu(\mathbf{x})], \tag{4.4}$$

$$Var(Y^*) = \sigma_0^2 - \Sigma^{*T}(\Sigma + \sigma_\varepsilon^2 I_n)^{-1}\Sigma^* . \quad (4.5)$$

In the above equations, $\mathbf{y} = \{y_1, y_2, ..., y_n\}$, σ_ε^2 is noise variance, σ_0^2 is signal variance, a hyperparameter of the covariance function, Σ denotes the prior covariance matrix of the training data with its *ij*-th entry as $\Sigma_{i,j} = k(\mathbf{x}_i, \mathbf{x}_j)$, and Σ^* is a vector denoting the covariance between training and test data, i.e., $\Sigma_i = k(\mathbf{x}_i, \mathbf{x}^*)$.

In this study, we use GPR to construct surrogate models for NEE and T_{can}, respectively. Both surrogate models use the critical design parameters of the ASLUM as input variables after scaling to [0, 1]. We note that this is a high dimensional problem with 24 input variables (p=24), which would pose challenges for some commonly used surrogate modeling techniques such as polynomial chaos expansion (W. He et al. 2020). For both surrogate models, we specify a linear prior mean and the commonly used squared exponential covariance function. The models are trained using simulation results of ASLUM v4.1 described in Section 4.1.2. The two hyperparameters of the covariance function (signal variance and range) are tuned by maximizing log likelihood; the other hyperparameters (noise variance and coefficients of the linear mean function) are estimated once the best signal variance and range are determined. The model trained using the selected hyperparameters is then used for optimization (Section 4.1.4). In this study, we use the posterior mean $\bar{y}^*$ to emulate temporally aggregated NEE and T_{can} simulated by ALSUM. However, whenever needed it is possible to use the posterior variance with stochastic/robust optimization techniques (e.g., U.M. Diwekar 2003; A.A. Mishra et al. 2020).

Besides GPR, we also use the radial basis function (RBF) interpolation technique (D.B. McDonald et al. 2007) to construct the surrogates. RBF interpolation constructs an exact emulator; in other words, the fitted function is exactly equal to the target variable at training data points. Because of this appealing feature and satisfactory performance of RBF in previous studies (T. Akhtar & C.A. Shoemaker 2016), we include RFB interpolation in this study to construct surrogates for T_{can} and NEE, respectively. The Gaussian basis is used, and its decay rate hyperparameter was selected by maximizing coefficient of determination on a validation set separate from training data.

4.1.4 Metrics of Environmental Quality and Multi-objective Optimization

As mentioned, we use daily mean in-canyon temperature (T_{can}) and biogenic NEE to represent thermal and carbon environment in this study. During summertime, both lower T_{can} and NEE are preferred for better heat mitigation and CO_2 reduction purposes. It is noteworthy that urban mitigation strategies will affect the behavior of CO_2 exchange over vegetated surfaces, primarily by affecting the atmospheric temperature and radiation redistribution. Specifically, the shading effect of tall urban trees (R. Upreti et al. 2017; Z.-H. Wang 2014) reduces photosynthetic active radiation on understory lawns, lowering CO_2 uptake rate. Meanwhile, the cooling effect caused by shading and evapotranspiration from green spaces reduces enzyme activities in photosynthesis and respiration processes, weakening CO_2 uptake and release at the same time. The complex interactions between heat and biogenic carbon dynamics make it difficult to disentangle the effect of mitigating heat and CO_2 emissions separately.

To account for the compound mitigation effect to heat and carbon emissions, we perform multi-objective optimization to minimize T_{can} and NEE simultaneously. The decision variables (24 ASLUM v4.1 parameters) are constrained by their physically feasible ranges (Table 4.1). The optimization problem is solved by an elitist genetic algorithm (K. Deb 2001) in MatLab®. A population size of 500 is used in each generation with the maximum of 500 generations when searching for the Pareto solutions. Mathematically, Pareto solutions are defined as a compromise to "no other solution that can improve at least one of the objectives without degradation any other objective" (P. Ngatchou et al. 2005). The optimization process stops when the movement of the points on the Pareto front between the final two iterations is small.

To facilitate the assessment of optimization results and to enable direct comparison among designed scenarios, we introduce a compound heat-carbon index (CHCI):

$$\mathrm{CHCI} = \alpha \overline{T_{\mathrm{can}}} + \left(1-\alpha\right)\overline{\mathrm{NEE}}, \tag{4.6}$$

where $0 < \alpha < 1$ is the weight of multiple environmental indicators (for simplicity, we use $\alpha = 0.5$ for subsequent analysis), and the overhead bar denotes the normalization by

$$\overline{X} = \frac{X - X_{\min}}{X_{\max} - X_{\min}}, \tag{4.7}$$

with X being T_{can} or NEE. Qualitatively, lower CHCI represents lower temperature and stronger carbon sink, thus indicates better overall environmental quality.

4.2 Results and Discussion

4.2.1 Machine Learning Surrogates

In this study, we train two GPR models to emulate T_{can} and NEE, respectively, using 5% of the simulated dataset ($N_{train} = 0.05N = 2769$), as described in Section 4.1.2. We then evaluate the emulation accuracy of the two surrogates on the test data ($N_{test} = 0.95N = 52619$). Figure 4.2a&b shows the comparison between T_{can} and NEE simulated by the physical model ASLUM v4.1 and ML surrogates on the test data. For each scenario, CHCI is calculated by Eq.(4.6) using normalized T_{can} and NEE from ASLUM and GPR models respectively (Figure 4.2c). The result shows GPR models reproduce the environmental metrics with satisfactory accuracy, with coefficient of determination (R^2) above 0.96 for T_{can}, NEE, and CHCI. Figure 4.2d shows the change of R^2 and normalized root mean square errors ($RMSE_n$) of the comparisons when varying the training sample size from 0.5% to 10% with 0.5% increment ($0.005N = 277$). R^2 and $RMSE_n$ shown in Figure 5.3d are the ensemble means from 20 runs with different random seeds to reduce the influence of data heterogeneity and randomness in training sample selection. The variations among 20 runs are insignificant with the coefficient of variance (standard deviation / mean) smaller than 0.002 for R^2 and 0.02 for $RMSE_n$. Generally, the model performance improves with the increase of training sample size, but the change becomes marginal when sample size is greater than 3% ($0.03N = 1662$). The GPR surrogate models retain reasonable accuracy ($R^2 > 0.90$ for T_{can} and NEE on test data) when trained by only 0.5% (277) of the dataset while tested on the rest. Small training sample size can potentially cause over-fitting, especially for models fitting on a large number of input features due to the "curse of dimensionality" (M.A. Bessa et al. 2017). In this study, the minimum training sample size required to avoid over-fitting issue is around 0.3% ($0.003N = 166$), but the model performance and stability degrade significantly on test samples when training sample size is smaller than 0.5% of the dataset. Users with a limited amount of data points from observations should be cautious about the over-fitting issue and employ strategies such as reducing the input dimension and model averaging (G.C. Cawley & N.L.C. Talbot 2007; 2010). To the extent allowed by computational budget, we suggest increasing training sample size to ensure better and more robust model performance.

The emulation accuracy of RBF interpolant is substantially lower than GPR ($R^2 =$ 0.77 and 0.88 for T_{can} and NEE, respectively, evaluated on test data). Therefore, we did not use the RBF surrogates for optimization. A possible cause of the inferior performance is that RBF may be subject to numerical stability and robustness issues with large datasets (V. Skala 2017). However, RBF may be an attractive candidate for surrogate modeling when only a small amount of training data is available (T. Akhtar & C.A. Shoemaker 2016; S. Razavi et al. 2012).

In addition to the satisfactory accuracy, our performance benchmark shows that the GPR surrogate models only take 3.6, 17.6, and 35.0 seconds to simulate a group of 10, 50, and 100 different scenarios respectively, which is eight times faster on average than ASLUM v4.1 (tested on Intel Xeon E-2186G 3.8GHz with 12 logic cores and 40GB RAM). The high efficiency reduces the time cost of calculation, facilitating decision making processes and enabling fast comparison between a large amount of scenarios, especially when exhaustive search for best case is desired. The improvement in calculation efficiency also promotes fast assessment of variable sensitivity for high-dimensional physical-based ASLUM v4.1, in comparison with the previous sensitivity analysis (P. Li & Z.-H. Wang 2021b).

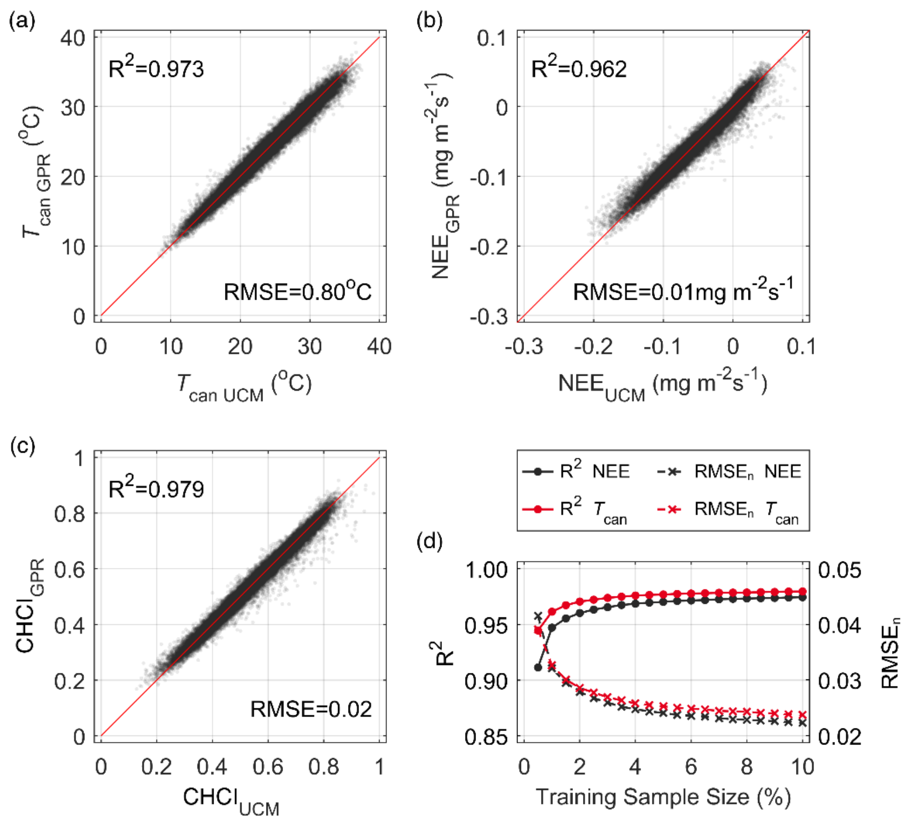

Figure 4.2 Performance of ML training and tests using the GPR surrogate for (a) T_{can}, (b) NEE, (c) CHCI when trained using 5% of the simulated dataset, and (d) the ensemble mean of R^2 and normalized RMSE ($RMSE_n$) of T_{can} and NEE when trained using different training sample sizes. For each sample size, model performance is evaluated as the average of 20 replicate runs.

4.2.2 Multi-objective Optimization

Once the GPR emulations of ASLUM v4.1 is trained and tested, we use a multi-objective genetic algorithm (GA) optimization process to find the desirable urban system design within the physically feasible range of the critical design parameters in Table 4.1. The multi-objective GA finds urban configurations that minimize T_{can} and NEE simultaneously, leading to Pareto solutions. The Pareto solutions characterize the trade-off among multiple objectives in a constrained optimization. In this study, a tradeoff exists between the two urban environmental measures, viz., T_{can} and NEE, because photosynthesis shrinks with temperature decrease, though the underlying mechanisms are much more complex. Figure 4.3 shows the comparison of results of ASLUM v4.1 simulations and the Pareto front formed by multiple Pareto solutions (n = 134) identified by GA with similar CHCI but different combinations of T_{can} and NEE. The Pareto solutions are located lower left corner, within the range of CHCI from −0.05 to 0.10. Overall, the CHCI values of the Pareto solutions are significantly lower than the training and test dataset, indicating the potential further improvement of environmental quality via optimized urban design.

Furthermore, the Pareto front roughly consists of two segments: the upper left wing running parallel with the equi-CHCI contours and the lower right tail with increasing CHCI. The segment of Pareto front with (roughly) constant CHCI can be physically interpretated as that the optimal urban designs for mitigating carbon emission can be obtained with the trade-off of compromising heat mitigation. Yet, the total efficacy of the combined benefit of carbon-heat mitigation is achieved with constant CHCI. The lower right tail, in contrast, signals that if urban system design put more weight on the cooling effect, as a consequence, the objective of carbon emissions will be strongly degraded. This is manifested in that the right tail extends in the direction where CHCI increases, meaning the combined benefit of carbon-heat mitigation will be severely hampered: only marginal cooling effect can be obtained at the expense of significant increases in carbon emission.

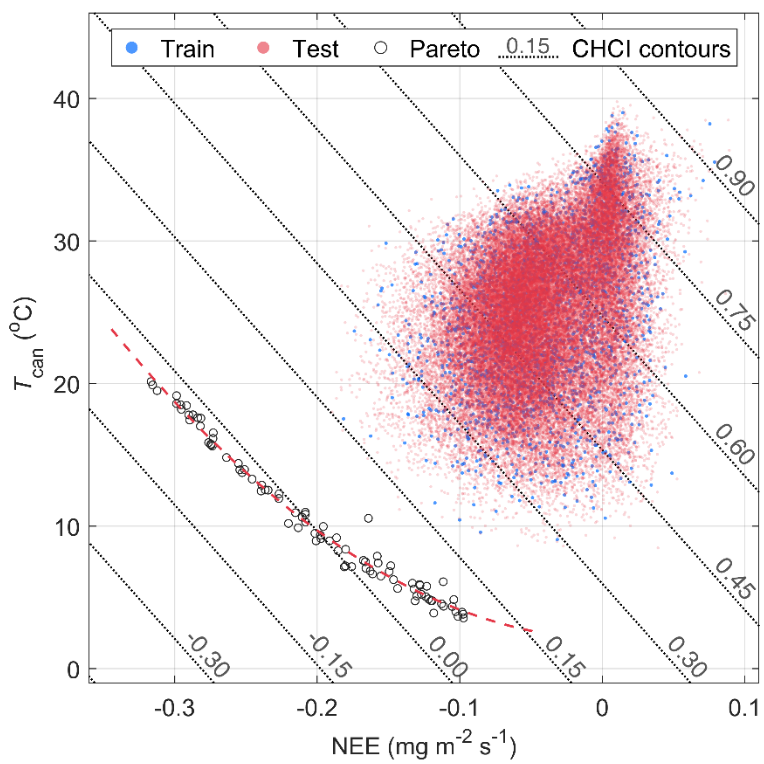

Figure 4.3 Scatter plots of the original dataset and the Pareto solutions found via GA multi-objective optimization. The red dashed line indicates the Pareto front formed by Pareto solutions. The dotted lines in the background indicate the contours of CHCI.

Note that here we only consider two essential measures of urban environmental quality. If more environmental metrics are to be included (e.g., health risks of urban residents due to degraded thermal/air quality), the multi-objective optimization will likely produce smaller (due to more optimization constraints) solution domain with lowest CHCI as the candidate for urban system design. But the trade-offs among diverse environmental indicators will remain the guiding principles for researchers and policy makers to design and assess more livable cities using multi-objective optimization.

4.2.3 Implications to Urban System Design

For optimal urban system design, one would seek for the urban characteristics that lead to Pareto solutions. The deviations of these parameters from their *status quo* values indicate the potential urban system design for planners to ammolite the thermal and carbon environments in cities. Figure 4.4a shows the histograms of initial and optimized (Pareto solutions) distributions of the 24 critical design parameters. Among the Pareto solutions (n = 134), we found that the key parameters shared similar values skewed to the edge of prescribed boundaries from Table 4.1. Overall, wide street (W), low-rise building (H), high vegetation coverage (f_v), dense lawns (LAI_G), and small bare soil fraction (f_s) are most likely to furnish Pareto solutions for thermal and carbon mitigations. To achieve desirable environmental benefits, these urban features need to fall within a small range (Figure 4.4b). Good environmental performance is also associated with high trees (h_T) with large crown (r_T) and dense canopy (LAI_T). Environmental responses (i.e., T_{can} and NEE) are not sensitive to parameters related to trees than those related to urban street morphology and land use, yet tree parameters play important roles affecting both heat and CO_2 exchanges in urban environment (P. Li & Z.-H. Wang 2021a). As a result of heat mitigation, urban greenery saves building energy consumption during summertime, indirectly reducing CO_2 emissions induced by fossil fuel power generation (H. Akbari 2002). This study only considers biogenic CO_2 exchange. The importance of greenery-related urban features (i.e., f_v, f_s, LAI_G, LAI_T, h_T, r_T, etc.) might be more substantial if point source emissions from fossil fuel power plants are included.

Unlike the parameters of street canyon geometry and plant properties, no significant skewness of material properties of pavement and building materials are observed, except for the albedo of vegetated ground (aG_3) and heat capacity (cW_1) and thermal conductivity (kW_1) of building walls. Albedo of vegetated ground (aG_3) directly affects the energy flux and the skin temperature of ground vegetation (i.e., urban lawns) and controls the rates of evapotranspiration, photosynthesis, and respiration. Active evapotranspiration dissipates surface energy via latent heat (F. Aram et al. 2019; J. Yang & Z.-H. Wang 2017), triggering changes in the ambient temperature and further altering biogenic CO_2 exchanges through physiological processes. In addition, thermal properties of building walls regulate the energy exchange rate between building and canyon atmosphere, more effectively than roofs, especially if the building interior thermal environment is regulated by the operation of heating, ventilation, and air conditioning (HVAC) systems or effective (green) building energy designs (C. Wang et al. 2021a).

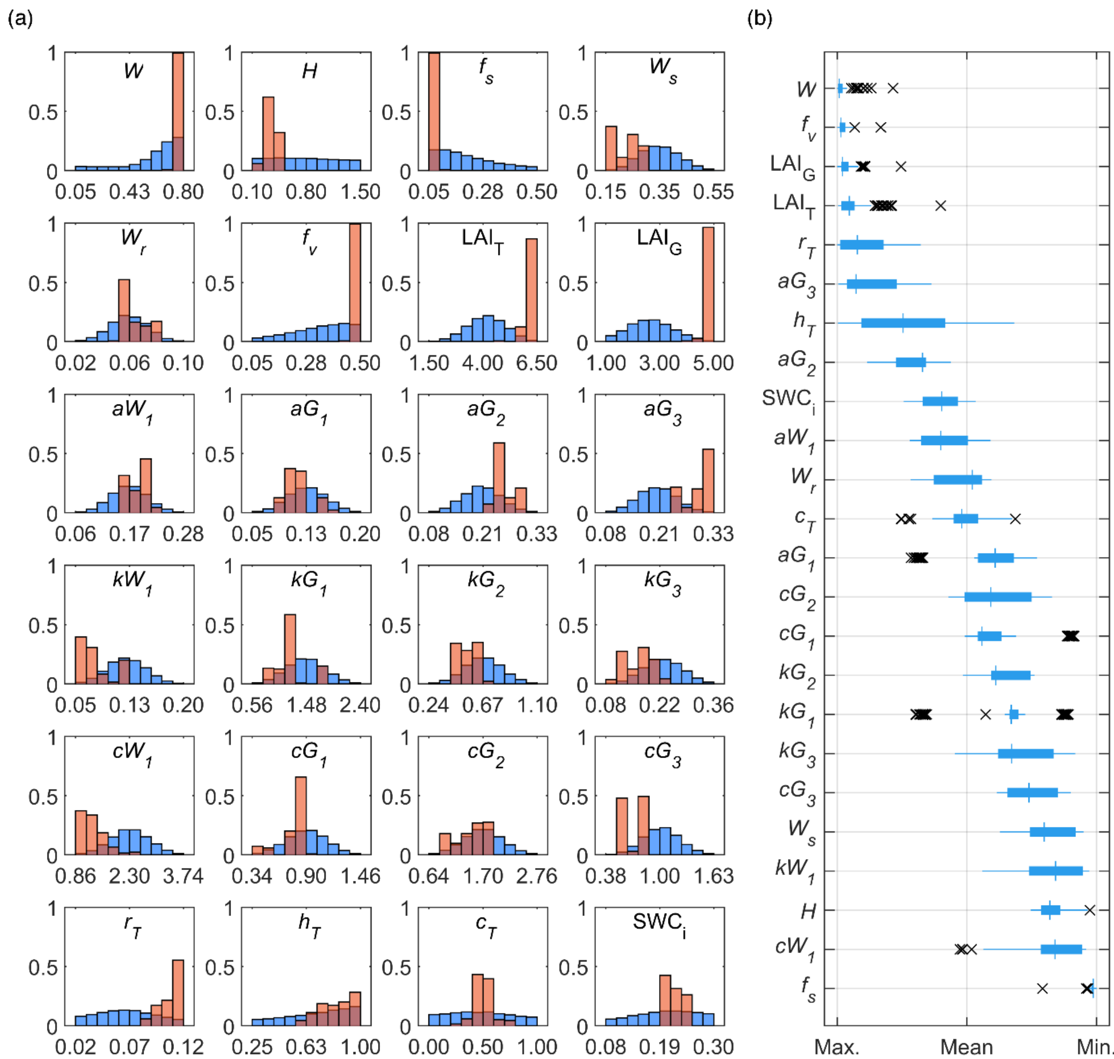

Figure 4.4 Distributions of the urban features used in GPR surrogate and GA optimization. (a) Histograms (Normalized to Probability) of 24 urban features in original dataset (blue) and pareto solutions (orange), and (b) Boxplot of the parameters that lead to Pareto solutions. Values are normalized by Eq. (4.7). Max. Mean and Min. represent the numerical range of urban features in Table 4.1.

It is noteworthy that initial soil moisture (SWCi) shows limited sensitivity with the optimal mean nearly identical to its initial value (Figure 4.4b). In urban environment, scheduled irrigation controls soil moisture, therefore the optimal irrigation amount exists corresponding to the optimal soil moisture. The finding is consistence with P. Li and Z.-H. Wang (2021a), where it is found that excessive irrigation may not help to mitigate carbon emission. This is due to the fact that the extra moisture can promote soil respiration (hence increase carbon emission), whereas the marginal cooling due to extra irrigation is not significant. This effect has been corroborated by E.R. Vivoni et al. (2020), based on a year-long in-situ measurement at a desert urban park, and was referred to as an “oasis effect” of urban irrigation that enhances evapotranspiration and CO_2 exchanges. It is also noteworthy that the tail observed in the Pareto front in Figure 4.3 with degraded co-benefit of heat and carbon mitigation can be largely attributed to this effect as well.

Overall, the good agreement between the results of the GA multi-objective optimization and previous physically-based simulations (P. Li & Z.-H. Wang 2021a) underlines the reliability and fidelity of the ML surrogates in the current study. Results show that specific urban system design strategies for effective mitigation of heat and carbon emissions include more urban green spaces, choices of urban vegetation types, meticulous management of irrigation schedule, and adoption of smart building and pavement materials. The ML-based surrogates and optimization algorithms can be used in the place of physical models with significantly reduced complexity and computational cost, and furnish excellent operative models for fast decision making. Nevertheless, as revealed by this study, it is of critical importance to re-iterate here that multi-objective optimizations are intrinsically constrained by the competing interest among diverse objectives. Furthermore, the GA optimization method in this study helps to inform policy makers and practitioners at the onset of planning stage, and to gauge their preference of specific or compound design objectives, e.g., improvement of thermal comfort, air quality, building energy efficiency, or reduction of health risks, etc.

4.3 Future Development

This study aims to provide a practical toolkit to design and evaluate the impact of urban characteristics on improving the livability of urban environment, based on ML surrogates trained on a simulated dataset. We adopt GPR in our applications to showcase the performance of ML emulation in terms of model accuracy and stability. However, many other popular ML or deep learning algorithms, such as Random Forest, support vector machine, or deep neural networks, can be adopted for urban system design depending on specific applications or the user preference. For example, support vector machine with RBF kernel is expected to outperform GPR when training data is scarce (T. Akhtar & C.A. Shoemaker 2016; S. Razavi et al. 2012).

The design optimization in this study is primarily based on ML models without the aid from physically-based UCM. Theoretically, ML emulations are expected to be more accurate within the range of training data than when it is used for extrapolation. This caveat will be relaxed by adaptive learning with dataset continuously retrieved from observation or numerical modeling to retrain the ML models during optimization. Adaptive learning could further improve the model accuracy and optimization performance but might sacrifice model simplicity and practicality for non-machine learners (i.e., urban planner/designers and decision makers).

In this study, we focus on heat and carbon emissions as the indicator of the urban environmental quality. Through they are the major concerns amid the global climate change, many other factors affect the comfort and health of urban dwellers that should be considered in sustainable urban development. For example, relative humidity and thermal radiation (i.e., ultraviolet, UV) play important roles in human thermal comfort and their influence varies among climate regions (A.M. Abdel-Ghany et al. 2013; M.M. Baruti et al. 2019). Thermal discomfort caused by undesired relative humidity and excessive UV exposure can be mitigated by proper urban designs of urban geometry, building and pavement materials, green and blue spaces (D. Lai et al. 2019). Moreover, air pollutions such as high levels of ozone and particulate matters (PM) concentration can be alleviated by street trees, though the mitigation effect is highly dependent on tree location and species (Y. Barwise & P. Kumar 2020) and requires dedicated tree models to quantify (E. Riondato et al. 2020). As shown by the Pareto solutions in Figure 5.4, exclusive urban planning objectives, such as UHI mitigation by reflective pavements, often lead to severe compromise of other environmental qualities (e.g., carbon emissions). Such one-sidedness in urban planning strategies has practically gained upper hand in policies of some local municipalities, which leads to many unintended physical consequences in the real world (J. Yang et al. 2015). It is important that urban practitioners bear in mind the potential trade-offs of multi-objective designs, and more sustainable urban planning strategies should account for the interactions of total urban system dynamics, instead of trying to "optimize" for singular environmental indicators (in particular, heat mitigation).

Furthermore, the high computational efficiency of ML emulation can enhance the performance and predictive capacity of regional urban hydroclimate modeling by serving as surrogates of multi-scale numerical platforms such as the widely-used Weather Research and Forecast (WRF) model (W.C. Skamarock et al. 2021). Currently, WRF resolves urban land surface using WRF-UCM coupling framework, which allows simple configuration of urban characteristics with limited urban types. Comparing to the simplified UCM in WRF model, ML models learned from full version of UCM will produce more detailed and accurate results with much improved computational economy. As cities are more vulnerable in climate change than other nature areas, the improvement in computation speed and accuracy are not trivial in terms of the sustainable development of the human society.

4.4 Concluding Remarks

This study presents a method emulating a complex urban land surface model using machine learning, aiding the direct interpretation of modeling results for urban planners and policymakers who might have less knowledge on urban land surface models and computing coding. The machine learning surrogate models inherit the advantages the physical-based ASLUM v4.1 model in terms of core dynamics, accuracy, and high resolution, with enhanced computational efficiency and user-friendliness to practitioners. Based on scenario comparison and optimization under constraints, specific mitigation strategies can be derived for both existing and developing urban areas. The versatility of the proposed method and its further improvement (e.g., web-based and graphic user interface development) will help to foster decision making processes and enable policy makers and urban planners to gain deeper and more holistic insight into sustainable solutions that promotes the overall livability of cities.

The transition from complex process-based modeling to ML-based protocols, albeit at its infancy, is transformative and has the potential to furnish a new paradigm in urban system modeling using advanced computer techniques, and further our fundamental understanding of the complex urban ecosystem and the interactions among its diverse components. Future work is planned to take the full advantage of data-driven techniques to form comprehensive and systematic views of compound urban environmental assessment including UHI, building energy efficiency, ecosystem services, air quality, anthropogenic CO_2 emission, etc.

CHAPTER 5

CONCLUSIONS AND PERSPECTIVES

5.1 Conclusions and Implications

The dissertation presents the development of a new algorithm to quantify the CO_2 exchange in urban area as well as the effort of model implementation from urban design and management perspectives. Based on the existing urban land surface modeling platform, the new algorithm proposed in this dissertation assesses the CO_2 exchange from biogenic sectors by coupling photosynthesis and respiration models, and from anthropogenic sectors by applying the spatially gridded data derived from inventory information, remote sensing imagery, and statistically learning techniques. The offline simulation (i.e. without the coupling to regional climate models) is tested against in-situ measurement over a typical single family residential neighborhood and achieves satisfactory accuracy. The total CO_2 flux measured from the eddy covariance system is decomposed into the release from traffic, human respiration, soil respiration, and plant respiration and photosynthesis. The traffic emission dominates the carbon efflux of the neighborhood, followed by soil respiration over the degraded turf in the front and back yards. It is noteworthy that though the vegetation fraction of the study area is very limit, they can offset 30% of the total emission from anthropogenic sectors annually. Evidence shows that residential lots have potential to achieve carbon neutrality via proper landscaping management, thus can further contribute to the city reduction goal against the global climate change.

To assess the impact of urban greening practices on heat and carbon dynamics, we set up a series of numerical experiments to mimic the change of land use and irrigation scheme in a residential neighborhood. Both increasing grassland fraction and tree coverage will lead to environmental co-benefits regarding the mitigation of heat and CO_2 emissions. Comparing to the linear relation between cooling and tree coverage, the change in NEE is non-linear mainly due to the combined mechanisms in which additional tree coverage provides extra biomass for photosynthesis, suppresses soil respiration from cooling, but intercepts PAR for low level grassland. We also find insufficient irrigation significantly inhibits the plant photosynthesis rate, whereas benefit from excessive irrigation is marginal. When the land use is dominated by bare soil (often as a consequence of degraded turf), increasing irrigation will sometimes promote soil respiration and offset the CO_2 uptake from plants. The optimum irrigation amount is highly landscape-dependent and needs to be estimated carefully to improve the overall environmental quality.

Furthermore, we emulate the physical based urban canopy model by adopting Gaussian Process regression, a widely use machine learning algorithm, to improve the computational efficiency and practicality of the modeling framework. In addition, the machine learning surrogate models are used for multi-objective optimization to investigate the optimum configuration of an urban neighborhood to achieve the best cooling and carbon reduction purpose. Within a wide range of urban settings, we find the overall environmental quality will be mostly affected by street canyon aspect ratio and land use, followed by the design and management of green spaces such as vegetation density, tree location, tree height, irrigation, etc. Building and pavement materials play a minor role comparing to the parameters related to urban morphology and urban greening. The machine learning surrogate models and the subsequent optimization algorithm largely improve the versatility and practicality of urban land surface simulation, thus enable the urban practitioners who might not be familiar with modeling and computer coding to operate the simulation and interpret the results.

In summary, the key findings of this dissertation highlight the interplay between thermal and carbon environment in cities and imply the potential of co-benefit of heat and carbon mitigation by utilizing the biogenic functions of urban vegetation and urban greening. The numerical experiments also unveil the possible trade-offs between thermal and carbon environment from certain urban greening actions. The entangled dynamics and considerations will be even more complex from environmental, financial, and societal perspectives, therefore are reserved for future exploration.

5.2 Future Work

The modeling framework developed in this dissertation (Chapter 2) presents a unique land surface model for urban ecosystem service. The current effort implements the model at a neighborhood scale over real-world and pre-designed scenarios (Chapter 3). Simulations over a broader spatial scale (i.e. a city, city clusters, or regional scale) are of high research interests, especially for assessing cities' impact on global climate. The versatility of the coupled UCM-CO_2 framework allows users to apply the model in a spatially distributed mode, with the information of urban morphology derived from inventory or remote sensing data. The regional surface energy and CO_2 flux can be aggregated from each unit cell within the modeling domain. For the regional scale simulation, one can adopt WRF-UCM framework to provide meteorological forcing for the subsequent photosynthesis and soil respiration models. Previously, R. Ahmadov et al.

(2007) coupled WRF with Vegetation Photosynthesis and Respiration Model (VPRM, P. Mahadevan et al. 2008) as the first attempt to quantify the weather-informed land surface dynamics on the spatiotemporal variability of atmospheric CO_2 fluxes and concentrations. It is noteworthy that WRF-VPRM is designed to quantify CO_2 exchange from natural land. Its main objective is to estimate CO_2 concentration over a large scale by resolving the turbulent transport in the atmosphere. In contrast, WRF-UCM focuses on the accurate representation of the urban environment, thus users can estimate vegetation behaviors and test the influence of urban greening strategies in a broader spatial context. As an example, Figure 5.1 shows the irrigation-induced change of NEE during the summer months (May to August) of 2013 to 2015 in urban areas over the contiguous United States (CONUS). The preliminary result illustrates the apparent spatial variation, with the manifest decrease of NEE in the Great Lakes region and increase of NEE in west coast cities, due to the same irrigation strategy. When relating the irrigation-induced cooling to the change of NEE, we observe either environmental co-benefits (Great Lakes region) or trade-offs (west coast) caused by urban irrigation. The regional scale simulation implies the carbon reduction strategies need to be city or climate dependent, thus a holistic understating and accurate quantification to the heat and carbon dynamics in urban area is necessary in sustainable urban planning and landscaping management.

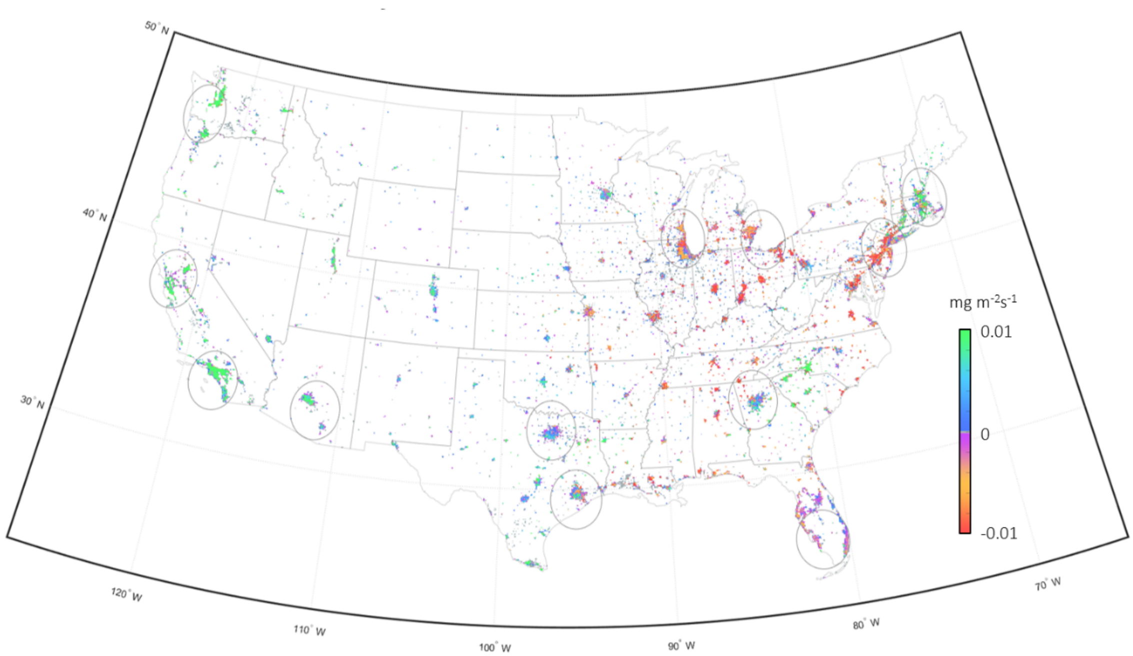

Figure 5.1 Irrigation-induced Ecosystem Service Change over CONUS.

The implementation of the machine learning methods to urban land surface modeling greatly improves the computational efficiency and the practicality of UCM-CO_2. Nevertheless, it still requires the users to have basic coding skills to operate. To better inform urban practitioners, such as city officials, policymakers, urban planners, and landscape designers, a user-friendly decision support system is necessary. For example, coding UCM-CO_2 using a universal and open-source programming language like Python and R will allow users from different platforms sharing the same workflow from data preprocessing to result interpretation and visualization (T. Sun & C.S.B. Grimmond 2019).

In this dissertation, we select in-canyon temperature and net ecosystem exchange as the two major measures to evaluate the environmental quality in cities. For the carbon reduction purpose, it is meaningful to consider CO_2 emission associated with energy consumption in buildings. Aside from the linkages between thermal and carbon environment within the biogenic sectors, cooling from urban greening could lower building energy cost from air conditioning and possibly reduce the total carbon footprint of a city. Similarly, the optimal urban design will require a holistic view from the consideration of the restriction of water resources, financial cost of irrigation and landscaping, local power mix, etc., although not all factors will be affected by meteorological conditions. In addition to the "compound carbon and heat index" introduced in Chapter 4, a more comprehensive index is desired in the future development of UCM-CO_2, especially in the offline simulation where modeling of fine details is possible. The future work of including more and practical urban environmental measures in physical modeling as well as ML-driven multi-objective optimization schemes, challenging as it will be, will enable us to extend the knowledge gained in this dissertation work to broader context such as to meet the goal of Paris Climate Agreement and/or th global carbon neutrality.

REFERENCES

Abdel-Ghany, A.M., Al-Helal, I.M., & Shady, M.R. (2013). Human Thermal Comfort and Heat Stress in an Outdoor Urban Arid Environment: A Case Study. *Advances in Meteorology, 2013*, 693541. http://doi.org/10.1155/2013/693541

Ahmadov, R., Gerbig, C., Kretschmer, R., Koerner, S., Neininger, B., Dolman, A.J., & Sarrat, C. (2007). Mesoscale covariance of transport and CO_2 fluxes: Evidence from observations and simulations using the WRF-VPRM coupled atmosphere-biosphere model. *Journal of Geophysical Research: Atmospheres, 112*(D22). http://doi.org/https://doi.org/10.1029/2007JD008552

Akbari, H. (2002). Shade trees reduce building energy use and CO_2 emissions from power plants. *Environmental Pollution, 116*, S119-S126. http://doi.org/https://doi.org/10.1016/S0269-7491(01)00264-0

Akhtar, T., & Shoemaker, C.A. (2016). Multi objective optimization of computationally expensive multi-modal functions with RBF surrogates and multi-rule selection. In: Springer New York LLC.

Aram, F., Higueras Garcia, E., Solgi, E., & Mansournia, S. (2019). Urban green space cooling effect in cities. *Heliyon, 5*(4), e01339. http://doi.org/10.1016/j.heliyon.2019.e01339

Arnfield, A.J. (2003). Two decades of urban climate research: a review of turbulence, exchanges of energy and water, and the urban heat island. *International Journal of Climatology, 23*(1), 1-26. http://doi.org/10.1002/joc.859

Bae, J., & Ryu, Y. (2017). Spatial and temporal variations in soil respiration among different land cover types under wet and dry years in an urban park. *Landscape and Urban Planning, 167*, 378-385. http://doi.org/10.1016/j.landurbplan.2017.07.020

Balling Jr, R.C., Cerveny, R.S., & Idso, C.D. (2001). Does the urban CO_2 dome of Phoenix, Arizona contribute to its heat island? *Geophysical Research Letters, 28*(24), 4599-4601. http://doi.org/https://doi.org/10.1029/2000GL012632

Barrett, K.E., Barman, S.M., Boitano, S., Brooks, H. (2009) Ganong's Review of MedicalPhysiology, 23rd ed., McGraw-Hill Medical, 726 pp.

Baruti, M.M., Johansson, E., & Åstrand, J. (2019). Review of studies on outdoor thermal comfort in warm humid climates: challenges of informal urban fabric. *International Journal of Biometeorology, 63*(10), 1449-1462. http://doi.org/10.1007/s00484-019-01757-3

Barwise, Y., & Kumar, P. (2020). Designing vegetation barriers for urban air pollution abatement: a practical review for appropriate plant species selection. *npj Climate and Atmospheric Science, 3*(1), 12. http://doi.org/10.1038/s41612-020-0115-3

Bergeron, O., & Strachan, I.B. (2011). CO_2 sources and sinks in urban and suburban areas of a northern mid-latitude city. *Atmospheric Environment, 45*(8), 1564-1573. http://doi.org/10.1016/j.atmosenv.2010.12.043

Bessa, M.A., Bostanabad, R., Liu, Z., Hu, A., Apley, D.W., Brinson, C., . . . Liu, Wing K. (2017). A framework for data-driven analysis of materials under uncertainty: Countering the curse of dimensionality. *Computer Methods in Applied Mechanics and Engineering, 320*, 633-667. http://doi.org/https://doi.org/10.1016/j.cma.2017.03.037

Cai, Q., Yan, X., Li, Y., & Wang, L. (2018). Global patterns of human and livestock respiration. *Sci Rep, 8*(1), 9278. http://doi.org/10.1038/s41598-018-27631-7

Cawley, G.C., & Talbot, N.L.C. (2007). Preventing over-fitting during model selection via Bayesian regularisation of the hyper-parameters. *Journal of Machine Learning Research, 8*(31), 841-861.

Cawley, G.C., & Talbot, N.L.C. (2010). On over-fitting in model selection and subsequent selection bias in performance evaluation. *Journal of Machine Learning Research, 11*, 2079-2107.

Chen, F., Kusaka, H., Bornstein, R., Ching, J., Grimmond, C.S.B., Grossman-Clarke, S., . . . Zhang, C. (2011). The integrated WRF/urban modelling system: development, evaluation, and applications to urban environmental problems. *International Journal of Climatology, 31*(2), 273-288. http://doi.org/https://doi.org/10.1002/joc.2158

Chow, W.T.L. (2017). *Eddy covariance data measured at the CAP LTER flux tower located in the west Phoenix, AZ neighborhood of Maryvale from 2011-12-16 through 2012-12-31*.

Chow, W.T.L., & Brazel, A.J. (2012). Assessing xeriscaping as a sustainable heat island mitigation approach for a desert city. *Building and Environment, 47*, 170-181. http://doi.org/10.1016/j.buildenv.2011.07.027

Chow, W.T.L., Volo, T.J., Vivoni, E.R., Jenerette, G.D., & Ruddell, B.L. (2014). Seasonal dynamics of a suburban energy balance in Phoenix, Arizona. *International Journal of Climatology, 34*(15), 3863-3880. http://doi.org/10.1002/joc.3947

Christen, A., Coops, N.C., Crawford, B.R., Kellett, R., Liss, K.N., Olchovski, I., . . . Voogt, J.A. (2011). Validation of modeled carbon-dioxide emissions from an urban neighborhood with direct eddy-covariance measurements. *Atmospheric Environment, 45*(33), 6057-6069. http://doi.org/10.1016/j.atmosenv.2011.07.040

Churkina, G. (2016). The Role of Urbanization in the Global Carbon Cycle. *Frontiers in Ecology and Evolution, 3*. http://doi.org/10.3389/fevo.2015.00144

Collatz, G.J., Ball, J.T., Grivet, C., & Berry, J.A. (1991). Physiological and environmental regulation of stomatal conductance, photosynthesis and transpiration: a model that includes a laminar boundary layer. *Agricultural and Forest Meteorology, 54*(2), 107-136. http://doi.org/https://doi.org/10.1016/0168-1923(91)90002-8

Collatz, G.J., Ribas-Carbo, M., & Berry, J.A. (1992). Coupled Photosynthesis-Stomatal Conductance Model for Leaves of C_4 Plants. *Functional Plant Biology, 19*(5), 519-538.

Contosta, A.R., Lerman, S.B., Xiao, J., & Varner, R.K. (2020). Biogeochemical and socioeconomic drivers of above- and below-ground carbon stocks in urban residential yards of a small city. *Landscape and Urban Planning, 196*. http://doi.org/10.1016/j.landurbplan.2019.103724

Crawford, A.J., McLachlan, D.H., Hetherington, A.M., & Franklin, K.A. (2012). High temperature exposure increases plant cooling capacity. *Curr Biol, 22*(10), R396-397. http://doi.org/10.1016/j.cub.2012.03.044

Crawford, B., & Christen, A. (2014). Spatial variability of carbon dioxide in the urban canopy layer and implications for flux measurements. *Atmospheric Environment, 98*, 308-322. http://doi.org/10.1016/j.atmosenv.2014.08.052

Crawford, B., Grimmond, C.S.B., & Christen, A. (2011). Five years of carbon dioxide fluxes measurements in a highly vegetated suburban area. *Atmospheric Environment, 45*(4), 896-905. http://doi.org/10.1016/j.atmosenv.2010.11.017

Dass, P., Houlton, B.Z., Wang, Y., & Warlind, D. (2018). Grasslands may be more reliable carbon sinks than forests in California. *Environmental Research Letters, 13*(7), 074027. http://doi.org/10.1088/1748-9326/aacb39

Deb, K. (2001). *Multi-Objective optimization using evolutionary algorithms*. Chichester, England: John Wiley & Sons.

Decina, S.M., Hutyra, L.R., Gately, C.K., Getson, J.M., Reinmann, A.B., Short Gianotti, A.G., & Templer, P.H. (2016). Soil respiration contributes substantially to urban carbon fluxes in the greater Boston area. *Environ Pollut, 212*, 433-439. http://doi.org/10.1016/j.envpol.2016.01.012

Diwekar, U.M. (2003). Optimization Under Uncertainty. In U. M. Diwekar (Ed.), *Introduction to Applied Optimization* (pp. 145-208). Boston, MA: Springer US.

Dyukarev, E.A. (2017). Partitioning of net ecosystem exchange using chamber measurements data from bare soil and vegetated sites. *Agricultural and Forest Meteorology, 239*, 236-248. http://doi.org/10.1016/j.agrformet.2017.03.011

Fernando, H.J.S. (2010). Fluid Dynamics of Urban Atmospheres in Complex Terrain. *Annual Review of Fluid Mechanics, 42*(1), 365-389. http://doi.org/10.1146/annurev-fluid-121108-145459

Field, C.B., Jackson, R.B., & Mooney, H.A. (1995). Stomatal responses to increased CO_2: implications from the plant to the global scale. *Plant, Cell & Environment, 18*(10), 1214-1225. http://doi.org/https://doi.org/10.1111/j.1365-3040.1995.tb00630.x

Gately, C., Hutyra, L.R., & Wing, I.S. (2019). DARTE Annual On-road CO_2 Emissions on a 1-km Grid, Conterminous USA V2, 1980-2017. In: ORNL Distributed Active Archive Center.

Gately, C.K., & Hutyra, L.R. (2017). Large Uncertainties in Urban-Scale Carbon Emissions. *Journal of Geophysical Research: Atmospheres, 122*(20), 11,242-211,260. http://doi.org/10.1002/2017jd027359

Gately, C.K., Hutyra, L.R., & Sue Wing, I. (2015). Cities, traffic, and CO_2: A multidecadal assessment of trends, drivers, and scaling relationships. *Proc Natl Acad Sci U S A, 112*(16), 4999-5004. http://doi.org/10.1073/pnas.1421723112

Goret, M., Masson, V., Schoetter, R., & Moine, M.-P. (2019). Inclusion of CO_2 flux modelling in an urban canopy layer model and an evaluation over an old European city centre. *Atmospheric Environment: X, 3*. http://doi.org/10.1016/j.aeaoa.2019.100042

Grimmond, C.S.B., Best, M., Barlow, J., Arnfield, A.J., Baik, J.J., Baklanov, A., . . . Williamson, T. (2009). Urban Surface Energy Balance Models: Model Characteristics and Methodology for a Comparison Study. In A. Baklanov, G. Sue, M. Alexander, & M. Athanassiadou (Eds.), *Meteorological and Air Quality Models for Urban Areas* (pp. 97-123). Berlin, Heidelberg: Springer Berlin Heidelberg.

Grimmond, C.S.B., Blackett, M., Best, M.J., Baik, J.J., Belcher, S.E., Beringer, J., . . . Zhang, N. (2011). Initial results from Phase 2 of the international urban energy balance model comparison. *International Journal of Climatology, 31*(2), 244-272. http://doi.org/10.1002/joc.2227

Grimmond, C.S.B., Blackett, M., Best, M.J., Barlow, J., Baik, J.J., Belcher, S.E., . . . Zhang, N. (2010). The International Urban Energy Balance Models Comparison Project: First Results from Phase 1. *Journal of Applied Meteorology and Climatology, 49*(6), 1268-1292. http://doi.org/10.1175/2010JAMC2354.1

Grimmond, C.S.B., King, T.S., Cropley, F.D., Nowak, D.J., & Souch, C. (2002). Local-scale fluxes of carbon dioxide in urban environments: methodological challenges and results from Chicago. *Environmental Pollution, 116*, S243-S254. http://doi.org/https://doi.org/10.1016/S0269-7491(01)00256-1

Grote, M., Williams, I., Preston, J., & Kemp, S. (2016). Including congestion effects in urban road traffic CO_2 emissions modelling: Do Local Government Authorities have the right options? *Transportation Research Part D: Transport and Environment, 43*, 95-106. http://doi.org/10.1016/j.trd.2015.12.010

Gurney, K.R. (2014). Recent research quantifying anthropogenic CO_2 emissions at the street scale within the urban domain. *Carbon Management, 5*(3), 309-320. http://doi.org/10.1080/17583004.2014.986849

Gurney, K.R., Liang, J., O'Keeffe, D., Patarasuk, R., Hutchins, M., Huang, J., . . . Song, Y. (2019). Comparison of Global Downscaled Versus Bottom-Up Fossil Fuel CO_2 Emissions at the Urban Scale in Four U.S. Urban Areas. *Journal of Geophysical Research: Atmospheres, 124*(5), 2823-2840. http://doi.org/https://doi.org/10.1029/2018JD028859

Gurney, K.R., Mendoza, D.L., Zhou, Y., Fischer, M.L., Miller, C.C., Geethakumar, S., & de la Rue du Can, S. (2009). High Resolution Fossil Fuel Combustion CO_2 Emission Fluxes for the United States. *Environmental Science & Technology, 43*(14), 5535-5541. http://doi.org/10.1021/es900806c

Gurney, K.R., Razlivanov, I., Song, Y., Zhou, Y., Benes, B., & Abdul-Massih, M. (2012). Quantification of Fossil Fuel CO_2 Emissions on the Building/Street Scale for a Large U.S. City. *Environmental Science & Technology, 46*(21), 12194-12202. http://doi.org/10.1021/es3011282

He, W., Zeng, Y., & Li, G. (2020). An adaptive polynomial chaos expansion for high-dimensional reliability analysis. *Structural and Multidisciplinary Optimization, 62*(4), 2051-2067. http://doi.org/10.1007/s00158-020-02594-4

Hilbert, D., Roman, L., Koeser, A., Vogt, J., & Van Doorn, N. (2018). Urban tree mortality: a literature review. *Arboriculture & Urban Forestry, 45*(5), 167-200. http://doi.org/10.48044/jauf.2019.015

Hutyra, L.R., Duren, R., Gurney, K.R., Grimm, N., Kort, E.A., Larson, E., & Shrestha, G. (2014). Urbanization and the carbon cycle: Current capabilities and research outlook from the natural sciences perspective. *Earth's Future, 2*(10), 473-495. http://doi.org/10.1002/2014ef000255

Jacobs, A.F.G., Ronda, R.J., & Holtslag, A.A.M. (2003). Water vapour and carbon dioxide fluxes over bog vegetation. *Agricultural and Forest Meteorology, 116*(1-2), 103-112. http://doi.org/10.1016/s0168-1923(02)00229-0

Jacobs, C.M.J. (1994). *Direct Impact of Atmospheric CO_2Enrichment on Regional Transpiration.* (28227373 Ph.D.), Wageningen University and Research, Ann Arbor.

Jacobson, A.R., Schuldt, K.N., Miller, J.B., Oda, T., Tans, P., Arlyn, A., . . . Miroslaw, Z. (2020). CarbonTracker CT2019B. In: NOAA Global Monitoring Laboratory.

Järvi, L., Havu, M., Ward, H.C., Bellucco, V., McFadden, J.P., Toivonen, T., . . . Grimmond, C.S.B. (2019). Spatial Modeling of Local-Scale Biogenic and Anthropogenic Carbon Dioxide Emissions in Helsinki. *Journal of Geophysical Research: Atmospheres, 124*(15), 8363-8384. http://doi.org/https://doi.org/10.1029/2018JD029576

Kirschbaum, M.U.F. (1995). The temperature dependence of soil organic matter decomposition, and the effect of global warming on soil organic C storage. *Soil Biology and Biochemistry, 27*(6), 753-760. http://doi.org/https://doi.org/10.1016/0038-0717(94)00242-S

Koerner, B., & Klopatek, J. (2002). Anthropogenic and natural CO_2 emission sources in an arid urban environment. *Environmental Pollution, 116*, S45-S51. http://doi.org/https://doi.org/10.1016/S0269-7491(01)00246-9

Konarska, J., Uddling, J., Holmer, B., Lutz, M., Lindberg, F., Pleijel, H., & Thorsson, S. (2016). Transpiration of urban trees and its cooling effect in a high latitude city. *Int J Biometeorol, 60*(1), 159-172. http://doi.org/10.1007/s00484-015-1014-x

Kusaka, H., Kondo, H., Kikegawa, Y., & Kimura, F. (2001). A Simple Single-Layer Urban Canopy Model For Atmospheric Models: Comparison With Multi-Layer And Slab Models. *Boundary-Layer Meteorology, 101*(3), 329-358. http://doi.org/10.1023/A:1019207923078

Lahr, E.C., Dunn, R.R., & Frank, S.D. (2018). Getting ahead of the curve: cities as surrogates for global change. *Proceedings of the Royal Society B: Biological Sciences, 285*(1882), 20180643. http://doi.org/doi:10.1098/rspb.2018.0643

Lai, D., Liu, W., Gan, T., Liu, K., & Chen, Q. (2019). A review of mitigating strategies to improve the thermal environment and thermal comfort in urban outdoor spaces. *Science of The Total Environment, 661*, 337-353. http://doi.org/https://doi.org/10.1016/j.scitotenv.2019.01.062

Landscape Watering by Numbers, 2017. Retrieved from https://wateruseitwisely.com/100-ways-to-conserve/landscape-watering-guide/

Lara, M.V., & Andreo, C.S. (2011). C_4 plants adaptation to high levels of CO_2 and to drought environments. *Abiotic Stress in Plants-Mechanisms and Adaptations*, 415-428.

Lee, S.-H., & Park, S.-U. (2008). A Vegetated Urban Canopy Model for Meteorological and Environmental Modelling. *Boundary-Layer Meteorology, 126*(1), 73-102. http://doi.org/10.1007/s10546-007-9221-6

Lee, S.-H., Lee, H., Park, S.-B., Woo, J.-W., Lee, D.-I., & Baik, J.-J. (2016). Impacts of in-canyon vegetation and canyon aspect ratio on the thermal environment of street canyons: numerical investigation using a coupled WRF-VUCM model. *Quarterly Journal of the Royal Meteorological Society, 142*(699), 2562-2578. http://doi.org/https://doi.org/10.1002/qj.2847

Lemonsu, A., Masson, V., Shashua-Bar, L., Erell, E., & Pearlmutter, D. (2012). Inclusion of vegetation in the Town Energy Balance model for modelling urban green areas. *Geoscientific Model Development, 5*(6), 1377-1393. http://doi.org/10.5194/gmd-5-1377-2012

Leuning, R. (1995). A critical appraisal of a combined stomatal-photosynthesis model for C_3 plants. *Plant, Cell & Environment, 18*(4), 339-355. http://doi.org/https://doi.org/10.1111/j.1365-3040.1995.tb00370.x

Li, P., & Wang, Z.-H. (2019). Estimating evapotranspiration over vegetated surfaces based on wet patch patterns. *Hydrology Research, 50*(4), 1037-1046. http://doi.org/10.2166/nh.2019.034

Li, P., & Wang, Z.-H. (2020a). Modeling carbon dioxide exchange in a single-layer urban canopy model. *Building and Environment, 184*, 107243. http://doi.org/https://doi.org/10.1016/j.buildenv.2020.107243

Li, P., & Wang, Z.-H. (2020b). A Nonequilibrium Thermodynamic Approach for Surface Energy Balance Closure. *Geophysical Research Letters, 47*(3), e2019GL085835. http://doi.org/https://doi.org/10.1029/2019GL085835

Li, P., & Wang, Z.-H. (2021a). Environmental co-benefits of urban greening for mitigating heat and carbon emissions. *Journal of Environmental Management, 293*, 112963. http://doi.org/https://doi.org/10.1016/j.jenvman.2021.112963

Li, P., & Wang, Z.-H. (2021b). Uncertainty and sensitivity analysis of modeling plant CO_2 exchange in the built environment. *Building and Environment, 189*, 107539. http://doi.org/https://doi.org/10.1016/j.buildenv.2020.107539

Litvak, E., Manago, K.F., Hogue, T.S., & Pataki, D.E. (2017). Evapotranspiration of urban landscapes in Los Angeles, California at the municipal scale. *Water Resources Research, 53*(5), 4236-4252. http://doi.org/10.1002/2016wr020254

Lloyd, J., & Taylor, J.A. (1994). On the Temperature Dependence of Soil Respiration. *Functional Ecology, 8*(3), 315-323. http://doi.org/10.2307/2389824

Loridan, T., Grimmond, C.S.B., Grossman-Clarke, S., Chen, F., Tewari, M., Manning, K., . . . Best, M. (2010). Trade-offs and responsiveness of the single-layer urban canopy parametrization in WRF: An offline evaluation using the MOSCEM optimization algorithm and field observations. *Quarterly Journal of the Royal Meteorological Society, 136*(649), 997-1019. http://doi.org/https://doi.org/10.1002/qj.614

Luketich, A.M., Papuga, S.A., & Crimmins, M.A. (2019). Ecohydrology of urban trees under passive and active irrigation in a semiarid city. *PLoS One, 14*(11), e0224804. http://doi.org/10.1371/journal.pone.0224804

Luo, Y., & Zhou, X. (2006). CHAPTER 5 - Controlling Factors. In Y. Luo & X. Zhou (Eds.), *Soil Respiration and the Environment* (pp. 79-105). Burlington: Academic Press.

Macknick, J. (2011). Energy and CO_2 emission data uncertainties. *Carbon Management, 2*(2), 189-205. http://doi.org/10.4155/cmt.11.10

Mahadevan, P., Wofsy, S.C., Matross, D.M., Xiao, X., Dunn, A.L., Lin, J.C., . . . Gottlieb, E.W. (2008). A satellite-based biosphere parameterization for net ecosystem CO_2 exchange: Vegetation Photosynthesis and Respiration Model (VPRM). *Global Biogeochemical Cycles, 22*(2). http://doi.org/https://doi.org/10.1029/2006GB002735

Martilli, A. (2002). Numerical Study of Urban Impact on Boundary Layer Structure

Masson, V. (2000). A Physically-Based Scheme For The Urban Energy Budget In Atmospheric Models. *Boundary-Layer Meteorology, 94*(3), 357-397. http://doi.org/10.1023/A:1002463829265

McDonald, D.B., Grantham, W.J., Tabor, W.L., & Murphy, M.J. (2007). Global and local optimization using radial basis function response surface models. *Applied Mathematical Modelling, 31*(10), 2095-2110. http://doi.org/https://doi.org/10.1016/j.apm.2006.08.008

Meili, N., Manoli, G., Burlando, P., Bou-Zeid, E., Chow, W.T.L., Coutts, A.M., . . . Fatichi, S. (2020). An urban ecohydrological model to quantify the effect of vegetation on urban climate and hydrology (UT&C v1.0). *Geoscientific Model Development, 13*(1), 335-362. http://doi.org/10.5194/gmd-13-335-2020

Meng, L., Mao, J., Zhou, Y., Richardson, A.D., Lee, X., Thornton, P.E., . . . Jia, G. (2020). Urban warming advances spring phenology but reduces the response of phenology to temperature in the conterminous United States. *Proceedings of the National Academy of Sciences, 117*(8), 4228. http://doi.org/10.1073/pnas.1911117117

Mishra, A.A., Mukhopadhaya, J., Alonso, J., & Iaccarino, G. (2020). Design exploration and optimization under uncertainty. *Physics of Fluids, 32*(8), 085106. http://doi.org/10.1063/5.0020858

Mitchell, L.E., Lin, J.C., Bowling, D.R., Pataki, D.E., Strong, C., Schauer, A.J., . . . Ehleringer, J.R. (2018). Long-term urban carbon dioxide observations reveal spatial and temporal dynamics related to urban characteristics and growth. *Proc Natl Acad Sci U S A, 115*(12), 2912-2917. http://doi.org/10.1073/pnas.1702393115

Ng, B.J.L., Hutyra, L.R., Nguyen, H., Cobb, A.R., Kai, F.M., Harvey, C., & Gandois, L. (2015). Carbon fluxes from an urban tropical grassland. *Environ Pollut, 203*, 227-234. http://doi.org/10.1016/j.envpol.2014.06.009

Ngatchou, P., Zarei, A., & El-Sharkawi, A. (2005, 6-10 Nov. 2005). *Pareto Multi Objective Optimization.* Paper presented at the Proceedings of the 13th International Conference on, Intelligent Systems Application to Power Systems.

Norman, J.M., Garcia, R., & Verma, S.B. (1992). Soil surface CO_2 fluxes and the carbon budget of a grassland. *Journal of Geophysical Research: Atmospheres, 97*(D17), 18845-18853. http://doi.org/https://doi.org/10.1029/92JD01348

Oda, T., Maksyutov, S., & Andres, R.J. (2018). The Open-source Data Inventory for Anthropogenic Carbon dioxide (CO_2), version 2016 (ODIAC2016): A global, monthly fossil-fuel CO_2 gridded emission data product for tracer transport simulations and surface flux inversions. *Earth Syst Sci Data, 10*(1), 87-107. http://doi.org/10.5194/essd-10-87-2018

Oke, T.R. (1973). City size and the urban heat island. *Atmospheric Environment (1967), 7*(8), 769-779. http://doi.org/https://doi.org/10.1016/0004-6981(73)90140-6

Oke, T.R. (1982). The energetic basis of the urban heat island. *Quarterly Journal of the Royal Meteorological Society, 108*(455), 1-24. http://doi.org/https://doi.org/10.1002/qj.49710845502

Oke, T.R., Mills, G., Christen, A., & Voogt, J.A. (2017). *Urban Climates*. Cambridge: Cambridge University Press.

Pataki, D.E., Bowling, D.R., & Ehleringer, J.R. (2003). Seasonal cycle of carbon dioxide and its isotopic composition in an urban atmosphere: Anthropogenic and biogenic effects. *Journal of Geophysical Research: Atmospheres, 108*(D23). http://doi.org/https://doi.org/10.1029/2003JD003865

Pataki, D.E., Bowling, D.R., Ehleringer, J.R., & Zobitz, J.M. (2006). High resolution atmospheric monitoring of urban carbon dioxide sources. *Geophysical Research Letters, 33*(3). http://doi.org/https://doi.org/10.1029/2005GL024822

Pinker, R.T., & Laszlo, I. (1992). Modeling Surface Solar Irradiance for Satellite Applications on a Global Scale. *Journal of Applied Meteorology and Climatology, 31*(2), 194-211. http://doi.org/10.1175/1520-0450(1992)031<0194:MSSIFS>2.0.CO;2

Pozzi, F., & Small, C. (2001, 8-9 Nov. 2001). *Exploratory analysis of suburban land cover and population density in the U.S.A.* Paper presented at the IEEE/ISPRS Joint Workshop on Remote Sensing and Data Fusion over Urban Areas (Cat. No.01EX482).

Qi, Y., Dong, Y., Liu, L., Liu, X., Peng, Q., Xiao, S., & He, Y. (2010). Spatial-temporal variation in soil respiration and its controlling factors in three steppes of Stipa L. in Inner Mongolia, China. *Science China Earth Sciences, 53*(5), 683-693. http://doi.org/10.1007/s11430-010-0039-6

Qun, D., & Huizhi, L. (2013). Seven years of carbon dioxide exchange over a degraded grassland and a cropland with maize ecosystems in a semiarid area of China. *Agriculture, Ecosystems & Environment, 173*, 1-12. http://doi.org/https://doi.org/10.1016/j.agee.2013.04.009

Rasmussen, C.E., & Williams, C.K.I. (2006). *Gaussian processes for machine learning*: The MIT Press.

Razavi, S., Tolson, B.A., & Burn, D.H. (2012). Numerical assessment of metamodelling strategies in computationally intensive optimization. *Environmental Modelling & Software, 34*, 67-86. http://doi.org/https://doi.org/10.1016/j.envsoft.2011.09.010

Redon, E., Lemonsu, A., & Masson, V. (2020). An urban trees parameterization for modeling microclimatic variables and thermal comfort conditions at street level with the Town Energy Balance model (TEB-SURFEX v8.0). *Geosci. Model Dev., 13*(2), 385-399. http://doi.org/10.5194/gmd-13-385-2020

Riondato, E., Pilla, F., Sarkar Basu, A., & Basu, B. (2020). Investigating the effect of trees on urban quality in Dublin by combining air monitoring with i-Tree Eco model. *Sustainable Cities and Society, 61*, 102356. http://doi.org/https://doi.org/10.1016/j.scs.2020.102356

Ronda, R.J., de Bruin, H.A.R., & Holtslag, A.A.M. (2001). Representation of the Canopy Conductance in Modeling the Surface Energy Budget for Low Vegetation. *Journal of Applied Meteorology, 40*(8), 1431-1444. http://doi.org/10.1175/1520-0450(2001)040<1431:ROTCCI>2.0.CO;2

Ryu, Y.-H., Bou-Zeid, E., Wang, Z.-H., & Smith, J.A. (2015). Realistic Representation of Trees in an Urban Canopy Model. *Boundary-Layer Meteorology, 159*(2), 193-220. http://doi.org/10.1007/s10546-015-0120-y

Sailor, D.J. (2007). *A bottom-up approach for estimating latent and sensible heat emissions from anthropogenic sources.* Paper presented at the Proceedings of the 7th Symposium on the Urban Environment, American Meteorological Society, Boston.

Sailor, D.J. (2011). A review of methods for estimating anthropogenic heat and moisture emissions in the urban environment. *International Journal of Climatology, 31*(2), 189-199. http://doi.org/https://doi.org/10.1002/joc.2106

Sailor, D.J., & Lu, L. (2004). A top–down methodology for developing diurnal and seasonal anthropogenic heating profiles for urban areas. *Atmospheric Environment, 38*(17), 2737-2748. http://doi.org/https://doi.org/10.1016/j.atmosenv.2004.01.034

Sargent, M., Barrera, Y., Nehrkorn, T., Hutyra, L.R., Gately, C.K., Jones, T., . . . Wofsy, S.C. (2018). Anthropogenic and biogenic CO_2 fluxes in the Boston urban region. *Proc Natl Acad Sci U S A, 115*(29), 7491-7496. http://doi.org/10.1073/pnas.1803715115

Sensitivity to Wind Speed, Urban Morphology, and Rural Soil Moisture. *Journal of Applied Meteorology (1988-2005), 41*(12), 1247-1266.

Skala, V. (2017). RBF Interpolation with CSRBF of Large Data Sets. *Procedia Computer Science, 108*, 2433-2437. http://doi.org/https://doi.org/10.1016/j.procs.2017.05.081

Skamarock, W.C., Klemp, J.B., Dudhia, J., Gill, D.O., Liu, Z., Berner, J., . . . Huang, X.-y. (2021). *A description of the advanced research WRF model version 4.3*.

Smith, I.A., Dearborn, V.K., & Hutyra, L.R. (2019). Live fast, die young: Accelerated growth, mortality, and turnover in street trees. *PLoS One, 14*(5), e0215846. http://doi.org/10.1371/journal.pone.0215846

Song, J., & Wang, Z.-H. (2015). Impacts of mesic and xeric urban vegetation on outdoor thermal comfort and microclimate in Phoenix, AZ. *Building and Environment, 94*, 558-568. http://doi.org/https://doi.org/10.1016/j.buildenv.2015.10.016

Song, J., & Wang, Z.-H. (2016). Evaluating the impact of built environment characteristics on urban boundary layer dynamics using an advanced stochastic approach. *Atmos. Chem. Phys., 16*(10), 6285-6301. http://doi.org/10.5194/acp-16-6285-2016

Song, J., Wang, Z.-H., & Wang, C. (2017). Biospheric and anthropogenic contributors to atmospheric CO_2variability in a residential neighborhood of Phoenix, Arizona. *Journal of Geophysical Research: Atmospheres, 122*(6), 3317-3329. http://doi.org/10.1002/2016jd026267

Stavropulos-Laffaille, X., Chancibault, K., Brun, J.-M., Lemonsu, A., Masson, V., Boone, A., & Andrieu, H. (2018). Improvements to the hydrological processes of the Town Energy Balance model (TEB-Veg, SURFEX v7.3) for urban modelling and impact assessment. *Geoscientific Model Development, 11*(10), 4175-4194. http://doi.org/10.5194/gmd-11-4175-2018

Still, C.J., Berry, J.A., Collatz, G.J., & DeFries, R.S. (2003). Global distribution of C_3 and C_4 vegetation: Carbon cycle implications. *Global Biogeochemical Cycles, 17*(1), 6-1-6-14. http://doi.org/10.1029/2001gb001807

Sun, T., & Grimmond, S. (2019). A Python-enhanced urban land surface model SuPy (SUEWS in Python, v2019.2): development, deployment and demonstration. *Geoscientific Model Development*, 12(7), 2781-2795. http://doi.org/10.5194/gmd-12-2781-2019

Sun, T., Wang, Z.-H., & Ni, G.-H. (2013). Revisiting the hysteresis effect in surface energy budgets. *Geophysical Research Letters, 40*(9), 1741-1747. http://doi.org/https://doi.org/10.1002/grl.50385

Tao, X., Cui, J., Dai, Y., Wang, Z., & Xu, X. (2016). Soil respiration responses to soil physiochemical properties in urban different green-lands: A case study in Hefei, China. *International Soil and Water Conservation Research, 4*(3), 224-229. http://doi.org/10.1016/j.iswcr.2016.08.001

Teskey, R., Wertin, T., Bauweraerts, I., Ameye, M., McGuire, M.A., & Steppe, K. (2015). Responses of tree species to heat waves and extreme heat events. *Plant Cell Environ, 38*(9), 1699-1712. http://doi.org/10.1111/pce.12417

Toparlar, Y., Blocken, B., Maiheu, B., & van Heijst, G.J.F. (2017). A review on the CFD analysis of urban microclimate. *Renewable and Sustainable Energy Reviews, 80*, 1613-1640. http://doi.org/10.1016/j.rser.2017.05.248

Trammell, T.L.E., Pataki, D.E., Still, C.J., Ehleringer, J.R., Avolio, M.L., Bettez, N., . . . Wheeler, M.M. (2019). Climate and lawn management interact to control C_4 plant distribution in residential lawns across seven U.S. cities. *Ecological Applications, 29*(4), e01884. http://doi.org/https://doi.org/10.1002/eap.1884

United Nations (2019). *World Urbanization Prospects: The 2018 Revision*. New York: United Nations.

United States Energy Information Administration (USEIA), 2015 Residential Energy Consumption Survey, 2018. https://www.eia.gov/consumption/residential/

Upreti, R., Wang, Z.-H., & Yang, J. (2017). Radiative shading effect of urban trees on cooling the regional built environment. *Urban Forestry & Urban Greening, 26*, 18-24. http://doi.org/10.1016/j.ufug.2017.05.008

Velasco, E., & Roth, M. (2010). Cities as Net Sources of CO_2: Review of Atmospheric CO_2 Exchange in Urban Environments Measured by Eddy Covariance Technique. *Geography Compass, 4*(9), 1238-1259. http://doi.org/https://doi.org/10.1111/j.1749-8198.2010.00384.x

Velasco, E., Roth, M., Tan, S.H., Quak, M., Nabarro, S.D.A., & Norford, L. (2013). The role of vegetation in the CO_2 flux from a tropical urban neighbourhood. *Atmospheric Chemistry and Physics, 13*(20), 10185-10202. http://doi.org/10.5194/acp-13-10185-2013

Vesala, T., Kljun, N., Rannik, U., Rinne, J., Sogachev, A., Markkanen, T., . . . Leclerc, M.Y. (2008). Flux and concentration footprint modelling: state of the art. *Environ Pollut, 152*(3), 653-666. http://doi.org/10.1016/j.envpol.2007.06.070

Vetter, M., Churkina, G., Jung, M., Reichstein, M., Zaehle, S., Bondeau, A., . . . Heimann, M. (2008). Analyzing the causes and spatial pattern of the European 2003 carbon flux anomaly using seven models. *Biogeosciences, 5*(2), 561-583. http://doi.org/10.5194/bg-5-561-2008

Vivoni, E.R., Kindler, M., Wang, Z., & Pérez-Ruiz, E.R. (2020). Abiotic Mechanisms Drive Enhanced Evaporative Losses under Urban Oasis Conditions. *Geophysical*

Research Letters, 47(22), e2020GL090123. http://doi.org/https://doi.org/10.1029/2020GL090123

Wang, C., Li, Q., & Wang, Z.-H. (2018a). Quantifying the impact of urban trees on passive pollutant dispersion using a coupled large-eddy simulation–Lagrangian stochastic model. *Building and Environment, 145*, 33-49. http://doi.org/10.1016/j.buildenv.2018.09.014

Wang, C., Wang, Z.-H., & Ryu, Y.-H. (2021b). A single-layer urban canopy model with transmissive radiation exchange between trees and street canyons. *Building and Environment, 191*. http://doi.org/10.1016/j.buildenv.2021.107593

Wang, C., Wang, Z.-H., & Yang, J. (2018b). Cooling Effect of Urban Trees on the Built Environment of Contiguous United States. *Earth's Future, 6*(8), 1066-1081. http://doi.org/https://doi.org/10.1029/2018EF000891

Wang, C., Wang, Z.-H., & Yang, J. (2019b). Urban water capacity: Irrigation for heat mitigation. *Computers, Environment and Urban Systems, 78*, 101397. http://doi.org/https://doi.org/10.1016/j.compenvurbsys.2019.101397

Wang, C., Wang, Z.-H., & Yang, J. (2019c). Urban water capacity: Irrigation for heat mitigation. *Computers, Environment and Urban Systems, 78*. http://doi.org/10.1016/j.compenvurbsys.2019.101397

Wang, C., Wang, Z.-H., Kaloush, K.E., & Shacat, J. (2021a). Cool pavements for urban heat island mitigation: A synthetic review. *Renewable and Sustainable Energy Reviews, 146*, 111171. http://doi.org/https://doi.org/10.1016/j.rser.2021.111171

Wang, C., Wang, Z.-H., Wang, C., & Myint, S.W. (2019a). Environmental cooling provided by urban trees under extreme heat and cold waves in U.S. cities. *Remote Sensing of Environment, 227*, 28-43. http://doi.org/10.1016/j.rse.2019.03.024

Wang, C., Wang, Z.H., & Yang, J. (2018c). Cooling Effect of Urban Trees on the Built Environment of Contiguous United States. *Earth's Future, 6*(8), 1066-1081. http://doi.org/10.1029/2018ef000891

Wang, H., Prentice, I.C., Keenan, T.F., Davis, T.W., Wright, I.J., Cornwell, W.K., . . . Peng, C. (2017). Towards a universal model for carbon dioxide uptake by plants. *Nature Plants, 3*(9), 734-741. http://doi.org/10.1038/s41477-017-0006-8

Wang, S., Ju, W., Peñuelas, J., Cescatti, A., Zhou, Y., Fu, Y., . . . Zhang, Y. (2019). Urban−rural gradients reveal joint control of elevated CO_2 and temperature on extended photosynthetic seasons. *Nature Ecology & Evolution, 3*(7), 1076-1085. http://doi.org/10.1038/s41559-019-0931-1

Wang, Z.-H. (2014). Monte Carlo simulations of radiative heat exchange in a street canyon with trees. *Solar Energy, 110*, 704-713. http://doi.org/https://doi.org/10.1016/j.solener.2014.10.012

Wang, Z.-H. (2021). Compound environmental impact of urban mitigation strategies: Co-benefits, trade-offs, and unintended consequence. *Sustainable Cities and Society, 75*, 103284. http://doi.org/https://doi.org/10.1016/j.scs.2021.103284

Wang, Z.-H., & Upreti, R. (2019). A scenario analysis of thermal environmental changes induced by urban growth in Colorado River Basin, USA. *Landscape and Urban Planning, 181*, 125-138. http://doi.org/https://doi.org/10.1016/j.landurbplan.2018.10.002

Wang, Z.-H., Bou-Zeid, E., & Smith, J.A. (2013). A coupled energy transport and hydrological model for urban canopies evaluated using a wireless sensor network. *Quarterly Journal of the Royal Meteorological Society, 139*(675), 1643-1657. http://doi.org/10.1002/qj.2032

Wang, Z.-H., Bou-Zeid, E., Au, S.K., & Smith, J.A. (2011). Analyzing the Sensitivity of WRF's Single-Layer Urban Canopy Model to Parameter Uncertainty Using Advanced Monte Carlo Simulation. *Journal of Applied Meteorology and Climatology, 50*(9), 1795-1814. http://doi.org/10.1175/2011JAMC2685.1

Wang, Z.-H., Zhao, X., Yang, J., & Song, J. (2016). Cooling and energy saving potentials of shade trees and urban lawns in a desert city. *Applied Energy, 161*, 437-444. http://doi.org/https://doi.org/10.1016/j.apenergy.2015.10.047

Yang, J., & Wang, Z.-H. (2014). Physical parameterization and sensitivity of urban hydrological models: Application to green roof systems. *Building and Environment, 75*, 250-263. http://doi.org/10.1016/j.buildenv.2014.02.006

Yang, J., & Wang, Z.-H. (2015). Optimizing urban irrigation schemes for the trade-off between energy and water consumption. *Energy and Buildings, 107*, 335-344. http://doi.org/https://doi.org/10.1016/j.enbuild.2015.08.045

Yang, J., & Wang, Z.-H. (2017). Planning for a sustainable desert city: The potential water buffering capacity of urban green infrastructure. *Landscape and Urban Planning, 167*, 339-347. http://doi.org/https://doi.org/10.1016/j.landurbplan.2017.07.014

Yang, J., Wang, Z.-H., & Kaloush, K.E. (2015). Environmental impacts of reflective materials: Is high albedo a 'silver bullet' for mitigating urban heat island? *Renewable and Sustainable Energy Reviews, 47*, 830-843. http://doi.org/10.1016/j.rser.2015.03.092

Yang, J., Wang, Z.-H., Chen, F., Miao, S., Tewari, M., Voogt, J.A., & Myint, S. (2014). Enhancing Hydrologic Modelling in the Coupled Weather Research and Forecasting–Urban Modelling System. *Boundary-Layer Meteorology, 155*(1), 87-109. http://doi.org/10.1007/s10546-014-9991-6

Yang, J., Wang, Z.-H., Kaloush, K.E., & Dylla, H. (2016). Effect of pavement thermal properties on mitigating urban heat islands: A multi-scale modeling case study in Phoenix. *Building and Environment, 108*, 110-121. http://doi.org/10.1016/j.buildenv.2016.08.021

Yuan, W., Luo, Y., Li, X., Liu, S., Yu, G., Zhou, T., . . . Stoy, P.C. (2011). Redefinition and global estimation of basal ecosystem respiration rate. *Global Biogeochemical Cycles, 25*(4), 1-14. http://doi.org/10.1029/2011GB004150

Zhang, L., Hu, Z., Fan, J., Zhou, D., & Tang, F. (2014). A meta-analysis of the canopy light extinction coefficient in terrestrial ecosystems. *Frontiers of Earth Science, 8*(4), 599-609. http://doi.org/10.1007/s11707-014-0446-7

Zhao, S., Liu, S., & Zhou, D. (2016). Prevalent vegetation growth enhancement in urban environment. *Proc Natl Acad Sci U S A, 113*(22), 6313-6318. http://doi.org/10.1073/pnas.1602312113

Ziter, C.D., Pedersen, E.J., Kucharik, C.J., & Turner, M.G. (2019). Scale-dependent interactions between tree canopy cover and impervious surfaces reduce daytime urban heat during summer. *Proc Natl Acad Sci U S A, 116*(15), 7575-7580. http://doi.org/10.1073/pnas.1817561116